Publicly Accessible Penn Dissertations

1-1-2014

Multi-Functional Polymer Vesicles: Applications in Chemotherapy and Photodynamic Therapy

Nimil Sood
University of Pennsylvania, nsood@seas.upenn.edu

Follow this and additional works at: http://repository.upenn.edu/edissertations

Part of the Biomedical Commons, and the Chemical Engineering Commons

Multi-Functional Polymer Vesicles: Applications in Chemotherapy and Photodynamic Therapy

Abstract

The field of drug delivery is rapidly expanding to bridge the gap between novel drugs that are created and their effective entry into diseased tissue. In one growing area of research, synthetic polymers are being utilized to meet these needs. The precise control over their chemistry allows polymers to be tuned to the drug delivery application and make them attractive candidates for research. The focus of this dissertation is to engineer responsive polymersomes for drug delivery and understand their ability to reduce drug toxicity, increase absorption in diseased cells and tissue, and control the release of drug in vitro and in vivo. Gemcitabine, a nucleoside analog, was encapsulated in the aqueous core of nano-polymersomes composed of the biodegradable and biocompatible polymer PEO-PCL, and the in vitro toxicity of this novel drug delivery construct was tested against Panc-1 cells. The polymersome formulation performed at par with the free drug with one-log cell killing at 1 Ã¬M of gemcitabine. The polymersome was also able to control the release of gemcitabine, and this release was modulated by the degradation kinetics of the ester linkages in the membrane. Photodynamic therapy was performed against OVCAR-5 (ovarian cancer) cells. A hydrophobic photosensitizer, benzoporphrin derivative monoacid A (BPD-MA) was encapsulated the in the membrane of polymersomes composed of PEO14-PBD22 (OB14.5) polymer, and its phototoxicity was compared to an existing photosensitizer formulation called verteporfin that is currently used in the clinic for age-related macular degeneration (AMD). The polymersome formulation outperformed verteporfin both at the in vitro and in vivo level. Additionally, we investigated the photorupture of giant polymersomes encapsulating a near IR fluorophore (porphyrin dimer, PZn2) in the hydrophobic membrane and dextran in the aqueous lumen. Polymersomes synthesized from softer polymers released more of a reporter dye than stiffer polymersomes when illuminated with 690 nm of light. Finally, we investigated the fractionation of giant polymersomes in a deterministic lateral displacement device and developed a hydrodynamic model to predict this fractionation based on the attractive and repulsive forces experienced by the polymersome.

Degree Type
Dissertation

Degree Name
Doctor of Philosophy (PhD)

Graduate Group
Chemical and Biomolecular Engineering

First Advisor
Daniel A. Hammer

Keywords
chemotherapy, nanoparticle, photodynamic therapy, polymersome

Subject Categories
Biomedical | Chemical Engineering

MULTI-FUNCTIONAL POLYMER VESICLES: APPLICATIONS IN DRUG DELIVERY AND

PHOTODYNAMIC THERAPY

Nimil Sood

A DISSERTATION

in

Chemical and Biomolecular Engineering

Presented to the Faculties of the University of Pennsylvania

in

Partial Fulfillment of the Requirements for the

Degree of Doctor of Philosophy

2014

Supervisor of Dissertation   Graduate Group Chairperson

_____   _____

Daniel A. Hammer, Ph.D.   Raymond J. Gorte, Ph.D.
Alfred G. and Meta A. Ennis Professor of   Russell Pearce and Elizabeth Crimian
Bioengineering and Chemical and   Heuer Professor of Chemical and
Biomolecular Engineering   Biomolecular Engineering

Dissertation Committee

Theresa M. Busch, Ph.D.   John C. Crocker, Ph.D.
Research Associate Professor   Associate Professor
Radiation Oncology   Chemical and Biomolecular Engineeing

Daeyeon Lee, Ph.D.
Associate Professor
Chemical and Biomolecular Engineeing

MULTI-FUNCTIONAL POLYMER VESICLES: APPLICATIONS IN CHEMOTHERAPY

AND PHOTODYNAMIC THERAPY

COPYRIGHT

2014

Nimil Sood

To my parents, Sunil and Anshu.

ACKNOWLEDGEMENT

ABSTRACT

MULTI-FUNCTIONAL POLYMER VESICLES: APPLICATIONS IN DRUG DELIVERY

AND PHOTODYNAMIC THERAPY

Nimil Sood

Daniel A. Hammer, Ph.D.

The field of drug delivery is rapidly expanding to bridge the gap between novel drugs that are created and their effective entry into diseased tissue. In one growing area of research, synthetic polymers are being utilized to meet these needs. The precise control over their chemistry allows polymers to be tuned to the drug delivery application and make them attractive candidates for research. The focus of this dissertation is to engineer responsive polymersomes for drug delivery and understand their ability to reduce drug toxicity, increase absorption in diseased cells and tissue, and control the release of drug *in vitro* and *in vivo*. Gemcitabine, a nucleoside analog, was encapsulated in the aqueous core of nano-polymersomes composed of the biodegradable and biocompatible polymer PEO-PCL, and the *in vitro* toxicity of this novel drug delivery construct was tested against Panc-1 cells. The polymersome formulation performed at par with the free drug with one-log cell killing at 1 µM of gemcitabine. The polymersome was also able to control the release of gemcitabine, and this release was modulated by the degradation kinetics of the ester linkages in the membrane. Photodynamic therapy was performed against OVCAR-5 (ovarian cancer) cells. A hydrophobic photosensitizer, benzoporphrin derivative monoacid A (BPD-MA) was encapsulated the in the membrane of polymersomes composed of PEO_{14}-PBD_{22} (OB14.5) polymer, and its phototoxicity was compared to an existing photosensitizer formulation called verteporfin that is

currently used in the clinic for age-related macular degeneration (AMD). The polymersome formulation outperformed verteporfin both at the *in vitro* and *in vivo* level. Additionally, we investigated the photorupture of giant polymersomes encapsulating a near IR fluorophore (porphyrin dimer, PZn_2) in the hydrophobic membrane and dextran in the aqueous lumen. Polymersomes synthesized from softer polymers released more of a reporter dye than stiffer polymersomes when illuminated with 690 nm of light. Finally, we investigated the fractionation of giant polymersomes in a deterministic lateral displacement device and developed a hydrodynamic model to predict this fractionation based on the attractive and repulsive forces experienced by the polymersome.

Table of Contents

List of Figures

1 Introduction to Synthetic Polymers as Drug Delivery Vehicles and the Specific Aims of this Dissertation

1.1 Challenges in Drug Delivery

With significant advancement in the field of medical science, new classes of pharmaceuticals and biologics are paving the way for the rapid evolution of drug delivery technologies. The underlying challenges in drug delivery, however, have remained fairly constant. Drug solubility and stability in the body, method of administration (oral, intravenous, transdermal, intramuscular, etc.), and drug absorption, distribution, metabolism, and elimination all are critical parameters that determine the overall efficacy and toxicity of a drug. The design of new drugs takes into account these considerations. Because of the complexity of new treatments, engineering smart delivery vehicles is often done in tandem with drug development. Figure 1-1 illustrates the fate of a drug and drug delivery vehicle from its introduction into the body to its ultimate metabolization and elimination. Stable drug carriers must navigate the harsh *in vivo* environment to successfully deliver the therapeutic payload to the appropriate site.

1
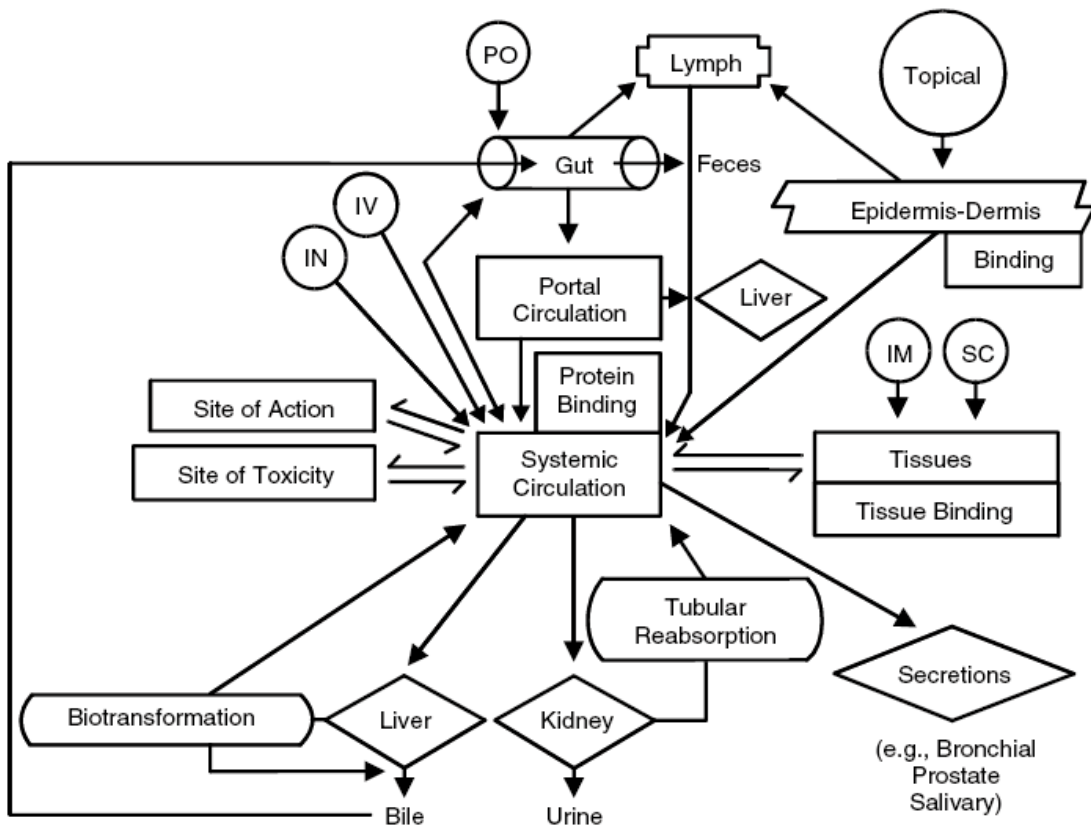
Figure 1-1: Diagram illustrating how drugs are absorbed, distributed, metabolized, and excreted from the body. Adapted from [1].

The work presented in this thesis focuses on the utility of synthetic polymers for the delivery of therapeutic drugs to cancer cells. The next section outlines the use of polymersomes, self-assembled polymer vesicles, for drug delivery applications.

2

1.2 Introduction to Polymersomes as Drug Delivery Vehicles

Polymersomes are self-assembled vesicles composed of amphiphilic block copolymers. In aqueous solution, these polymers undergo spontaneous reordering that yield mesoscopic structures ranging in size from hundreds of nanometers to tens of microns [2]. Much like the packing parameter [3] ($v/a_0 l_c$) established for the self-assembly of lipids in solution – where the ratio of the hydrophobic tail volume v to the product of the head group area a_0 and hydrophobic tail length l_c give different structures in solution ranging from micellar to bilayer vesicles – a general rule of thumb exists for polymersomes as well. The hydrophilic to total mass fraction guides the assembly of various structures. This is highlighted in Table 1-1.

Table 1-1: General guidelines for the self-assembly of block copolymers in solution. Adapted from [2].

$f_{hydrophilic}$	Shape Factor
$f < 25\%$	Inverted microstructure
$25\% < f < 35\%$	Bilayer vesicle
$f > 45\%$	Micelle

Polymersomes have significant advantages over liposomes. While both vesicles have an aqueous core and hydrophobic membrane, the hyperthick polymer membrane can encapsulate a much larger payload of hydrophobic molecules. Lipid membranes have a thickness of around 3 nm whereas polymersomes can have varying membrane thicknesses ranging from 8 nm to 21 nm [4]. Polymersome membranes are also mechanically more robust than liposome membranes. Typical values of membrane elastic moduli, as determined from micropipette aspiration, are around 100 dyne/cm for polymersomes and 150 to 1000 dyne/cm for liposomes [4, 5]. The surface chemistry of polymersomes can be readily altered to include targeting moieties. Previous work has been done to conjugate a TAT peptide on the surface of polymersomes to enhance the

uptake of vesicles by dendritic cells [6]. The improved mechanical robustness, hydrophobic encapsulation potential, and surface modification potential make polymersomes ideal candidates for targeted drug delivery applications.

1.3 Specific Aims

Aim 1: Develop controlled release nano-polymersome platform for the encapsulation and release of chemotherapeutic drug and determine toxicity in cancer cells.

Aim 2: Quantify the release of an encapsulated fluorescent dye from giant polymersomes due to photo-initiated rupture.

Aim 3: Encapsulate a photosensitizer in nano-polymersomes for photodynamic therapy and assess the *in vitro* and *in vivo* toxicity of the polymersomes.

Aim 4: Develop a force-based model for understanding and predicting polymersome fractionation in a deterministic lateral displacement microfluidic device.

1.4 Description of Dissertation

This dissertation is composed of six chapters and describes the efforts to create controlled release polymersomes for the delivery of therapeutic molecules to *in vitro* or *in vivo* cancer models.

Chapter 2 presents the preparation and characterization of nano-polymersomes synthesized from PEO-PCL that encapsulate a chemotherapeutic drug called gemcitabine. Like many other chemotherapeutic drugs, gemcitabine has a short half-life in the blood and severe dose limiting toxicities. Encapsulating gemcitabine within

polymersomes can mitigate these side effects, increase the blood circulation time, and produce greater toxicity at the cancer site. We can <u>passively control</u> the release of gemcitabine from the polymersomes by taking advantage of the PCL block degradation under acidic conditions.

Chapter 3 presents an extension of controlled release polymersomes. In this chapter, we illustrate and quantify the photoresponsiveness of giant polymersomes that contain a hydrophobic solute in the membrane (porphyrin) and a hydrophilic solute in the aqueous lumen (dextran). Under certain illumination conditions, these polymersomes undergo membrane deformation and rupture. This work has implications in the field of drug delivery since we can <u>actively control</u> the release of encapsulated molecules.

Chapter 4 presents the work done to synthesize and characterize nano-polymersomes that encapsulate a photosensitizer for photodynamic therapy (PDT). PDT provides an interesting approach to cancer therapy because the cytotoxic agent is not a small molecule drug but actually singlet oxygen. Singlet oxygen is generated locally by first administering a photosensitizer, and then illuminating the diseased tissue with a specific wavelength of light. A polymersomal formulation of the photosensitizer provides several advantages over current formulations, with the additional benefit of having a dual drug delivery vehicle encapsulating both a photosensitizer in the hydrophobic membrane and chemotherapeutic drug in the aqueous lumen.

Chapter 5 is a departure from the topic of nanoparticle drug delivery. In this chapter, I discuss the experimental and computational modeling work done to understand the fractionation of giant polymersomes in a deterministic lateral displacement microfluidic device. Synthesizing monodisperse polymersomes form thin-

film rehydration is extremely challenging. Other methods of synthesizing polymersomes (emulsion techniques, electroporation) result in a monodisperse population but low yield. Combining the rehydration technique with a fractionation will give a large number of polymersomes of a desired size.

Finally, **Chapter 6** details the major findings and future directions of the work presented in this dissertation.

1.5 References

1. Riviere JE: *Comparative Pharmacokinetics: Principles, Techniques, and Applications*. 2nd edition. John Wiley & Sons, Inc.; 2011.

2. Discher BM: Polymersomes: Tough Vesicles Made from Diblock Copolymers. *Science* 1999, 284:1143–1146.

3. Israelachvili JN: *Intermolecular and Surface Forces*. 3rd edition. Elsevier Inc.; 2011.

4. Bermudez H, Brannan AK, Hammer DA, Bates FS, Discher DE: Molecular Weight Dependence of Polymersome Membrane Structure , Elasticity , and Stability. 2002, 4:8203–8208.

5. Evans E, Needham D: Physical properties of surfactant bilayer membranes: thermal transitions, elasticity, rigidity, cohesion and colloidal interactions. *The Journal of Physical Chemistry* 1987, 91:4219–4228.

6. Christian N a, Milone MC, Ranka SS, Li G, Frail PR, Davis KP, Bates FS, Therien MJ, Ghoroghchian PP, June CH, Hammer D a: Tat-functionalized near-infrared emissive polymersomes for dendritic cell labeling. *Bioconjugate chemistry* 2007, 18:31–40.

2 Biodegradable Polymersomes for the Delivery of Gemcitabine to Panc-1 Cells

2.1 Summary

Traditional anti-cancer chemotherapy often displays toxic side effects, poor bioavailability, and a low therapeutic index. Targeting and controlled release of a chemotherapeutic agent can increase drug bioavailability, mitigate undesirable side effects, and increase the therapeutic index. Here we report a polymersome-based system to deliver gemcitabine to Panc-1 cells *in vitro*. The polymersomes were self-assembled from a biocompatible and completely biodegradable polymer, poly(ethyleneoxide)-poly(caprolactone), PEO-PCL. We showed that we can encapsulate gemcitabine within stable 200 nm vesicles with a 10% loading efficiency. These vesicles displayed a controlled release of gemcitabine with 60% release after 2 days at physiological pH. Upon treatment of Panc-1 cells *in vitro*, vesicles were internalized as verified with fluorescently labeled polymersomes. Clonogenic assays to determine cell survival were performed by treating Panc-1 cells with varying concentrations of

unencapsulated gemcitabine (FreeGem) and polymersome-encapsulated gemcitabine (PolyGem) for 48 hours. 1 µM PolyGem was equivalent in tumor cell toxicity to 1 µM FreeGem, with a one log cell kill observed. These studies suggest that further investigation on polymersome-based drug formulations are warranted for chemotherapy of pancreatic cancer.

2.2 Introduction

Pancreatic adenocarcinoma is the fourth highest cause of cancer death with a 5-year survival rate of less than 6% [1]. Despite the use of surgery, radiation and/or chemotherapy [2], local recurrence and metastasis invariably occur. The causes of resistance of pancreatic tumors are not completely understood. The inability to deliver adequate adjuvant therapy due to local normal tissue toxicity, limitations caused by tumor microenvironment (hypoxia, pH), and active drug export out of tumor cells likely cause this resistance [3-4]. Modifications to the delivery of chemotherapeutics that improve the therapeutic ratio (TR) are highly desirable in order to allow higher drug delivery while minimizing toxicity to normal tissues.

Gemcitabine is a commonly-used water soluble anticancer agent that acts as an anti-metabolite; it is considered an efficacious addition to radiation therapy in pancreatic cancer [5]. Gemcitabine is an S-phase deoxycytidine analog (2',2'-difluorodeoxycytidine). Its mechanism of action involves competitive incorporation into DNA, masked termination (causing termination of DNA synthesis without being excised out of the strand), and self-potentiation (promoting its own activity by inhibiting regulatory enzymes involved in DNA synthesis). Like most chemotherapeutics, its use has significant limitations. Gemcitabine is rapidly metabolized in the blood stream with a

9

short plasma half-life (for short infusions, 32 - 94 min) and has substantial side effects that limit the dose that can be given, especially when combined with radiation therapy [6]. In a phase 1 study, concurrent application of gemcitabine and radiation caused nausea, vomiting, dehydration and gastric ulceration resulting in a 44% hospital admission rate [7]. These side effects are much greater for concurrent therapy than for just radiation, which has been linked primarily to nausea. Encapsulation of gemcitabine in a carrier vehicle has the potential to reduce dose-limiting side effects while improving the drug delivery to the tumor. The latter includes increased circulation time and preferential accumulation in tumor due to the enhanced permeability and retention (EPR) effect [8].

Encapsulation of gemcitabine to address the challenges of rapid blood metabolism and low therapeutic ratio has been previously investigated. In one study, gemcitabine loaded in sonochemically-prepared bovine serum albumen (BSA) microspheres, was evaluated for cell killing in renal cancer *in vitro* [9]. These microspheres exhibited poor dynamics of release and were unable to take advantage of the EPR effect observed in solid tumors due to their large size (~1 μm diameter), an effect which requires 150-300 nm particles in diameter [8]. In another study, albumin nanospheres were loaded with gemcitabine [10]; this delivery system also had poor release kinetics with 100% of the drug being released in 24 hours. In a third study, encapsulated gemcitabine within poly(ethylene glycol)-poly(DL-lactic acid) (PEG-PDLLA) nano-vesicles showed toxicity against SW1990 pancreatic cells [11]. The vesicle morphology and size of these vesicles were very variable.

Polymer vesicles, or polymersomes, are self-assemblies of amphiphilic block copolymers that can encapsulate both hydrophobic and hydrophilic compounds [12-13].

Their highly tunable chemistry allows for diverse functionalities and applications [14]. Polymersomes possess superior biomaterial properties compared to their lipid counterparts (liposomes) including greater stability, storage capacity, release characteristics, and plasma circulation times [15-18]. The hydrophilic block is often composed of poly(ethylene oxide) (PEO) head groups, which helps reduce non-specific interactions with blood proteins due to their hydrophilicity and steric hindrance effects. This greatly reduces opsonization of nanoparticles and increases their plasma circulation time. Several biodegradable hydrophobic blocks can be utilized for drug delivery including polycaprolactone (PCL) and polylactide (PLA) for polymersomes and polylactic-co-glycolic acid (PLGA) for nanoparticles [14, 19-21]. PCL has several advantages over the other polymers including high permeability to small molecules, maintenance of neutral pH after degradation, ease of blending with other polymer blocks, and long-term and tunable erosion kinetics [22].

Recognizing the potential of PEO-PCL polymersomes for use in cancer treatment, this manuscript describes the novel use of PEO-PCL nano-polymersomes for gemcitabine encapsulation and *in vitro* delivery to Panc-1 cells. We investigated the polymersome release kinetics of gemcitabine, vesicle internalization by Panc-1 cells, and cell toxicity of PolyGems compared to standard gemcitabine (FreeGem). Polymersomes were internalized by Panc-1 cells and had equivalent cell toxicity at the same total dose when loaded with gemcitabine. These results suggest that PolyGems have the potential to be an attractive route to improve gemcitabine delivery *in vivo*.

2.3 Materials and Methods

2.3.1 Materials

Gemcitabine (Gemzar ®) was obtained from Eli Lilly and Company (Indianapolis, IN). Panc-1 cells were obtained from the ATCC. DMEM/F12 Ham's (50/50) without phenol red was purchased from ZenBio (Research Park, NC). The meso-to-meso ethyne bridged (porphinato) zinc(II) trimer (PZn$_3$) with a 9-methoxy-1,4,7-trioxanonyl substituent on one aryl group and a more hydrophobic 3,3-dimethyl-1-butyloxy substituent on the other, was synthesized as previously described [23]. Glacial acetic acid, methylene chloride, methylene blue for colony staining, phosphate buffered saline (PBS), sodium acetate trihydrate, and sodium chloride were purchased from Fisher Chemicals (Pittsburgh, PA). Polycarbonate extrusion membranes (13 mm) were purchased from Whatman (Piscataway, NJ). Centrifugal filter units were purchased from Millipore (Billerica, MA). Dialysis cassettes were purchased from Spectrum Laboratories (Rancho Dominguez, CA).

2.3.2 PEO-PCL Preparation

PEO-*b*-PCL with 45 and 105 monomer repeat units per block, respectively (MW = 14,000 g mol^{-1}) was synthesized prior to this work [14]. The block co-polymer was generated via ring-opening polymerization of cyclic ε-caprolactone. Briefly, monomethoxypoly(ethylene oxide) (2k) was filled in a flame-dried flask under argon. Caprolactone monomer was injected into the flask via syringe and two drops of stannous(II) octoate was added to the reaction mixture. The reaction occurred at 130°C for 24 hours. The copolymer was isolated by dissolving the product in methylene chloride and precipitating in excess methanol/hexane at 4°C. The resulting powder was

dried further. The block co-polymer was purified via gel permeation chromatography and the molecular weight was determined by ^{1}H NMR.

2.3.3 Vesicle Preparation

Polymersomes were synthesized by the thin film hydration method as described elsewhere [14]. Briefly, 200 µL of a 100 mg/mL PEO-PCL solution in methylene chloride were deposited on a roughened Teflon strip and allowed to dry overnight under vacuum. A 2.21 mg/mL (corresponding to 5:1 molar ratio of drug:polymer) solution of gemcitabine in 0.9% saline (~290 mOsm) was added to the film in a 20 mL vial in order to hydrate the polymer. Polymersomes were formed by one hour of sonication at 60°C and 5 freeze/thaw cycles using liquid nitrogen. A narrow size distribution of polymersomes was obtained by successive extrusion through 400 nm, 200 nm, and 100 nm membranes using a thermobarrel extruder (Lipex Biomembranes, Vancouver, Canada) operating at 65°C. Size was verified using a NanoZs Zetasizer (Malvern Instruments, Southboro, MA). 0.9% saline without drug was used as the hydration solution for control studies. For cellular uptake studies, polymersomes were loaded with the porphyrin-based near-IR fluorophore, PZn_3 (λ_{ex} = 785 nm, λ_{em} = 800 nm), at a molar ratio of 40:1 polymer to PZn_3 by cocasting the PZn_3 with the polymer film. Before cell culture studies, vesicles were sterilized for 30 minutes via germicidal UV irradiation.

2.3.4 Cryo-TEM

Cryogenic Transmission Electron Microscopy was performed at the University of Pennsylvania in the Penn Regional Nanotechnology Facility (Philadelphia, PA). Lacey formvar/carbon grids (Ted Pella) were rinsed with chloroform to remove the formvar template and subsequently carbon coated with a Quorum Q150T ES carbon coater

(Quorum Technologies, United Kingdom). Grids were cleaned with hydrogen/oxygen plasma for 15 seconds using the Solarus Advanced Plasma System 950 (Gatan, Pleasanton, CA). Polymersome sample (2μL) was deposited on lacey formvar/carbon mesh grid (Ted Pella) and inserted into a cryoplunger (Gatan Cp3, Gatan). The sample was blotted by hand and plunged into liquid ethane. Samples were transferred to a cryoholder (Gatan CT3500TR, Gatan) and the cryoholder was immediately inserted into a JEOL 2010 TEM (JEOL) operating at 200 kV. Micrographs were imaged with an Orius SC200 digital camera.

2.3.5 Vesicle Release Kinetics

Nano-vesicles were prepared as described above. After extrusion, vesicles were concentrated to 0.5 mL volume using 3 kDa centrifugal filters made from regenerated cellulose. Additional removal of unencapsulated drug was performed via dialysis against a pH 5.0 sodium acetate/sodium chloride buffer (acidified with glacial acetic acid) or pH 7.4 PBS buffer. Immediately following dialysis, 250 μL sample aliquots were placed in microdialysis tubes and stored in 22 mL of pH 5.0 or 7.4 buffer in a 37°C oven. At predefined time points, aliquots were taken from the buffer solution and read on a UV/Vis spectrophotometer at 270 nm ($\varepsilon = 9.86 \times 10^{-3}$ cm^{-1} μM^{-1}). Aliquots were returned to the buffer to maintain a constant volume. 100% release was determined by addition of 100 μL of a 1% Triton-X solution to the PolyGem vials after one week and the gemcitabine absorbance after overnight storage at 37°C was measured.

2.3.6 Cell Culture

At the time of receipt from the ATCC, cells were placed in cryo-vials and stored in liquid nitrogen for future use. Cells for study were defrosted using standard procedures.

New cell stock was defrosted at 6-month intervals. Panc-1 cells were cultured in DMEM/F12 Ham's (50/50) without phenol red and with 12% fetal calf serum and 1% Pen/Strep. Cells were maintained in T-75 plastic culture flasks at 37°C in a humidified atmosphere containing 5% CO_2 in air. Flasks were subcultured when they were 75 – 90% confluent. Five minute exposure to 0.05% trypsin-EDTA was used to release attached cells from the tissue culture surface.

2.3.7 *In Vitro* Cellular Uptake of Vesicles

Fluorescent polymersomes were synthesized as described above. The concentration of PZn_3 was determined by Beer's Law using the established extinction coefficient $\varepsilon(795nm) = 1.25$ cm^{-1} µM^{-1} [24]. Panc-1 cells were plated in triplicate at 5,000 cells per well in 96 well (black frame, clear well) cell culture plates (Isoplate-96 TC, Perkin Elmer). Cells were allowed to adhere overnight. The following day, varying concentrations of fluorescent polymersomes were added to wells and were incubated for 12, 24, and 48 hours. At each time point, one plate was removed from incubation, washed three times with media to remove all polymersomes that were not internalized. Vesicles were illuminated on a LICOR Odyssey (λ_{ex} = 488 nm, λ_{em} = 810 nm). A calibration curve was generated to relate the fluorescence signal from wells to the concentration of PZn_3 to determine cellular uptake. Confocal laser scanning microscopy (CLSM) was used to visualize vesicle internalization in Panc-1 cells incubated with fluorescent polymersomes for 12 hours. An Olympus Fluoview FV1000 confocal microscope (Center Valley, PA) with a PLFLN 40x oil objective lens was used to obtain z-stacks of cells with a scan speed of 8.0 µs pixel^{-1} and step size of 1µm.

2.3.8 *In Vitro* Toxicity

Panc-1 cells were plated onto 60 mm tissue culture dishes. After 48 hours, the plates were examined under the microscope for evidence of cell growth. Only plates containing of 50-90% confluent cells were used for study. Following the removal of spent media, the plates were rinsed with 2 mL of fresh media. The rinse media was then replaced with 2 mL of treatment solution (Polygem, FreeGem, or blank polymersomes). Dishes were incubated for an additional 48 hours. At the time of assay, cells were removed from the plate by incubating 2 mL of 0.05% trypsin-EDTA with the cells for 5 minutes at 37°C. Trypsin was inactivated using fresh media with serum, and the total cell number was determined using a Coulter counter. A clonogenic assay was performed using standard techniques [25]. Plates were incubated for two weeks, with the goal of obtaining 25-250 colonies per plate. The surviving fraction was determined by normalizing the colony count of the treated condition by the initial cell number plated. The concentration of gemcitabine as reported for PolyGem represents the total encapsulated concentration. We corrected for the drug release relative to time, which was 60% release at 48 hours. The survival graphs were presented in absolute fractions with the maximal plating efficiency of untreated Panc-1 cells being 0.60. All comparisons were made to this value. Qualitative morphology of treated cells was observed using a Zeiss inverted microscope. Panc-1 cells were treated with media, 5 µM FreeGem, 5 µM PolyGem, or 2.5 µM blank polymersomes.

2.3.9 Statistical Analysis

All experiments were performed in triplicate, except where noted. *In vitro* toxicity studies were performed in duplicate with varying amounts of initial cell plating to ensure the resulting colonies were within a countable range (50-200 colonies). Data were

reported as mean ± standard deviation and analyzed by Single Factor ANOVA, setting the level of significance at $p < 0.05$.

2.4 Results and Discussion

Despite the advancement of chemoradiation therapy for the treatment of pancreatic cancer, the 5-year survival rate continues to among be the lowest of solid tumors. Any improvement in the delivery of chemotherapeutics to pancreatic cancer should mitigate side-effects associated with treatment and improve the survival outlook for patients. In the studies reported herein, we created a prototype vehicle which could ultimately be capable of delivering gemcitabine, a potent pancreatic cancer drug, to pancreatic cancer. The major aim of this work was to perform a comparative *in vitro* study of the cell-killing efficacy of polymersome-encapsulated gemcitabine (PolyGem) and unencapsulated gemcitabine (FreeGem) on Panc-1 cells.

2.4.1 Vesicle Preparation and Characterization

Bioresorbable polymersomes were synthesized via the thin-film rehydration method from two FDA-approved polymers, poly(ethylene oxide) (PEO) and poly(caprolactone) (PCL), which were covalently linked to form a diblock copolymer. PEO-PCL self-assembled in a fashion such that the hydrophobic PCL block was embedded in the polymersome membrane and the PEO block was exposed on the outer vesicle surface and inner corona. Thin-film rehydration is particularly attractive for making polymersomes for biological applications as it does not require the use of potentially toxic organic solvents during the hydration step (as is employed in the solvent injection method) [26]. Figure 2-1 shows a schematic of our novel carrier.
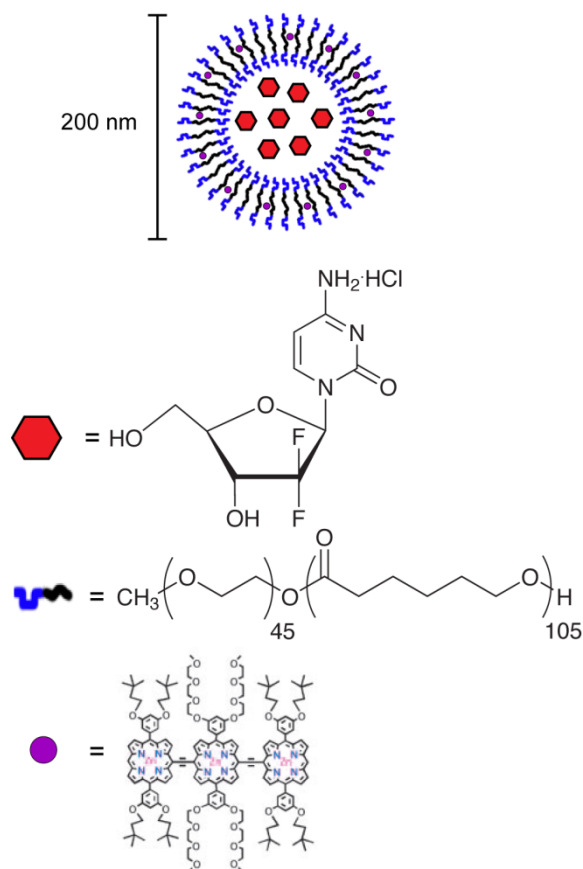
Figure 2-1: Schematic representation of PolyGem. In aqueous solution, poly(ethylene oxide)-b-poly(caprolactone) (PEO-PCL) self-assemble into spherical polymer vesicles (polymersomes), with the hydrophobic PCL chains orienting end-to-end to form the bilayer. The figure represents a uniaxial cross section of the polymersome, with gemcitabine (⬡) encapsulated in the aqueous lumen. Vesicles can also be made to include PZn_3 (⬤) in the hydrophobic membrane.

The size distribution of vesicles was measured using dynamic light scattering (DLS) and is shown in Table 2-1. Vesicles were serially extruded through 400, 200, 100, 100, and 200 nm polycarbonate membranes to reduce the sample polydispersity. The average hydrodynamic diameter of PolyGems was 180 nm. The hydrodynamic diameter of blank polymersomes (181 nm) and PZn_3-polymersomes (180 nm) did not statistically vary from PolyGems ($p > 0.05$).

Table 2-1: Hydrodynamic diameter and polydispersity of different polymersome formulations.

Vesicle Type	D_h (nm)	Polydispersity
PolyGem	180 ± 12	0.146 ± 0.045
Blank polymersome	181 ± 13	0.113 ± 0.023
PZn_3-polymersome	180 ± 31	0.163 ± 0.020

Vesicles were stored at 4ºC and used in the studies within one week of preparation. We evaluated the stability of gemcitabine after sonication and freeze/thaw cycles by checking the absorbance of the drug before and after processing. There was no difference in the absorbance spectrum, indicating that the drug retained its structure.

2.4.2 Vesicle Drug Release

To improve the tumor-killing effect of drug delivery vesicles *in vivo*, maximal drug release should occur between 10 and 20 hours following injection, during which time the majority of vesicles have accumulated at the tumor and can cause toxicity [27]. In order to approximate the time constants of release of gemcitabine *in vivo*, we first explored the *in situ* release of gemcitabine from PolyGems under acidic (pH 5.0) and physiological conditions (pH 7.4) as shown in Figure 2-2. Approximately 20% of the gemcitabine is released from the PolyGems within the first few hours at both pHs. The concentration of gemcitabine released begins to level off at approximately day two, indicating stable and controlled release after an initial period up to 48 hours.
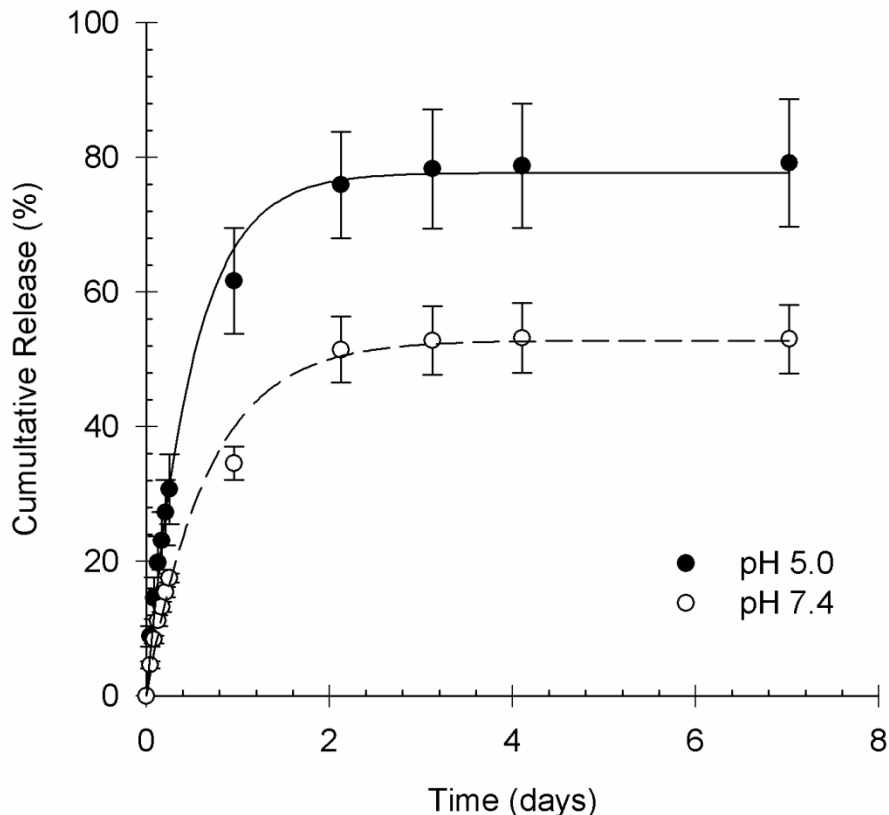
Figure 2-2: Cumulative *in situ* release of gemcitabine from PolyGem. Release was measured at pH 5.0 and 7.4 at 37°C. Gemcitabine was detected via UV/Vis spectroscopy for 7 days. N = 3 for each data point and the error bars represent standard deviation.

The release curves are well fit by a function of the form $c/c_0 = \alpha(1 - e^{-t/\tau})$, where α is a lumped constant and τ is the characteristic time constant. This functional form can be derived from a 1-D analysis of drug diffusion across a semi-permeable membrane. Fitting this equation to the release curves in Figure 2-2 reveal that τ_{pH5} is 12 hours and τ_{pH7} is 16 hours (lower values of τ indicate more rapid release). These time constants describe the time required for 63% $(1 - 1/e)$ of the drug to be released due to diffusion, and are functions of polymersome properties including geometric radius, membrane thickness, and diffusivity and partition coefficient of gemcitabine in the membrane. The time constants verify the quicker release observed at acidic conditions, with τ_{pH5} equal to 12 hours and τ_{pH7} equal to 16 hours. The ideal time constant for release depends on the

20

time required for polymersomes to localize at a tumor site. Minimal drug should be released due to passive diffusion while the vesicles are still en route, and maximal and prolonged release should occur when vesicles have reached the tumor. As seen from the release curves, the majority of the gemcitabine was released within 2 days, which is consistent with the 10-20 hour window observed by Ahmed and coworkers [27].

A burst release of drug was observed during the first few hours, which was likely caused by the initially steep concentration gradient of gemcitabine present across the vesicle membrane, leading to a high initial diffusive flux. One explanation of this observation is that some entrapped gemcitabine in the outer PEO corona may have also contributed to the burst. Gemcitabine release was greater at all time points under acidic pH as compared to physiological pH. The PCL block is known to undergo hydrolysis of its ester linkages in solution, with a higher rate of degradation observed at acidic pHs as compared to physiological pHs [28-29]. Consequently, both membrane permeability and the diffusive flux of gemcitabine increased at pH 5.0.

2.4.3 Cryo-TEM of Vesicles

In order to understand the difference in observed release rate between vesicles at pH 5.0 and 7.4, we observed the structure of nanovesicles using cryo-TEM at the incubation different conditions. Figure 2-3 provides representative images of vesicles that have been incubated at either pH 7.4 (Figure 2-3A) or pH 5.0 (Figure 2-3B-D) for 12 hours. The vesicles in Figure 2-3A have an even membrane thickness that is indicative of an intact membrane. The vesicles in Figure 2-3B-D have compromised membranes as shown by the arrows. In Figure 2-3B, the membrane of one vesicle has completely disintegrated and has formed a pore. Figure 2-3C shows a vesicle with a thinning portion of the membrane. Finally, in Figure 2-3D we see a membrane pore starting to form.
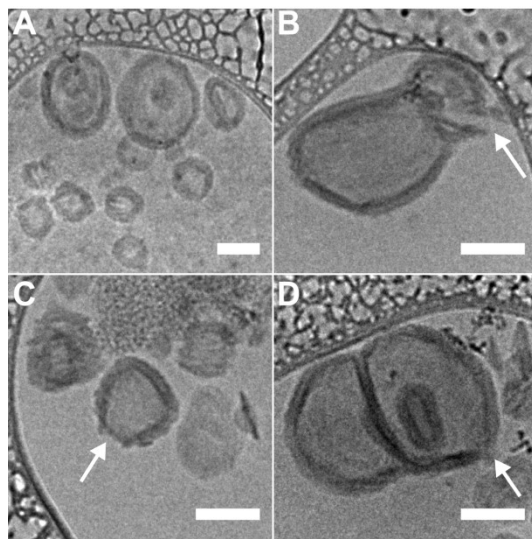
Figure 2-3: Cryo-TEM micrographs of PEO-PCL vesicles. Images were taken 12 hours after incubation at 37C at (A) pH.7.4 and (B)-(D) pH 5.0.Arrows indicate areas of membrane degradation. Scale bar = 100 nm.

Understanding the release at pH 5.0 is especially important for *in vivo* delivery to tumors because the extracellular environment of many tumors is acidic [30-32]. PolyGems would likely experience both acidic and physiological pH as they reach the tumor.

2.4.4 *In Vitro* Cellular Uptake

While it is known that polymersomes will partition into tumor tissue *in vivo* [24], cellular internalization of the vesicles at the tumor is desirable so the chemotherapeutic cargo can be released inside the cell in addition to the interstitial spaces where plasma clearance could be problematic. We visualized polymersome internalization by a cellular uptake study of blank polymersomes loaded with a hydrophobic porphyrin-based NIR fluorophore, PZn_3, in the vesicle membrane. PZn_3-based polymersomes have been utilized in the past to investigate polymersome uptake in dendritic cells (DCs) and DC trafficking *in vivo* [33-34]. In our study, Panc-1 cells were incubated with 50, 250, or 500

22

nM of PZn$_3$-loaded polymersomes in 96 well plates for 12, 24, or 48 hours. A calibration was performed to relate the integrated intensity in wells to PZn$_3$ concentration. Figure 2-4 shows the concentration of internalized PZn$_3$ as a function of incubation time. Vesicle uptake increased with an increase in the concentration of PZn$_3$ as well as incubation time. In order to confirm that the internalization from the uptake study was not surface association, Panc-1 cells were incubated with 500 nM PZn$_3$ for 12 hours and imaged on a confocal microscope with 1 µm z-slices. Figure 2-4C shows z-slices starting from the top of the cell and moving to the bottom. Vesicles are only observed internally and not on the cell surface.
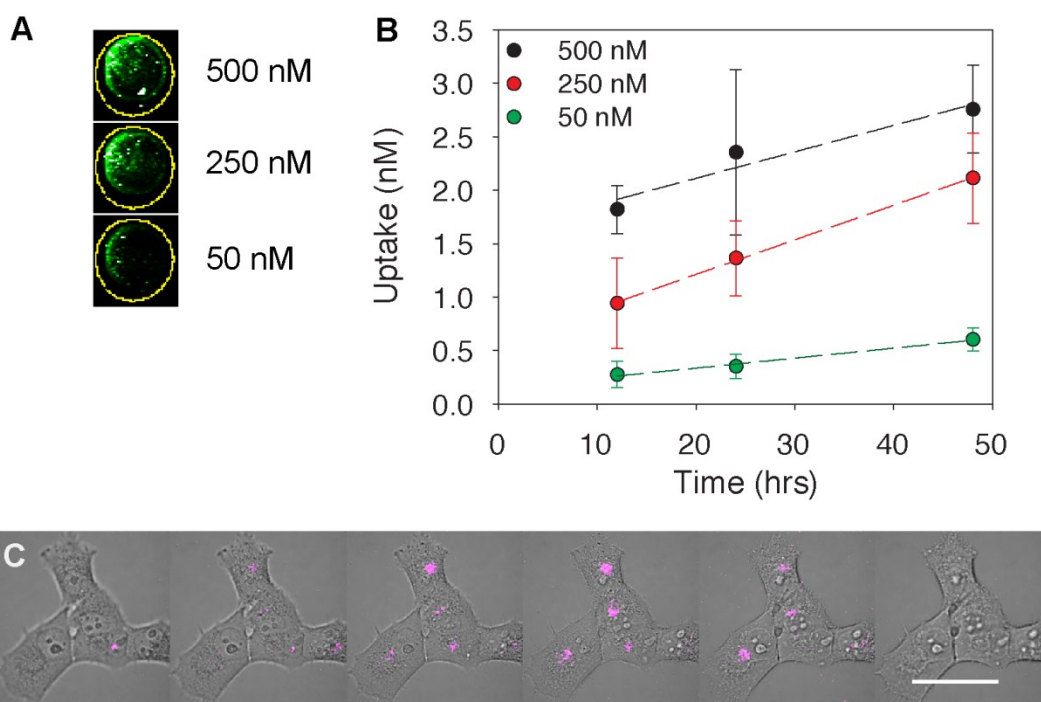
Figure 2-4: PolyGem internalization by Panc-1 cells. (A) Fluorescence intensity of PZn$_3$-polymersomes internalized by cells in well plates corresponding to 48 hour time point. (B) Concentration of PZn$_3$ uptake as a function of solution PZn$_3$ concentration (n = 3). Error bars indicate standard deviation. (C) CLSM z-stack images of Panc-1 cells incubated with PZn$_3$-polymersomes for 12 hours. Z-slices (Δz = 3 µm) are presented from left to right. Scale bar = 50 µm.

The uptake study of PolyGems showed that vesicle internalization is a concentration- and time-dependant process with more internalization occurring for higher

polymersome number and longer incubation times. However, a relatively low percentage of vesicle internalization was observed. A likely contributor is the stealth character imparted by the PEO block to the PolyGem, rendering the vesicles virtually invisible to Panc-1 cells. Another possible reason for low uptake could be a reduced cell surface area available for internalization due to cell adhesion on a tissue culture plate. Christian and coworkers observed a similar trend when incubating PZn_3-polymersomes with dendritic cells. Negligible uptake was noticed for vesicles decorated with a PEO brush as compared to vesicles surface-conjugated with the HIV-derived TAT peptide [33].

2.4.5 *In Vitro* Cell Toxicity

Panc-1 cell survival was determined by a clonogenic assay following 48 hour FreeGem or PolyGem exposure using varying drug concentrations (Figure 2-5). Panc-1 survival is concentration dependent with an observed increase in cell kill as gemcitabine concentration was increased irrespective of the formulation used. A one log cell kill is observed at approximately 1 µM gemcitabine, irrespective of the formulation. The only drug concentration where there was a significant difference in survival between FreeGem and PolyGems was at 0.05 µM gemcitabine (p = 0.048) where the PolyGem were more effective than the FreeGem. There was no significant cell kill using either blank polymersomes (0 µM PolyGem) or media-only treatment (0 µM FreeGem) as seen in Figure 2-5.
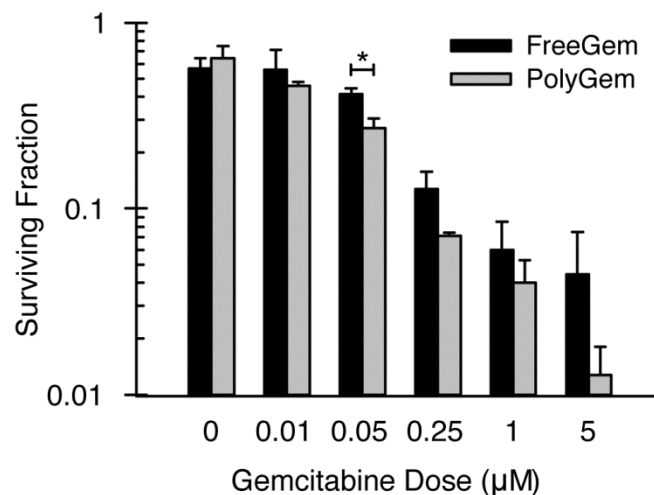
Figure 2-5: Panc-1 survival curve. Viability was determined after 48 hour treatment with varying concentrations of FreeGem or PolyGem, as measured by a clonogenic assay. Error bars indicate standard deviation (n = 3). * $p < 0.05$.

To qualitatively assess cell toxicity, Panc-1 cells were imaged using differential interference contrast microscopy (DIC) following 48 hour exposure to media, 5 µM FreeGem, 5 µM PolyGem, or 2.5 µM blank polymersomes. These doses of PolyGem, FreeGem, and blank polymersomes were chosen to reflect the maximum concentration of gemcitabine delivered to Panc-1 cells in the clonogenic assay and to equate the concentration of PEO-PCL across the formulations (2:1 ratio of drug to polymer). Figure 2-6A and Figure 2-6B demonstrate that application either of media or blank polymersomes, respectively, have no effect on cell viability since the cells are morphologically normal. Both 5 µM FreeGem and 5µM PolyGem treatments (Figure 2-6C and Figure 2-6D, respectively), resulted in significant cell killing as observed by the presence of morphologically abnormal cells and cellular debris.
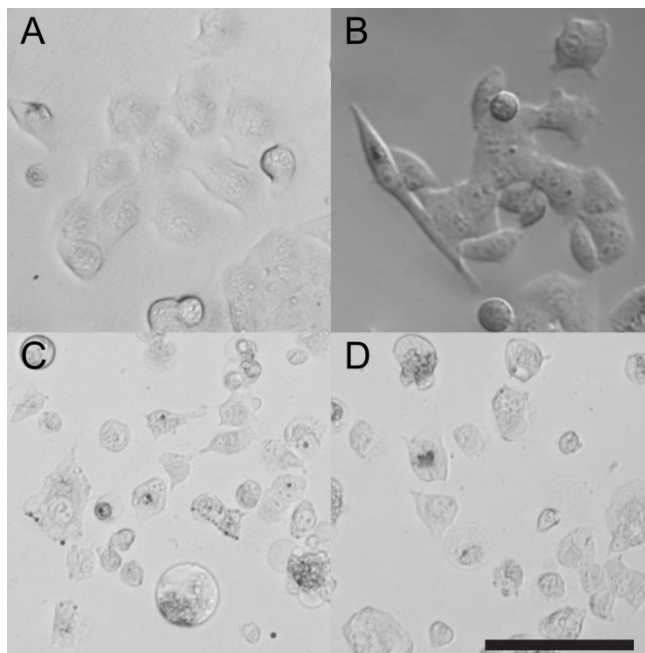
Figure 2-6: Cell phenotype as visualized by DIC. (A) Media control, (B) 2.5 μM empty polymersomes, (C) 5 μM FreeGem, and (D) 5 μM PolyGem. Scale bar = 100 μm.

Despite the low uptake without any targeting peptides, PolyGems performed at par with FreeGem (Figure 2-5). We believe that PolyGems released gemcitabine into the cell media, which was then internalized along with some vesicles via endocytosis and eventually leading to toxicity.

2.5 Conclusion

The true potential of PolyGems can best be determined *in vivo* where the drug kinetics are affected by all aspects of the tumor microenvironment, and the therapeutic ratio (TR) can be assessed. This ratio is optimally greater than one under *in vivo* conditions. Gemcitabine-based chemoradiotherapy in pancreatic cancer currently has a very narrow TR, being very close to one [35-36]. The result is substantial toxicity to the GI tract. We propose that this TR can be improved in future studies using the PolyGem technology. These nano-vesicles encapsulate and release gemcitabine over a prolonged period of time, which will likely be sufficient for non-specific accumulation of PolyGems

26

at the tumor site due to the EPR effect. A higher local concentration of drug in the tumor interstitial fluid can be expected because the polymersome prevents significant degradation of gemcitabine while trafficking to the tumor site. We predict that endocytosis of both free drug (due to release from the vesicles) and a portion of encapsulated drug will occur. The current findings – no decreased toxicity of gemcitabine using the encapsulated agent at equal concentrations of the free agent – are encouraging and support performing *in vivo* studies. Future studies will also focus on increasing efficacy by engineered internalization (i.e., using TAT-peptides conjugated to the polymersome surface) and targeting to specific cell surface receptors.

2.6 Acknowledgements

The results and conclusions presented in this chapter are published in the Journal of Pharmaceutics. The complete reference is as follows: Sood N., Jenkins W.T., Yang X., Shah N.N., Katz J.S., Koch C.J., Frail P.R., Therien M.J., Hammer D.A., Evans S.M. Biodegradable polymersomes for the delivery of gemcitabine to Panc-1 cells. *J. Pharmaceutics*. Vol. 2013.

2.7 References

1. Jemal, A., et al., *Cancer Statistics, 2010.* Ca-a Cancer Journal for Clinicians, 2010. **60**(5): p. 277-300.

2. Group, G.S., *Radiation therapy combned with adriamycin or 5-fluorouracil for the treatment of locally unresectable pancreatic carcinoma.* Cancer, 1985. **56**: p. 2563-2568.

3. Gottesman, M.M., *Mechanisms of cancer drug resistance.* Annual Review of Medicine, 2002. **53**: p. 615-627.

4. Wilson, W.R. and M.P. Hay, *Targeting hypoxia in cancer therapy.* Nature Reviews Cancer, 2011. **11**(6): p. 393-410.

5. Pauwels, B., et al., *Combined modality therapy of Gemcitibine and Radiation Therapy.* The Oncologist, Radiation Oncology, 2005. **10**: p. 34-51.

6. Moertel, C.G., et al., *Therapy of locally unresectable pancreatic carcinoma: a randomized comparison of high dose (6000 rads) radiation alone, moderate dose radiation (4000 rads + 5-fluorouracil), and high dose radiation + 5-fluorouracil: The Gastrointestinal Tumor Study Group.* Cancer, 1981. **48**(8): p. 1705-10.

7. Wolff, R.A., et al., *Phase I Trial of Gemcitabine Combined with Radiation for the Treatment of Locally Advanced Pancreatic Adenocarcinoma.* Clinical Cancer Research, 2001. **7**: p. 2246- 2249.

8. Alexis, F., et al., *Factors affecting the clearance and biodistribution of polymeric nanoparticles.* Molecular Pharmaceutics, 2008. **5**(4): p. 505-515.

9. Grinberg, O., et al., *Sonochemically prepared BSA microspheres containing Gemcitabine, and their potential application in renal cancer therapeutics.* Acta Biomaterialia, 2009. **5**(8): p. 3031-3037.

10.   Li, J.M., et al., *Preparation of albumin nanospheres loaded with gemcitabine and their cytotoxicity against BXPC-3 cells in vitro.* Acta Pharmacologica Sinica, 2009. **30**(9): p. 1337-1343.

11.   Jia, L., et al., *Preparation, physicochemical characterization and cytotoxicity in vitro of gemcitabine-loaded PEG-PDLLA nanovesicles.* World J Gastroenterol, 2010. **16**(8): p. 1008-13.

12.   Discher, B.M., et al., *Polymersomes: Tough vesicles made from diblock copolymers.* Science, 1999. **284**(5417): p. 1143-1146.

13.   Discher, D.E. and A. Eisenberg, *Polymer vesicles.* Science, 2002. **297**(5583): p. 967-973.

14.   Ghoroghchian, P.P., et al., *Bioresorbable vesicles formed through spontaneous self-assembly of amphiphilic poly(ethylene oxide)-block-polycaprolactone.* Macromolecules, 2006. **39**(5): p. 1673-1675.

15.   Kamat, N.P., et al., *A Generalized System for Photoresponsive Membrane Rupture in Polymersomes.* Advanced Functional Materials, 2010. **20**(16): p. 2588-2596.

16.   Katz, J.S., et al., *Membrane Stabilization of Biodegradable Polymersomes.* Langmuir, 2009. **25**(8): p. 4429-4434.

17.   Katz, J.S., et al., *Modular Synthesis of Biodegradable Diblock Copolymers for Designing Functional Polymersomes.* Journal of the American Chemical Society, 2010. **132**(11): p. 3654-+.

18.   Robbins, G.P., et al., *Photoinitiated Destruction of Composite Porphyrin-Protein Polymersomes.* Journal of the American Chemical Society, 2009. **131**(11): p. 3872-+.

19.   Ayen, W.Y., K. Garkhal, and N. Kumar, *Doxorubicin-Loaded (PEG)(3)-PLA Nanopolymersomes: Effect of Solvents and Process Parameters on Formulation*

Development and In Vitro Study. Molecular Pharmaceutics, 2011. **8**(2): p. 466-478.

20. Meng, F.H., G.H.M. Engbers, and J. Feijen, *Biodegradable polymersomes as a basis for artificial cells: encapsulation, release and targeting.* Journal of Controlled Release, 2005. **101**(1-3): p. 187-198.

21. Park, J., et al., *PEGylated PLGA nanoparticles for the improved delivery of doxorubicin.* Nanomedicine-Nanotechnology Biology and Medicine, 2009. **5**(4): p. 410-418.

22. Sinha, V.R., et al., *Poly-epsilon-caprolactone microspheres and nanospheres: an overview.* International Journal of Pharmaceutics, 2004. **278**(1): p. 1-23.

23. Duncan, T.V., et al., *Exceptional near-infrared fluorescence quantum yields and excited-state absorptivity of highly conjugated porphyrin arrays.* Journal of the American Chemical Society, 2006. **128**(28): p. 9000-9001.

24. Ghoroghchian, P.P., et al., *Near-infrared-emissive polymersomes: Self-assembled soft matter for in vivo optical imaging.* Proceedings of the National Academy of Sciences of the United States of America, 2005. **102**(8): p. 2922-2927.

25. Evans, S.M., et al., *2-nitroimidazole (EF5) binding predicts radiation resistance in individual 9L sc tumors.* Cancer Research, 1996. **56**(2): p. 405-411.

26. Yildiz, M.E., et al., *Formation and characterization of polymersomes made by a solvent injection method.* Polymers for Advanced Technologies, 2007. **18**(6): p. 427-432.

27. Ahmed, F., et al., *Shrinkage of a rapidly growing tumor by drug-loaded polymersomes: pH-triggered release through copolymer degradation.* Molecular Pharmaceutics, 2006. **3**(3): p. 340-350.

28. Grayson, A.C.R., M.J. Cima, and R. Langer, *Size and temperature effects on poly(lactic-co-glycolic acid) degradation and microreservoir device performance.* Biomaterials, 2005. **26**(14): p. 2137-2145.

29. Ivanova, T., et al., *Hydrolysis kinetics of poly(D,L-lactide) monolayers spread on basic or acidic aqueous subphases.* Colloids and Surfaces B-Biointerfaces, 1997. **8**(4-5): p. 217-225.

30. Gerweck, L.E. and K. Seetharaman, *Cellular pH gradient in tumor versus normal tissue: Potential exploitation for the treatment of cancer.* Cancer Research, 1996. **56**(6): p. 1194-1198.

31. Gillies, R.J., *MRI of the tumor microenvironment. (vol 16, pg 430, 2002).* Journal of Magnetic Resonance Imaging, 2002. **16**(6): p. 751-751.

32. Swietach, P., R.D. Vaughan-Jones, and A.L. Harris, *Regulation of tumor pH and the role of carbonic anhydrase 9.* Cancer and Metastasis Reviews, 2007. **26**(2): p. 299-310.

33. Christian, N.A., et al., *Tat-functionalized near-infrared emissive polymersomes for dendritic cell labeling.* Bioconjugate Chemistry, 2007. **18**(1): p. 31-40.

34. Christian, N.A., et al., *In Vivo Dendritic Cell Tracking Using Fluorescence Lifetime Imaging and Near-Infrared-Emissive Polymersomes.* Molecular Imaging and Biology, 2009. **11**(3): p. 167-177.

35. Reddy, L.H., et al., *Anticancer Efficacy of Squalenoyl Gemcitabine Nanomedicine on 60 Human Tumor Cell Panel and on Experimental Tumor.* Molecular Pharmaceutics, 2009. **6**(5): p. 1526-1535.

36. Hertel, L.W., et al., *Synthesis and biological activity of 2',2'-difluorodeoxycytidine (gemcitabine)*, in *Biomedical Frontiers of Fluorine Chemistry*, I. Ojima, J.R. McCarthy, and J.T. Welch, Editors. 1996, Amer Chemical Soc: Washington. p. 265-278.

3 Light Responsive Polymersomes: Understanding the Light Dose Response of Soft Vesicles

3.1 Summary

Altering membrane properties of soft vesicles can be of great interest in the field of generating synthetic cells that can mimic biological function. It has been recently shown that polymersomes encapsulating a near IR porphyrin fluorophore in the hydrophobic membrane and dextran in the aqueous lumen undergo membrane instability when exited with visible light. With drug delivery as a motivating factor, causing this membrane stability to occur at low laser power and induced by near IR light can be quite beneficial. The work presented here describes a soft vesicle system that undergoes photorupture from 690 nm light at low light doses. Furthermore, we quantify the rupture of these vesicles by determining the release percentage of an encapsulated fluorescent molecule, sulforhodamine B. We compared the release from vesicles composed of soft and stiffer membranes and quantify up to 40% release from the soft vesicles after 100 J/cm^2 of 690 nm light delivery.

3.2 Introduction

Polymersomes are bilayer vesicles self-assembled from amphiphilic copolymers [1]. Because of their robust chemical and mechanical properties, polymersomes have played an important role in therapeutic and diagnostic (theranostic) applications in drug delivery for cancer [2, 3], developing biomimetic systems to understand cellular processes [4], and acting as *in situ* mechanical stress sensors [5]. Polymersomes in the field of drug delivery have received particular attention. The large aqueous core and hyperthick hydrophobic membrane are capable of encapsulating significant concentrations of both hydrophilic and hydrophobic drugs, respectively, effectively providing a protective shell that increases drug circulation time *in vivo* [6]. There are several engineering challenges associated with synthesizing these polymersomes, and one of them is the release mechanism of the drug from the delivery vehicle.

Several polymersome systems rely on internal release mechanisms such as pH, temperature, and redox potential to release the encapsulated cargo. The method of vesicle destabilization include altering the hydrophilicity of the polymer [7] or degrading a polymer block [6, 8, 9]. These internal release mechanisms take advantage of the tumor microenvironment, which is known to be acidic and reducing [10-12]. These harsh microenvironments cause polymersomes to undergo shape changes (vesicular to micellar) or increase the permeability of the membrane to facilitate drug diffusion across the hydrophobic membrane. While internal release mechanisms provide an escape route for drugs from the carrier, they are ultimately dependent on the highly variable microenvironment. The transition from internal release mechanisms to external mechanisms is advantageous because it could provide precise spatiotemporal control over drug delivery.

Recently, groups have reported light-mediated release from polymersomes. Light is an attractive external release trigger because it is noninvasive and can be directed at the desired site of release (eg. tumor). Typically, these systems contain light-activated linkers that combine the hydrophilic and hydrophobic blocks of the diblock copolymer. Upon excitation with light ranging from ultraviolet to near infrared, the linker cleaves and causes the vesicle to rupture [13, 14]. The synthesis and purification of such linker-derived polymers can be challenging and often the energy required to cleave the linkers can be quite high and biologically unfeasible.

Previously, our group reported a linker-free polymersome composite system with tunable sensitivity to light. Polymersomes encapsulating luminal solute (ferritin or dextran) and a membrane encapsulated meso-to-meso ethyne-bridged bis[(porphinato)zinc] (PZn_2) chromophore exhibited membrane destabilization and rupture upon exposure to light [15-17]. The luminal solute functioned to stabilize the inner leaflet of the bilayer membrane, while PZn_2 (a low fluorescent quantum yield chromophore [18]) acted as a local heating agent upon excitation. The resulting asymmetric membrane stretching due to heating effects during light excitation caused the vesicles to rupture. A limitation to our previous work was the excitation wavelength (blue-green light) and mode of light delivery (multi-line confocal lasers). The translation to a biologically relevant system with our platform would be challenging due to the strong absorption and scattering of blue-green light by hemoglobin, deoxyhemoglobin, melanin, and other proteins [19]. In the work presented here, we report an optimization of our existing platform where we cause light-induced rupture of micron-sized polymersomes with near infrared light at biologically relevant light doses. We compare the release of a model small molecule drug (sulforhodamine B) from two different polymersomes

composed of a soft (PEO$_{14}$-b-PBD$_{22}$, denoted OB14.5) and stiffer membrane (PEO$_{30}$-b-PBD$_{46}$, denoted OB29).

3.3 Materials and Methods

3.3.1 Materials

Poly(ethylene oxide)-poly(butadiene), PEO$_{14}$-*b*-PBD$_{22}$ (OB14.5, MW = 1800 g/mol) and PEO$_{30}$-*b*-PBD$_{46}$ (OB29, MW = 3800 g/mol) were purchased from Polymer Source (Montreal, Canada). A molecular weight series of Dextran (Leuconostoc mesenteroides and Leuconostoc spp.), Optiprep, and octyl β-D-glucopyranoside were purchased from Sigma Aldrich (St. Louis, MO). Methylene chloride (HPLC grade), phosphate buffered saline (PBS), and sucrose were purchased from Fisher Chemicals (Pittsburgh, PA). The meso-to-meso ethyne bridged (porphinato) zinc(II) dimer (PZn$_2$, MW = 2123 g/mol) was synthesized by the Therien lab as previously described [18].

3.3.2 Polymersome preparation

Polymersomes were prepared using thin-film rehydration. 1mM OB polymer (OB14.5 or OB29) with PZn$_2$ at a molar ratio of 10:1 (polymer:fluorophore) were dissolved in methylene chloride. 200µL of this solution was deposited on a roughened Teflon strip and evaporated for 24 hours. Dextran at the desired molecular weight was dissolved at 5, 10, and 20 mg/mL in 290 mOsm sucrose. Sulfrorhodamine B was also dissolved in the sucrose solution with dextran at a concentration of 100mM. The resulting hydration solution was added to the OB-PZn$_2$ composite film and hydrated at 65ºC for 16 hours. Following the hydration period, the films were vortexed for one minute, which resulted in the spontaneous assembly of NIR emissive polymersomes, containing PZn$_2$ in the hydrophobic membrane and Dextran and sulforhodamine B in the

aqueous core. The polymersomes were purified from unencapsulated Dextran and sulforhodamine B by centrifugation in a step gradient. The top layer contained the polymersome sample diluted in iso-osmotic PBS and the bottom layer contained a solution of sucrose and density gradient medium (80% sucrose/20% Optiprep by volume). The sample was spun at 10,000 RPM for 1 hour at 4°C. The polymersomes migrated to the interface of the step gradient and were retrieved with a syringe. The polymersome sample was dialyzed against iso-osmotic PBS to remove any trace Dextran, sulforhodamine B, and Optiprep.

3.3.3 Photodestruction of polymersomes and quantification of release

A 690 nm diode laser (Model BWF2-690-1.0-400, B&W TEK Inc.) was used to illuminate the polymersomes in a well plate and cause photodestruction. The fluence rate was modulated to 200 mW/cm^2 and delivered via a microlens tipped fiber. The total light dose varied was varied to 100 J/cm^2. Post illumination, the released sulforhodamine B was separated from the polymersomes via centrifugation in Amicon centrifugal filters (NMWCO 10kDa). The fluorescence of the sulfrorhodamine B (λ_{ex} = 480 nm, λ_{em} = 580 nm) in the filtrate was measured using a Jobin Yvon Fluoromax-4 spectrofluorometer. 100% release was measured by lysing the polymersomes with 30mM octyl β-D-glucopyranoside. The fractional release (f_r) was calculated using the following formula

$$f_r = \frac{F - F_0}{F_{OGP} - F_0}$$

Equation 3.1

where F_{OGP} is the fluorescence of the lysed polymersomes, F is the fluorescence of the treated polymersomes, and F_0 is the fluorescence of the untreated sample.

3.4 Results and Discussion

3.4.1 Polymersome deformation upon illumination

Polymersomes synthesized from OB14.5 polymer were subjected to both confocal illumination and 690 nm diode illumination to visualize membrane deformation and rupture (Figure 3-1B-C). OB14.5 polymersomes subjected to confocal illumination ruptured very quickly since the excitation wavelengths corresponded with the peak PZn_2 absorption (Figure 3-1A). Additionally, the laser energy per unit area (fluence rate) was extremely high because the laser spot size is on the order of hundreds of nanometers[1]. We transitioned the illumination to a 690 nm diode laser with a larger spot size (several centimeters) and illuminated the polymersomes for 250 or 500 seconds at 200 mW/cm^2 for a total light dose of 50 and 100 J/cm^2, respectively. The 690 nm laser was chosen because it corresponded to the PZn_2 absorption peak in the near infrared. During illumination, polymersomes underwent shrinkage and rupture and left behind debris, which can be visualized in Figure 3-3C. We next sought to quantify the rupture of the polymersomes by determining the release of a small fluorescent molecule, sulforhodamine B. The absorption of sulforhodamine B does not interfere with PZn_2 absorption (Figure 3-1A).

---

[1] $r_{Airy} = \frac{1.22\lambda}{2\,N.A.} = \frac{1.22(488nm)}{2(1.3)} = 230\,nm$
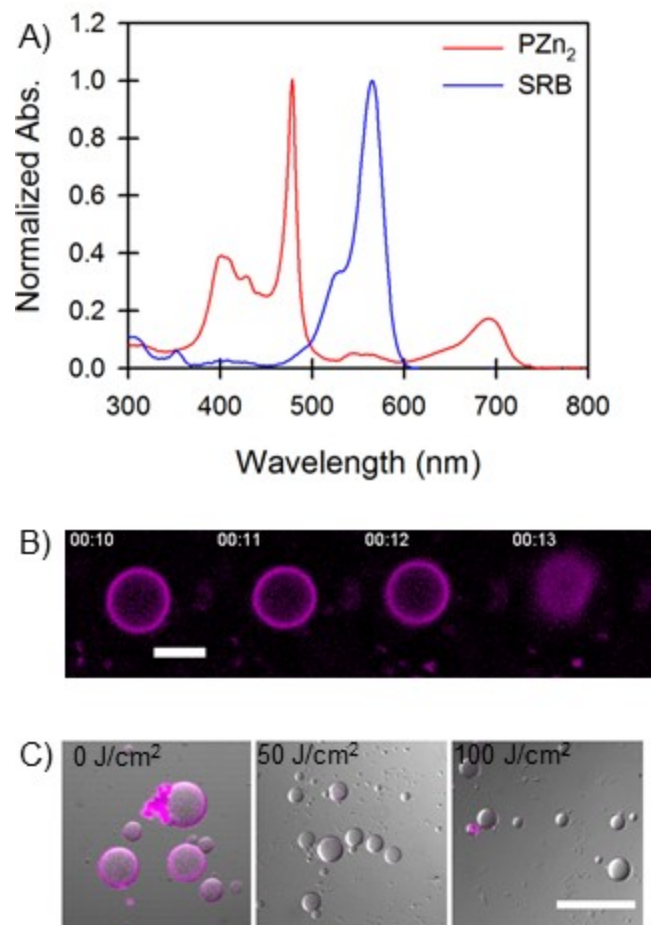
Figure 3-1: OB14.5 polymersome deformation and rupture. Polymersomes contain 10 mol% PZn_2 in the membrane and 100 kDa dextran at 10 mg/mL in the core. A) Normalized absorbance of PZn_2 within OB14.5 polymersomes and sulforhodamine B (SRB) in PBS. B) Polymersomes were exposed to confocal illumination (λ_{ex} = 458, 488, 515, 543, and 633 nm) corresponding to the peaks in PZn_2 absorption. Time-lapsed confocal images show an intact polymersome followed by complete rupture. Scale bar = 10 μm and time stamp is given in seconds. C) Confocal micrographs of polymersomes illuminated with 690 nm diode laser at 200 mW/cm^2 for a total light dose of 50 and 100 J/cm^2. Polymer debris can be seen indicating polymersome rupture. Scale bar = 100 μm. The purple fluorescence corresponds to PZn_2 emission.

3.4.2 Dependence of dextran MW and concentration on SRB release

We investigated the effects of dextran concentration and molecular weight on the release of sulforhodamine B from the aqueous core of OB14.5 polymersomes (Figure 3-2). Three different molecular weights (10, 40 and 100 kDa) and concentrations (5, 10, and 20 mg/mL) of dextran were encapsulated within the polymersomes containing 10 mol% PZn_2 in the membrane.
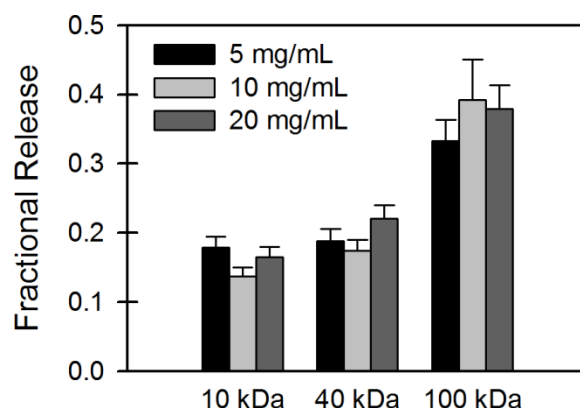
Figure 3-2: Effect of dextran MW and concentration on SRB release from OB14.5 polymersomes. Polymersomes were illuminated at 200 mW/cm^2 for a total light dose of 100 J/cm^2. Dextran at three different concentrations and molecular weights were encapsulated in the aqueous core of polymersomes containing 10 mol% PZn$_2$ in the membrane. Fractional release was determined by scaling and normalizing SRB emission between the untreated case (0% release) and after addition of the non-ionic surfactant octyl-β-D-gluopyranoside (OGP, 100% release). Error bars indicate standard deviation. N = 3 for each condition.

A modest SRB release of about 15-20% was observed for 10 and 40 kDa at all concentrations after treatment with 690 nm at a light dose of 100 J/cm^2. The fractional release increased to about 35-40% for the OB14.5 polymersomes containing 100 kDa dextran. Control polymersomes that contained either dextran or PZn$_2$ (but not both) had negligible release. We found that the key determinant in polymersome rupture was the molecular weight of the dextran and not the concentration. Larger molecular weight dextrans are more amphiphilic than smaller dextrans and as such have the ability to interact with bilayer membranes and lower the membrane elastic modulus [21-23]. Previous work in our lab with OB29 polymersomes has shown that high molecular weight dextran lowered the membrane elastic modulus of polymersomes compared to control polymersomes containing no dextran, and that OB29 polymersomes were softer than the more rigid OB18 polymersomes [16]. We expect this trend to continue and that OB14.5 polymersomes are softer than OB29 polymersomes.

3.4.3 Light dose dependence on SRB release from OB14.5 and OB29 polymersomes

From the previous study, we identified that the dextran molecular weight and not its concentration within the polymersome determined the release from polymersomes. For subsequent studies, we investigated the light-dose response of OB14.5 and OB29 polymersomes encapsulating 100 kDa dextran at 10 mg/mL with 10 mol% PZn_2 in the membrane (Figure 3-3). After illuminating the samples with a 690 nm laser, we separated the intact polymersomes from the released SRB and quantified the relative amount of released SRB using fluorescence.
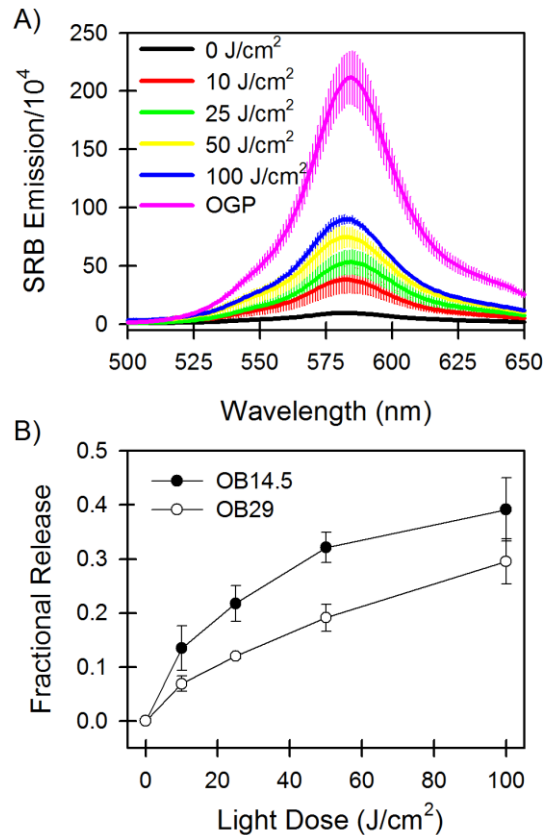
Figure 3-3: Light-dose dependence on SRB release from OB14.5 and OB29 polymersomes. Polymersomes synthesized with 100 kDa dextran at 10 mg/mL in the lumen and 10 mol% PZn_2 in the membrane. Polymersomes illuminated with 690 nm laser at 200 mW/cm^2. A) Representative emission scans of SRB released from OB14.5 polymersomes upon treatment with 0, 10, 25, 50, and 100 J/cm^2 of light. 100% release was determined by adding a non-ionic surfactant, octyl-β-D-gluopyranoside. B) Release curves of SRB from OB14.5 and OB29 polymersomes after illumination. Error bars indicate standard deviation. N = 3 for each condition.

As shown in Figure 3-3A, SRB emission increased as a function of light dose for OB14.5 polymersomes. A similar analysis was conducted for OB29 polymersomes as well. We scaled and normalized the emission scans to generate release curves as a function of light dose (Figure 3-3B). OB14.5 polymersomes released more SRB than OB29 polymersomes at all light doses. We expect this to be the case since we calculated the K_a for OB14.5 polymersomes to be less than the K_a for OB29 polymersomes (i.e. OB14.5 formed softer membrane). OB29 polymersomes were better able to withstand the asymmetric stretching that occurred during excitation (and PZn_2 heating).

As a control, we measured the solution temperature post illumination to ensure that drastic fluctuations in temperature were not causing photorelease of SRB from polymersomes. After 100 J/cm^2 of light delivery, the temperature of the polymersome solution increased by a maximum of 3ºC from room temperature. This result was initially surprising because theoretical calculations suggest that a system of water initially at room temperature needs a total of 130 J/cm^2 of energy to completely vaporize (assuming a total mass of 0.05g water, which was our sample volume that was illuminated). However, this thermodynamic calculation requires an adiabatic system, which our system was not. The supplied radiative energy was absorbed by the porphyrin and converted to thermal energy. The net effect was a small increase in solution temperature and polymersome rupture.

3.5 Conclusion

We showed that giant polymersomes containing a porphyrin dimer (PZn_2) in the hydrophobic membrane and dextran in the aqueous lumen ruptured in response to 690 nm laser illumination. The polymersomes were responsive up to 100 J/cm^2 of light

delivery, after which the release fraction started to plateau. We found that dextran molecular weight (and not concentration) is a determining factor in the release of sulforhodamine B from the aqueous lumen of polymersomes.

3.6 References

1. Discher, B.M., *Polymersomes: Tough Vesicles Made from Diblock Copolymers.* Science, 1999. **284**(5417): p. 1143-1146.

2. Levine, D.H., et al., *Polymersomes: a new multi-functional tool for cancer diagnosis and therapy.* Methods (San Diego, Calif.), 2008. **46**: p. 25-32.

3. Sood, N., et al., *Biodegradable Polymersomes for the Delivery of Gemcitabine to Panc-1 Cells.* Journal of Pharmaceutics, 2013. **2013**: p. 10.

4. Kamat, N.P., et al., *Single-Vesicle Patterning of Uniform, Giant Polymersomes into Microarrays.* Small, 2013. **9**(13): p. 2272-2276.

5. Kamat, N.P., et al., *Sensing membrane stress with near IR-emissive porphyrins.* Proceedings of the National Academy of Sciences of the United States of America, 2011. **108**: p. 13984-9.

6. Ahmed, F., et al., *Shrinkage of a rapidly growing tumor by drug-loaded polymersomes: pH-triggered release through copolymer degradation.* Molecular pharmaceutics, 2006. **3**: p. 340-50.

7. Napoli, A., et al., *Oxidation-responsive polymeric vesicles.* Nat Mater, 2004. **3**(3): p. 183-9.

8. Cheng, Z.L., D.L.J. Thorek, and A. Tsourkas, *Porous Polymersomes with Encapsulated Gd-Labeled Dendrimers as Highly Efficient MRI Contrast Agents.* Advanced Functional Materials, 2009. **19**(23): p. 3753-3759.

9. Ghoroghchian, P.P., et al., *Bioresorbable Vesicles Formed through Spontaneous Self-Assembly of Amphiphilic Poly(ethylene oxide)-block-polycaprolactone.* Macromolecules, 2006. **39**: p. 1673-1675.

10. Gerweck, L.E. and K. Seetharaman, *Cellular pH Gradient in Tumor versus Normal Tissue : Potential Exploitation for the Treatment of Cancer Advances in*

Brief Cellular pH Gradient in Tumor versus Normal Tissue : Potential Exploitation for the Treatment of Cancer1. 1996: p. 1194-1198.

11. Gillies, R.J., et al., *MRI of the tumor microenvironment.* Journal of magnetic resonance imaging : JMRI, 2002. **16**: p. 430-50.

12. Vander Heiden, M.G., L.C. Cantley, and C.B. Thompson, *Understanding the Warburg effect: the metabolic requirements of cell proliferation.* Science (New York, N.Y.), 2009. **324**: p. 1029-33.

13. Cabane, E., et al., *Photoresponsive polymersomes as smart, triggerable nanocarriers.* Soft Matter, 2011. **7**(19): p. 9167-9176.

14. Kumar, S., et al., *Near-infrared light sensitive polypeptide block copolymer micelles for drug delivery.* Journal of Materials Chemistry, 2012. **22**: p. 7252.

15. Kamat, N.P., et al., *Sensing membrane stress with near IR-emissive porphyrins.* Proceedings of the National Academy of Sciences of the United States of America, 2011. **108**: p. 13984-13989.

16. Kamat, N.P., et al., *A Generalized System for Photo-Responsive Membrane Rupture in Polymersomes.* Advanced functional materials, 2010. **20**: p. 2588-2596.

17. Robbins, G.P., et al., *Photoinitiated destruction of composite porphyrin-protein polymersomes.* Journal of the American Chemical Society, 2009. **131**: p. 3872-4.

18. Duncan, T.V., et al., *Exceptional near-infrared fluorescence quantum yields and excited-state absorptivity of highly conjugated porphyrin arrays.* Journal of the American Chemical Society, 2006. **128**: p. 9000-1.

19. König, K., *Multiphoton microscopy in life sciences.* Journal of Microscopy, 2000. **200**(2): p. 83-104.

20.   Evans, E. and D. Needham, *Physical properties of surfactant bilayer membranes: thermal transitions, elasticity, rigidity, cohesion and colloidal interactions.* The Journal of Physical Chemistry, 1987. **91**: p. 4219-4228.

21.   Decher, G., et al., *INTERACTION OF AMPHIPHILIC POLYMERS WITH MODEL MEMBRANES.* Angewandte Makromolekulare Chemie, 1989. **166**: p. 71-80.

22.   Ringsdorf, H., B. Schlarb, and J. Venzmer, *MOLECULAR ARCHITECTURE AND FUNCTION OF POLYMERIC ORIENTED SYSTEMS - MODELS FOR THE STUDY OF ORGANIZATION, SURFACE RECOGNITION, AND DYNAMICS OF BIOMEMBRANES.* Angewandte Chemie-International Edition, 1988. **27**(1): p. 113-158.

23.   Santore, M.M., et al., *Effect of surfactant on unilamellar polymeric vesicles: Altered membrane properties and stability in the limit of weak surfactant partitioning.* Langmuir, 2002. **18**(20): p. 7299-7308.

4 Light Responsive Nano-polymersomes for the Photodynamic Therapy of Ovarian Cancer

4.1 Summary

Photodynamic therapy (PDT) requires the administration of a photosensitizer followed by illumination of diseased tissue with light to produce toxic singlet oxygen. Many photosensitizers currently being used in PDT are hydrophobic and require a delivery vehicle to increase their solubility and absorption both *in vitro* and *in vivo*. A standardly used construct is to embed the photosensitizer benzoporphyrin derivative monoacid A (BPD-MA) into liposomes. Here, we explore an alternative: the encapsulation and delivery of BPD-MA from a polymersome assembled from poly(ethylene oxide)–b-poly(butadiene) di-block co-polymer. We studied the intracellular uptake and toxicity of both the polymersomal and liposomal formulations and found that the polymersomes produced greater *in vitro* toxicity despite generating less singlet oxygen. The polymersomes served to protect BPD-MA from being leached and associated with serum proteins. *In vivo* studies showed that while BPD-MA-loaded

polymersomes and verteporfin had similar biodistribution profiles, the polymersome formulation performed at par with verteporfin in reducing tumor growth despite being present in a lower concentration within the tumor.

4.2 Introduction

Photodynamic therapy (PDT) is a clinically approved cancer therapy that can selectively kill malignant tissue. This therapy has been approved by the FDA for the palliation or treatment of diseases that include high-grade dysplasia (HGD) associated with Barrett's Esophagus (BE), esophageal cancer, and non-small cell lung cancer. Additionally, clinical trials are being performed to determine the efficacy of PDT for bladder, mesothelioma, head and neck, pancreatic, and ovarian cancer, among other malignancies [1-6]. PDT is gaining wider acceptance in the clinic due to its demonstrated efficacy in treating more widespread superficial diseases, its lack of cumulative toxicities (and thus repeatability), and its suitability for combination with other therapeutic approaches [7-10].

PDT requires the administration of a drug (photosensitizer) and illumination of the diseased tissue [11, 12]. Light absorption by the photosensitizer produces reactive oxygen species, including singlet oxygen, that damage cellular components. Neither the photosensitizer nor the light is toxic by itself. The subcellular localization of photosensitizer is important for phototoxicity because the intracellular diffusion length for singlet oxygen is about 20 nm, and photodamage occurs very close to the site of the photosensitizer [13]. Additionally, when performed *in vivo*, PDT can lead to tumor cell death through the effects of treatment on host cells and tissues. For example, PDT damage of the microvasculature can contribute to therapeutic effect by shutting down

the blood vessels feeding the tumor [14, 15]. Treatment can also elicit an immune response that is associated with the release of inflammatory cytokines and active recruitment of leukocytes to the site of photodamage, potentially initiating the development of anti-tumor immunity [16].

Nanoparticle-based PDT has been studied for a wide variety of photosensitizers and nanovehicles. Lipid formulations of photosensitizers have received particular attention because this method of delivery has gained approval from the FDA in the forms of liposomal doxorubicin and daunorubicin, which were approved in the late 1990s. Liposomes can provide the necessary hydrophobic environment to solubilize hydrophobic photosensitizers, and additional modifications such as PEGylation to increase plasma circulation time and the conjugation of monoclonal antibodies for tumor targeting can render this class of nanoparticles quite potent [17-19]. Mir *et al.* integrated benzoporphyrin derivative monoacid A (BPD-MA) within targeted liposomes and showed tumor cell killing in an *in vitro* ovarian cancer model [19]. Polymeric-based nanoparticles have also been utilized for PDT and offer an advantage over lipids due to the variety of building blocks and surface functionality [20, 21]. Ding *et al.* used a non-covalently encapsulated protoporphyrin IX (PPIX) within polymeric micelles and showed a photosensitizer-dose response in the killing of lung cancer cells *in vitro* [22]. dePaula *et al.* created biodegradable nanospheres to encapsulate chloroaluminium phthalocyanine (AlClPc) and showed moderate phototoxicity in human fibroblast culture [23].

Verteporfin (benzoporhyrin derivative monoacid A, BPD-MA) is a second-generation lipophilic photosensitizer that produces singlet oxygen at high quantum yield ($\Phi_\Delta = 0.78$) [24, 25]. Current FDA-approved indications for verteporfin are limited to the treatment of subfoveal choroidal neovascularization (CNV) in age-related macular

degeneration (AMD) [26-28]. Ovarian cancer is the fifth leading cause of cancer deaths in women and represents another possible indication for PDT mediated by BPD-MA [29]. The work presented here discusses the efficacy and toxicity of BPD-MA encapsulated in polymersomes in treatment directed toward an ovarian cancer cell line and tumor model. Polymersomes are self-assembled bilayer vesicles synthesized from diblock copolymers capable of encapsulating large payloads of both hydrophilic and hydrophobic compounds [30, 31]. The capacity for carrying large amounts of hydrophobic drugs comes from hyperthick hydrophobic core of polymersome membranes, which is conveyed by the large molecular weight of the polymer used to assemble the membrane [32]. They also confer other advantages over liposomes including increased mechanical robustness and relative ease of surface functionalization [33-35]. Like liposomes, they have the capacity to encapsulate both hydrophilic and hydrophobic molecules. Here, we compare the performance of polymersomes made from poly (ethylene oxide) – b – poly (butadiene), designated OB14.5, loaded with 40% BPD (OB14.5-40% BPD), with that of verteporfin in a model for ovarian cancer.

4.3 Materials and Methods

4.3.1 Materials

Reagents were obtained as follows: Singlet oxygen sensor green® (SOSG) from Life Technologies (Grand Island, NY); Benzoporphyrin derivative monoacid A (BPD-MA) from U.S. Pharmacopeia (Rockville, MD); Visudyne™ from Valeant Pharmaceuticals International, Inc. (Bridgewater, NJ); and Poly(butadiene(1,2)addition-b-ethylene oxide) (PEO(0.60k)-PBD(1.2k), OB14.5) from Polymer Source Inc. (Montreal, Canada). The meso-to-meso ethyne bridged (porphinato) zinc(II) trimer (PZn$_3$) with a 9-methoxy-1,4,7-trioxanonyl substituent on one aryl group and a more hydrophobic 3,3-dimethyl-1-

butyloxy substituent on the other, was synthesized as previously described [36]. Methylene chloride, methylene blue for colony staining, phosphate buffered saline (PBS), sodium acetate trihydrate, and sodium chloride were purchased from Fisher Chemicals (Pittsburgh, PA). Centrifugal filter units were purchased from Millipore (Billerica, MA).

4.3.2 Cell Line

OVCAR-5 cells (Charles River, NCI Frederick, Frederick, MD) were maintained in RPMI 1640 media (Invitrogen) with 10% fetal bovine serum (FBS, Sigma) and 1% Pen/Strep. Media was supplemented with L-glutamine (1%) after three weeks. Cells were cultured in a humidified incubator at 37^0C under an atmosphere of 5% CO_2.

4.3.3 OB14.5-40% BPD Polymersome Preparation

BPD-loaded polymersomes were prepared via thin film rehydration. Briefly, 1mM OB14.5 with BPD at a molar ratio of 1:0.4 (polymer:BPD) were dissolved in methylene chloride. 100 µL of the polymer-drug solution was cast on a roughened 1 cm^2 Teflon surface in a scintillation vial and allowed to dry under vacuum for 24 hours. 1.5mL of PBS (for in vitro experiments) or 0.9% saline (for in vivo experiments) was added to the vial, and the composite film was sonicated for 60 minutes to generate nanometer-sized polymersomes containing BPD at a molar ratio of 40% in the membrane. Polymersomes were subjected to five cycles of freeze/thaw in liquid N_2 and hot water to narrow the size distribution of polymersomes. The final drug concentration in polymersomes was measured by UV/Vis absorbance with an extinction coefficient of 0.044 cm^{-1} $(µg/mL)^{-1}$ at 690 nm. The polymersome sample was diluted to 20 ng/mL for in vitro experiments. Five to eight vials were prepared and combined for in vivo experiments. The final

concentration of 0.1 mg/mL for mice injections was prepared by concentrating the total volume from five to eight vials in 50 kDa Amicon centrifugation tubes.

4.3.4 Verteporfin Preparation

Visudyne™ (verteporfin for injection) was weighed and hydrated with 1mL of PBS (for *in vitro* experiments) or 0.9% saline (for *in vivo* experiments). The concentration of active compound (BPD) in verteporfin was measured monthly, and varied from 1.4 – 1.9 mg BPD/100 mg. The active drug concentration was diluted to 20 ng/mL for *in vitro* experiments and 0.1 mg/mL for *in vivo* experiments.

4.3.5 Determination of Singlet Oxygen Production

Singlet oxygen sensor green® (SOSG) was protected from light and stored at -20ºC. Fresh aliquots were prepared before the study. Singlet oxygen production was determined both in PBS and 5% serum. 180 µL of 1 µM BPD-MA as verteporfin or OB14.5-40% BPD was added in wells in a 96 well plate in triplicate. 20 µL of a 15 µM SOSG solution was added to each well. The samples were illuminated at 690 nm with a fluence rate of 40 mW/cm^2. The total delivered light dose was 0, 5, 10, 20, 50, and 100 J/cm^2.

4.3.6 Photodynamic Therapy

A 690 nm diode laser (Model BWF2-690-1.0-400, B&W TEK Inc.) was used to deliver monochromatic light for *in vitro* and *in vivo* experiments. For *in vitro* experiments (clonogenic assays), the laser spot size was focused to 6 cm via a microlens-tipped optical fiber and an attenuator was used to modulate the fluence rate to 40 mW/cm^2, as measured by a power meter (LabMaster power meter; Coherent, Auburn, CA). OVCAR-

5 cells were treated with OB14.5-40% BPD or verteporfin for 12 h in T-75 flasks to allow for drug internalization. Following the incubation period, cells were washed with Hank's buffered saline solution (HBSS), moved to 6 cm dishes, and treated with 0, 5, 10, 15, or 20 J/cm^2 of light. For *in vivo* experiments, mice were injected via tail vein with 1 mg/mL BPD as either polymersomes or verteporfin. The fluence rate was modulated to 75 mW/cm^2 with a spot diameter of 1.1 cm to cover the mouse tumor. The total delivered light dose was 75 J/cm^2.

4.3.7 Clonogenic Assay

OVCAR-5 cells were incubated with OB14.5-40% BPD or verteporfin at an equivalent BPD concentration of 20 ng/mL in low serum RPMI 1640 media (5% FBS, 1% Pen/Strep) for 12 hours. Following the incubation period, the cells were washed with HBSS to remove uninternalized drug. Trypsin (0.05%) was added to detach the cells from the flask and the cells were counted. The PDT treatment is described above. A total of 2 x 10^5 cells were treated in a 6 cm dish with 0, 5, 10, 15 or 20 J/cm^2 of 690 nm light at 40 mW/cm^2. Following illumination, cells were plated in 10 cm tissue culture dishes in RPMI 1640 complete media (10% FBS, 1% Pen/Strep). Cells were plated at concentrations of 10^2, 10^3, 10^4, or 10^5 cells per dish depending on the treatment condition. Dishes were incubated for 10-12 days and removed when the control dishes (no treatment) formed visible colonies. After removal of the media, a solution of 0.25% methylene blue (in 30% ethanol) was used to stain and fix the colonies. From plates that contained 10-300 colonies (a colony defined by 50 or more cells) the surviving fraction (SF) was defined as follows:

- Plating efficiency = number of colonies formed by untreated cells / number of cells plated

- Surviving fraction = (number of colonies formed by treated cells) / (number of cells plated * plating efficiency)

4.3.8 Cryogenic Transmission Electron Microscopy

Cryogenic transmission electron microscopy was performed at the Krishna P. Singh Center for Nanotechnology at the University of Pennsylvania (Philadelphia, PA). Lacey formvar/carbon grids (Ted Pella) were rinsed with chloroform to dissolve and remove the formvar template. Grids were carbon coated with a Quorum Q150T ES carbon coater (Quorum Technologies, UK) and cleaned on both sides with hydrogen/oxygen plasma for 15 seconds using Solarus Advanced Plasma System 950 (Gatan, Pleasanton, CA). 2 µL of either the polymersome sample or verteporfin was deposited on the lacey/formvar grid and inserted into a cryoplunger (Gatan Cp3, Gatan). The sample was blotted by hand with filter paper and plunged into liquid ethane. Samples were transferred to a Gatan CT3500TR cryoholder. The cryoholder was immediately inserted into a JEOL 2100 HRTEM (JEOL, Tokyo, Japan) operating at 200 kV. Images were taken with an Orius SC200 digital camera.

4.3.9 *In Vitro* Cellular Internalization and Serum Binding

OVCAR-5 cells were separately incubated with 20 ng/mL verteporfin and OB14.5-40% BPD polymersomes for predefined lengths of time (15 minutes, 3 hours, 6 hours, 12 hours, and 24 hours) in low serum RPMI 1640 media (5% FBS, 1% Pen/Strep) in 6 well plates. After the indicated incubation period, the cells were rinsed three times with RPMI 1640 media containing no serum to remove uninternalized drug. After the washing step, cells were removed from the wells with 0.05% Trypsin. A small aliquot was used to determine the cell density using a coulter counter. The remaining cells were

centrifuged to a pellet (1500 RPM, 5 minutes), and resuspended in 0.5 mL SOLVABLE^{TM} (Perkin Elmer) to completely digest the cells. The cells were digested for 4 hours at 50°C in the dark in amber glass vials. After the digestion period, 0.5 mL of MilliQ water at room temperature was added to dilute and cool the tissue sample. 0.6 mL of the total volume was assayed for BPD-MA content using a Fluoromax-4 spectrophotometer (Jobin Yvon) (λ_{ex} = 435 nm, λ_{em} = 630 – 750 nm). The peak fluorescence emission at 690 nm was used to determine the concentration of BPD-MA in solution. The concentration of BPD-MA in solution was determined from a calibration curve. For serum binding experiments, verteporfin or OB14.5-40% BPD polymersomes were incubated at 20 ng/mL BPD-MA with 5% calf serum at 37°C for predefined lengths of time (15 min, 3 h, 12 h, and 24 h) and kept in the dark. After the incubation period was complete, the nanoparticles were separated from the serum protein using an amicon filter unit (MWCO 1000kDa). The BPD content was measured via fluorescence at its emission peak of 690 nm. As a control, verteporfin and OB14.5-40% BPD polymersomes were incubated with PBS.

4.3.10 *In Vivo* Biodistribution

4.3.10.1 Live-Animal Longitudinal Study

Prior to drug administration, OVCAR-5 cells were injected subcutaneously on both the left and right shoulders of female Athymic nude mice (30 µL per injection at a density of 2.67 x 10^8 cells/mL). Mice were maintained on a chlorophyll-free diet (Harlan Laboratories) 10 days prior to imaging. After the tumors reached approximately 100 mm^3 in size, mice were injected via tail-vein with the following formulations of drug or fluorescent labels: verteporfin, OB14.5-40% BPD, OB14.5-40% BPD/2.5% PZn$_3$ (dual-labeled polymersome), and OB14.5-2.5% PZn$_3$. The BPD concentration was maintained at 0.1 mg/mL for the formulations containing photosensitizer. The molar ratio of

BPD:PZn$_3$ in the dual-encapsulated polymersome was kept at 16:1. At predefined time points post tail-vein injections (15 minutes, 1 hour, 3 hours, 8 hours, and 24 h), anesthetized mice (inhalation of isoflurane) were imaged on the LI-COR Pearl® Impulse Small Animal Imaging System (LI-COR Biosystems). BPD signal was captured in the 700 channel (λ_{ex} = 685 nm, λ_{em} = 720 nm) and PZn$_3$ signal was captured in the 800 channel (λ_{ex} = 785 nm, λ_{em} = 820 nm). A white-light image was captured in the white channel. The imager resolution was set to 85 µm. Mice were imaged on the left and right sides to detect signal from the left and right tumors, and the ventral position to detect signal from the abdominal organs. Images were analyzed with the Pearl Impulse Software by drawing ROIs over the tumor, upper abdomen, and lower abdomen and recording the mean signal per area.

4.3.10.2 End-Point Organ Biodistribution

Prior to drug administration, OVCAR-5 cells were injected subcutaneously on both the left and right shoulders of female Athymic nude mice (30 µL per injection at a density of 2.67 x 108 cells/mL). After the tumors reached approximately 100 mm3 in size, mice were injected with equivalent dose of verteporfin or OB14.5-40% BPD at 0.1 mg/mL BPD via tail vein injection. At predefined time points (15 min, 3 h, 6 h, 16 h, and 24 h), the mice were anesthetized with an intraperitoneal injection of ketamine/xylazene. Whole blood was collected by cardiac puncture in sodium heparin-coated syringes. After confirmation of death, tumor, liver, intestines, and spleen were harvested for analysis of BPD-MA. All organs were stored in cryo vials at -80ºC. Plasma was isolated as follows: whole blood was collected in 1 mL Eppendorf tubes and centrifuged at 1000 RPM for 15 min at 22ºC. The top layer, which included plasma and some white blood cells, was carefully decanted and spun a second time at the same conditions as above. The purified plasma was collected and stored at -80 ºC.

During processing for spectrofluorometric analysis, tweezers were used to squeeze-out and remove any remaining food in the GI tract (intestines isolation). 30 – 50 mg of tissue was weighed in 10 mm dishes and minced with surgical scissors. Minced tissue was placed into glass amber vials and 0.5 mL of SOLVABLE™ (Perkin Elmer, Waltham, MA) was added to digest the tissue. Digestion took place for 4 hours at 50ºC in the dark. After the digestion period, 0.5 mL of MilliQ water at room temperature was added to dilute and cool the tissue sample. 0.6 mL of the total volume was assayed for BPD-MA content using a Fluoromax-4 spectrophotometer (Jobin Yvon) (λ_{ex} = 435 nm, λ_{em} = 630 – 750 nm). The peak fluorescence emission at 690 nm was used to determine the concentration of BPD-MA in solution. Separately, calibration curves were generated to relate fluorescence emission at 690 nm to drug concentration for the organs of interest by adding known concentrations of verteporfin or OB14.5-40% BPD to tissue harvested from mice that received no drug treatment.

4.4 Results and Discussion

BPD-MA is a potent second generation hydrophilic photosensitizer [24]. Because of its poor solubility in aqueous environments, BPD-MA was formulated in a liposomal association and sold as Visudyne™ (verteporfin for injection). We have tested the encapsulation of BPD-MA in the hydrophobic membrane of polymersomes as an alternative delivery vehicle with the potential for high BPD-MA loading. A schematic of singlet oxygen generation by polymersome-encapsulated BPD-MA is presented in Figure 4-1.
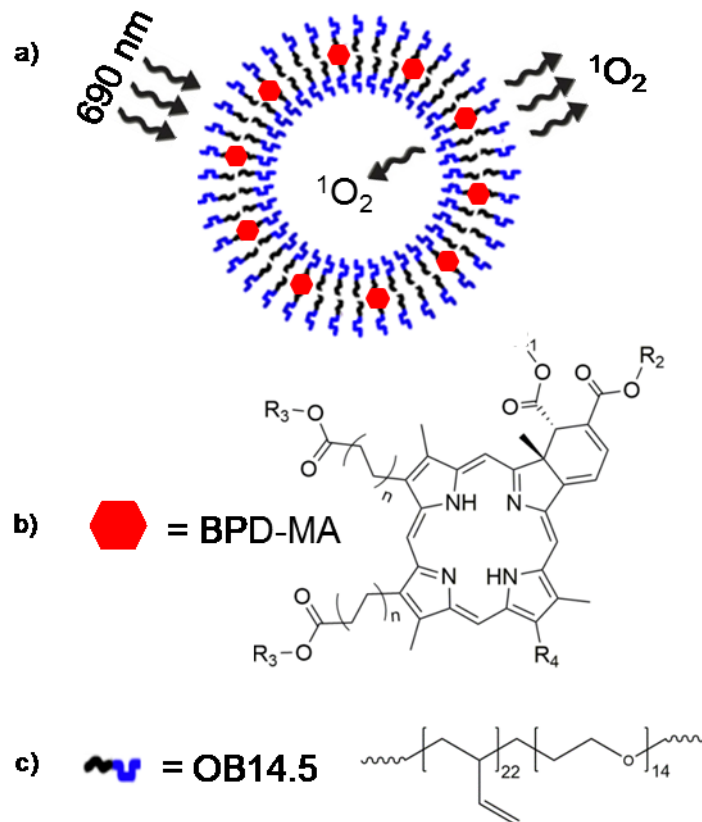
Figure 4-1: Polymersome delivery system. (a) Cartoon illustrating the encapsulation of BPD-MA in the hydrophobic core of the membrane of a polymersome. Excitation with 690 nm light causes BPD-MA to covert nearby ground-state triplet oxygen ($^3O_2$) into cytotoxic singlet oxygen ($^1O_2$). (b) Chemical structure of BPD-MA. (c) Chemical structure of the polymer OB14.5.

4.4.1 Nanoparticle characterization

Three different nanoparticle formulations were synthesized to understand the delivery and toxicity of the hydrophobic photosensitizer BPD-MA both *in vitro* and *in vivo*. Visudyne^TM (verteporfin for injection) is a liposomal formulation of BPD-MA with an active drug fraction at 1.4 – 1.9 wt%. We developed a novel formulation of BPD-MA by encapsulating it in the hydrophobic membrane of OB14.5 polymersomes at a molar ratio of 1:0.4 (polymer:BPD), with an effective weight fraction of 16 wt% BPD. We also assembled OB14.5 polymersomes with a hydrophobic NIR emissive porphyrin trimer

(PZn$_3$) [32, 36] at a molar ratio of 1:0.025 (polymer:PZn$_3$), as well as dual-labeled OB14.5 polymersomes with both BPD and PZn$_3$ at molar ratios of 0.4 and 0.025, respectively, for *in vivo* polymersome tracking.

The structure of the nanoparticles was confirmed with dynamic light scattering (DLS) and cryogenic transmission electron microscopy (cryo-TEM) (Figure 4-2a and Figure 4-2b, respectively). DLS shows that the average hydrodynamic diameters for all three polymersome formulations (BPD only, PZn$_3$ only, and dual BPD/PZn$_3$) are around 100 nm. The DLS results for verteporfin show an extremely polydisperse population ranging in size from 10 – 1000 nm. We imaged the structure of verteporfin and OB14.5-40% BPD via cryo-TEM. Verteporfin is a liposomal formulation of BPD and consisted of a heterogenous population of micelles, sheets, and vesicles. OB14.5-40% BPD polymersomes, on the other hand, were predominantly spherical vesicles with a narrower size distribution from 30 – 200 nm. Thus the polymersomes offer the advantage that size and shape can be precisely controlled. Size of nanoparticles plays an important role in their *in vivo* efficacy. Work done by Anraku and coworkers measured the residence time of polymersomes of various sizes in the plasma, tumor, liver, and spleen of mice and found that the optimal polymersome size is between 100 – 150 nm for extended plasma circulation (circulation half-life of 23 hours) [37].
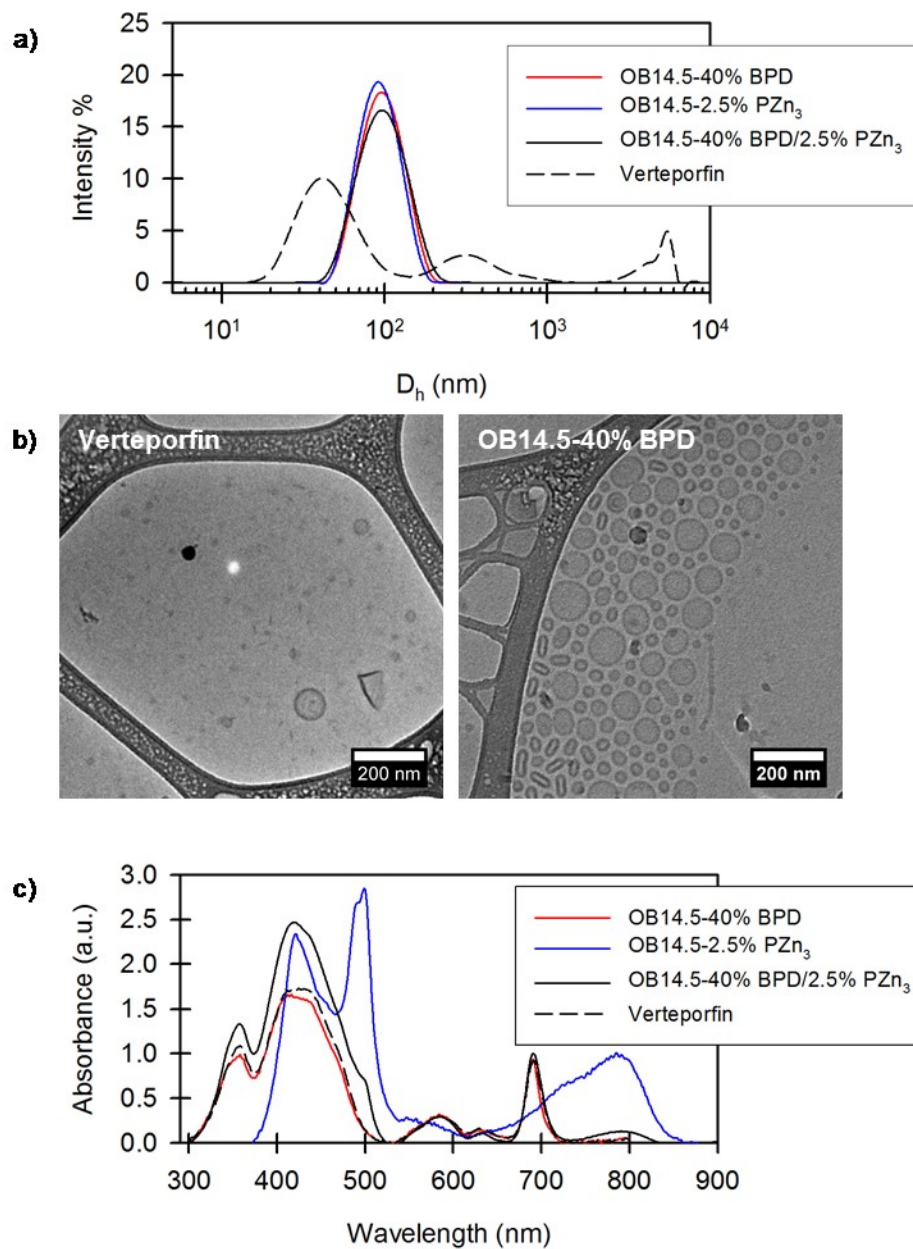
Figure 4-2: Nanoparticle characterization. (a) Dynamic light scattering showing the hydrodynamic diameter of polymersomes containing BPD, PZn$_3$, or both, and verteporfin. (b) Cryo-TEM micrographs of verteporfin and OB14.5-40% BPD. (c) UV/Vis absorbance spectra of nanoparticles containing BPD, PZn$_3$, or both, and verteporfin.

The encapsulation of the drug was confirmed via UV/vis absorbance spectroscopy (Figure 4-2c). BPD and PZn$_3$ feature NIR absorbance bands centered respectively at 690 and 794 nm.

4.4.2 *In situ* Singlet Oxygen Detection

The phototoxicity from cell-localized verteporfin and OB14.5-40% BPD is a direct consequence of the ability of these nanoparticles to generate singlet oxygen. In order to quantify the singlet oxygen production from these nanoparticles, we utilized Singlet Oxygen Sensor Green[TM] (SOSG) that captures singlet oxygen once it is released into solution and fluoresces.
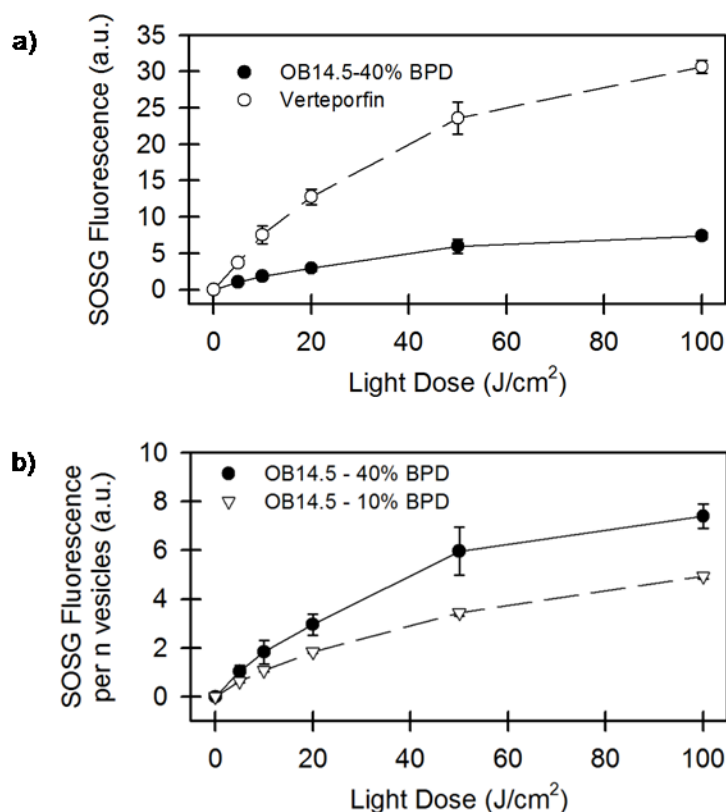
Figure 4-3: SOSG detection of Singlet Oxygen. Singlet oxygen was generated by irradiating BPD nanoparticles at 690 nm in the presence of SOSG at a fluence rate of 40 mW/cm^2. (a) Detection of singlet oxygen formation by verteporfin and OB14.5-40% BPD at the same concentration of BPD (1µM). (b) Normalized SOSG signal per *n* vesicles from OB14.5-40% BPD and OB14.5-10% BPD.

The assay can detect singlet oxygen only if it is able to diffuse out of the hydrophobic membrane of the polymersomes and into solution. We detected a greater concentration

of singlet oxygen from verteporfin than OB14.5-40% BPD at all light doses, potentially due to the loose association of BPD with the liposome and the protection of BPD by the hyperthick polymersome membrane. The high BPD-MA loading within the polymersome membrane may have also played a role in the lower singlet oxygen concentrations determined for OB14.5-40% BPD relative to that measured for BPD liposomes. It is also possible that the singlet oxygen that generated in the polymersome membrane diffused into the inner aqueous lumen where SOSG is not present. This could potentially reduce the SOSG signal.

We also compared the singlet oxygen production from polymersomes loaded with 10% and 40% BPD in the membrane by normalizing to the vesicle number. In order to equate the BPD concentration, the 10% BPD polymersomes must be present in four times the number as the 40% BPD polymersomes. After normalizing by vesicle number (Figure 4-3b), OB14.5-40% BPD did produce greater singlet oxygen than OB14.5-10% BPD, as was expected. However, we did not observe a proportional difference in singlet oxygen production between polymersomes loaded with 10% and 40% BPD, possibly due to singlet oxygen quenching. Nevertheless, we chose OB14.5-40% BPD polymersomes for *in vitro* and *in vivo* studies with the objective of killing OVCAR-5 cells due to its higher production of singlet oxygen per vesicle.

4.4.3 *In vitro* Cellular Internalization and Serum Binding

Initial in vitro studies were conducted to assess BPD internalization into OVCAR-5 cells after polymersome versus liposome (i.e. verteporfin) delivery (Figure 4-4a). OVCAR-5 cells were incubated with 20 ng/mL of BPD as either verteporfin or OB14.5-40% BPD polymersomes in low serum (5% FBS) RPMI 1640 media for predefined

lengths of time (15 minutes, 3 hours, 12 hours, and 24 hours). The concentration of drug was measured using a spectrofluorometer and normalized to the total cell count. The amount of BPD per cell increased as a function of time for both verteporfin and the polymersomal formulation and leveled off after 12 hours. The total drug content was statistically greater for polymersomes than verteporfin after 12 and 24 hours of incubation.
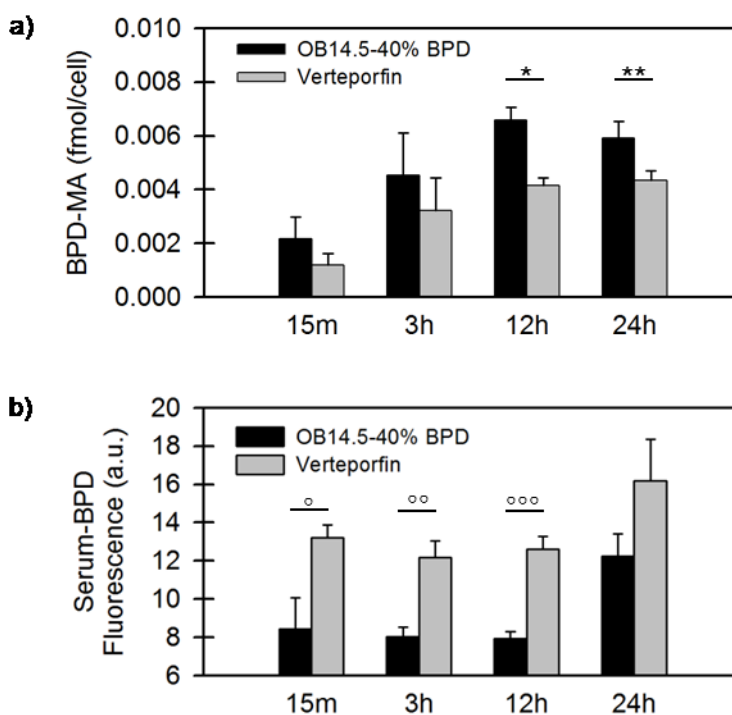
Figure 4-4: BPD uptake and serum binding. (a) BPD uptake per cell as a function of incubation time. * p = 0.005 and ** p = 0.03. (b) BPD association to serum proteins as a function of incubation time. Incubation with PBS (no serum) had negligible signal (0.032 for OB14.5-40% BPD and 0.034 for verteporfin). ∘ p = 0.02, ∘∘ p = 0.006, and ∘∘∘ p = 0.002. p-values were determined from a two-tailed student's t-test with α = 0.05. Error bars indicate standard deviation.

Because BPD-MA is a hydrophobic molecule and is known to partition into LDL proteins in circulation [38], we next explored the serum association of BPD-MA in verteporfin and OB14.5-40% BPD polymersomes (Figure 4-4b). Verteporfin and OB14.5-40% BPD polymersomes were incubated in PBS containing 5% FBS (low serum to

match the uptake study) for predefined lengths of time. A high MWCO membrane was used to separate the serum proteins from the nanoparticles and the presence of BPD was measured in the serum-containing filtrate. As shown in Figure 4-4b, BPD-MA partitions into serum proteins. We ensured that the membranes were very selective to the serum proteins – no verteporfin or polymersomes went through. As an additional control, verteporfin and polymersomes were incubated in PBS without any serum. BPD-MA did not leach into the surrounding buffer and remained associated with the nanoparticles. The decreased BPD fluorescence for serum proteins that were incubated with polymersomes suggested that the polymersomes were better able to protect the photosensitizer against serum leaching. Thus, the fraction of drug that is serum bound is much less for polymersomes than verteporfin. Based on differences in BPD association with serum at 12 h after incubation in verteporfin versus OB14.5-40%, together with the increased cell uptake of polymersome-delivered BPD at this time point, a 12 hour drug incubation period was chosen for further *in vitro* PDT studies.

4.4.4 *In vitro* PDT of OVCAR-5 Cells

OVCAR-5 cells were treated with 20 ng/mL of BPD for 12 hours as either verteporfin or OB14.5-40% BPD, followed by illumination at 690 nm. Cell survival decreased as a function of increasing light dose for both formulations (Figure 4-5a), thus the greatest difference in cytotoxic effect was detected at the highest light dose of 20 J/cm^2. At this dose, PDT led to a surviving fraction of 0.008 for verteporfin and 0.002 for OB14.5-40% BPD (a 4-fold difference in survival). Controls with drug only and light only (20 J/cm^2) showed no toxicity when compared to the case without treatment (surviving fractions of 1.05 and 0.98, respectively).
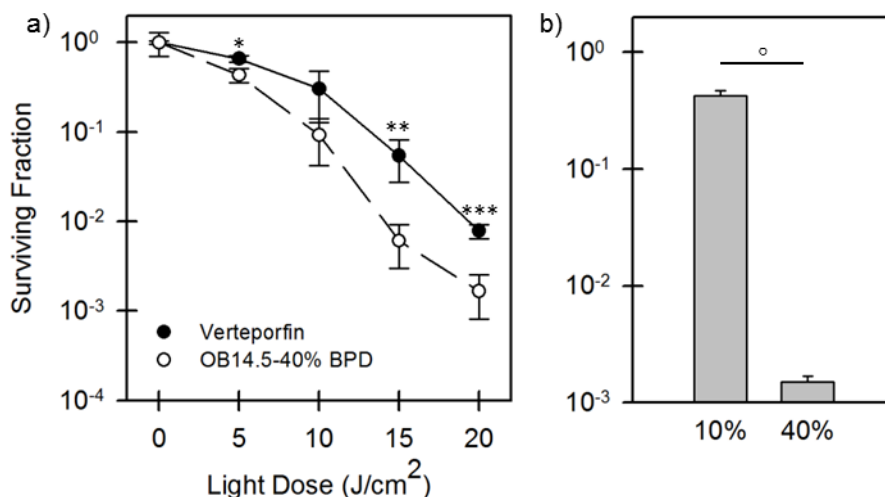
Figure 4-5: OVCAR-5 Surviving Fraction after PDT. (a) OVCAR-5 cells were incubated with 20 ng/mL of BPD-MA as either verteporfin or OB14.5-40% BPD polymersomes for 12 hours. The light dose was varied by modulating the illumination time. The fluence rate was held constant at 40 mW/cm^2. * p = 0.014, ** p = 0.036, *** p = 0.003. (b) OVCAR-5 cells were incubated with 20 ng/mL of BPD-MA for 12 hours as OB14.5-10% BPD or OB14.5-40% BPD. ∘ p = 0.0007. The light dose in (b) was kept constant at 20 J/cm^2 with a fluence rate of 40 mW/cm^2. p-values determined from single factor ANOVA with the level of significance, α = 0.05. Error bars represent standard deviation.

Despite the lower measured singlet oxygen production by OB14.5-40% BPD compared to verteporfin (as shown in Figure 4-3), the polymersomes produced greater phototoxicity than verteporfin at all light doses. This effect could be the result of an increase in cellular uptake of BPD when delivered by polymersomes (see Figure 4-4a). Also, the greater toxicity of polymersome-mediated PDT could be related to high local concentrations of singlet oxygen that are produced by OB14.5-40% BPD. To test the latter hypothesis, we treated OVCAR-5 cells with equal BPD concentration (20 ng/mL) of OB14.5 polymersomes loaded with 10% or 40% BPD in the membrane. Results showed that a lower molar loading of BPD in the polymersome membrane (10% vs. 40%) produced very little phototoxicity even though the total BPD concentration was identical (Figure 4-5b). This suggests that highly localized concentrations of BPD as can be delivered by polymersomes can significantly benefit cytotoxicity, although this is associated with the caveat that high loading can promote inefficiencies in singlet oxygen production, perhaps due to quenching.

4.4.5 *In Vivo* Biodistribution

We investigated the *in vivo* biodistribution of verteporfin and OB14.5-40% BPD polymersomes in nude Athymic female mice first via a semi-quantitative longitudinal imaging study using an NIR imager, and second with a quantitative end-point assay using a spectrofluorometer.

For the longitudinal imaging study, BPD-MA was injected via tail vein at a dose of 1 mg/kg as verteporfin or OB14.5-40% BPD. The fluorescence of BPD-MA was monitored in the 700 channel of the LI-COR Pearl® Impulse Small Animal Imaging System in the tumor (one each on left and right shoulders of the animal), as well as in the upper and lower abdomen, which corresponded to signal from mostly the liver and intestines, respectively. Based on our previous results showing that BPD-MA partitioned into lipophilic environments such as serum proteins (Figure 4-4), we also injected the mice with polymersomes encapsulating PZn_3 to track the polymersomes themselves. PZn_3 is a large and hydrophobic molecule that remains associated with the polymersome membrane for a prolonged length of time compared to BPD. OB14.5-40% BPD/2.5% PZn_3 (dual-labeled) and OB14.5-2.5% PZn_3 (singly-labeled) polymersomes were injected separately to track the separation of photosensitizer from polymersomes and polymersome location, respectively, in the 800 channel of the Pearl®. PZn_3 has previously been used for the *in vivo* tracking of dendritic cells, and an *in vitro* and *in vivo* study of polymersomes localization [32, 34, 35, 39, 40].
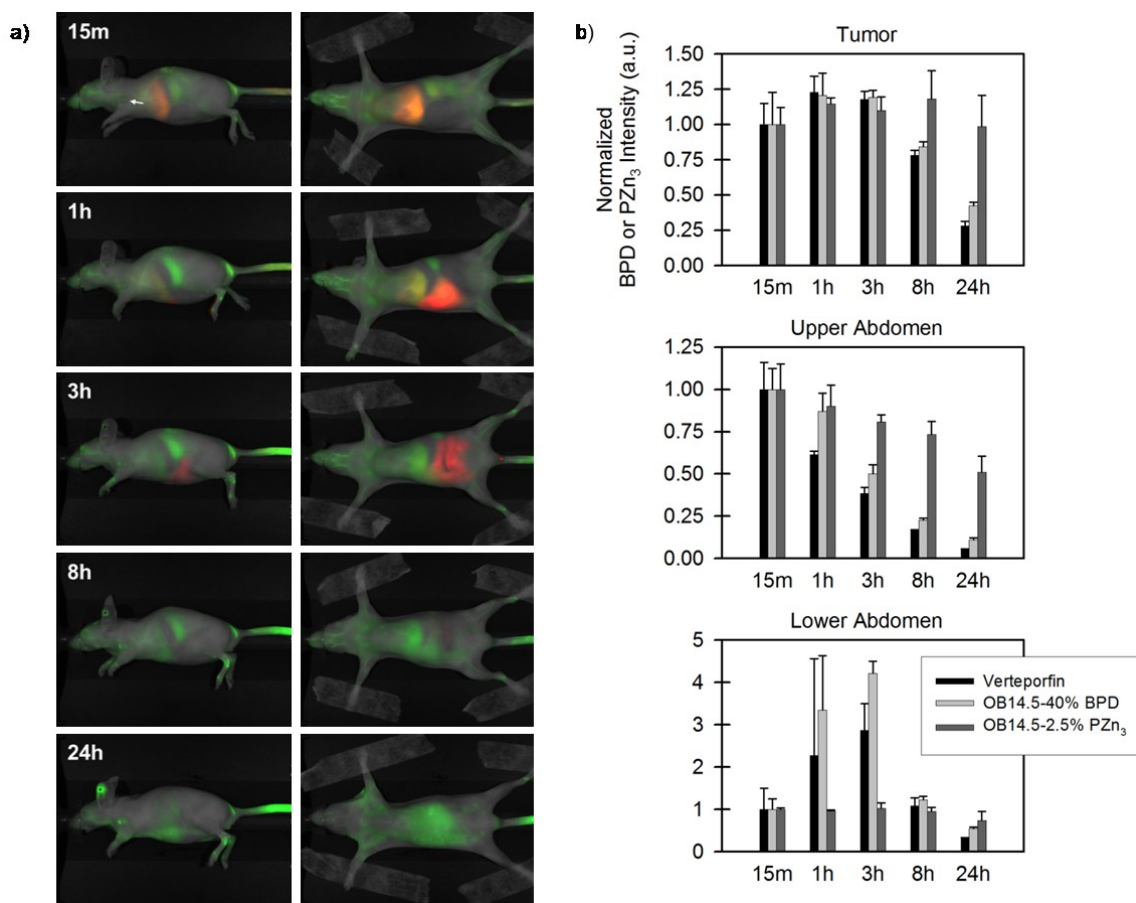
Figure 4-6: Longitudinal imaging of polymersomes formulated as OB14.5-40% BPD and/or OB14.5-2.5% PZn$_3$. (a) Mice received dual-labeled OB14.5-40% BPD/2.5% PZn3 polymersomes. Left column shows the left side of a mouse (arrow points to left tumor) and the right column shows the ventral side of the mouse. Emission has been pseudo-colored red (700 channel for BPD-MA) and green (800 channel for PZn$_3$). (b) In mice that received verteporfin, OB14.5-40% BPD, or OB14.5-2.5% PZn$_3$, ROIs were drawn over the tumors, upper abdomen and lower abdomen to measure the signal intensity per pixel (n = 2 – 3 mice per condition). Error bars indicate standard deviation. Intensity values were normalized within each mouse to the values measured at 15 minutes after drug injection.

Figure 4-6 shows the time-course of drug distribution in a mouse given dual-labeled polymersomes. At early times (15 minutes and 1 hour) after injection, both BPD-MA and the polymersome can be seen in the liver (yellow colocalization in the liver). After 1 hour, BPD-MA started to accumulate in the lower abdomen and was present in large amounts in the intestines (3 hours). After 8 hours, the lower abdomen was cleared of BPD-MA altogether. In animals that received verteporfin, OB14.5-40%, or BPD/2.5% PZn$_3$, we quantified the signal intensity from the left and right tumors, upper abdomen,

and lower abdomen (Figure 4-6b). Based on these results, BPD-MA in verteporfin and OB14.5-40% BPD has a similar biodistribution with the exception of a delayed clearance of OB14.5-40% BPD from the upper abdomen (see 1 h timepoint). In tumors, it appears that BPD begins to be cleared at times after 3 h for both the liposomal and polymersomal formulations. In contrast, the PZn$_3$ signal is very consistently seen in the tumor and lower abdomen, indicating that the polymersomes are staying in these locations. There is moderate clearance from the upper abdomen, but the clearance rate is much slower for the polymersomes than for the BPD.

The imaging study provided a unique insight - that both the photosensitizer and polymersomes were reaching the tumor, and that the polymersomes were present for long times within the mice. Using an *ex vivo* spectrofluorimetric assay, the biodistribution of BPD-MA after liposome vs. polymersome delivery was studied in greater detail for each organ. Mice were injected with verteporfin or OB14.5-40% BPD at a dose of 1 mg/kg. After predefined time points (15 minutes, 3 hours, 8 hours, 16 hours, and 24 hours), blood was collected via cardiac puncture, then tumor, liver, spleen, and intestines were harvested from the euthanized animals. The aforementioned organs were analyzed for BPD-MA content by digesting these organs in a strong base and measuring the fluorescence of BPD-MA in the solubilized tissue (Figure 4-7). OB14.5-40% BPD was more slowly taken up into the tumor than verteporfin as indicated by a significantly lower BPD-MA concentration at 3 h after injection of the polymersomes. Given the extremely similar plasma concentrations of drug for the formulations, it is likely that the delayed tumor uptake of BPD with polymersomes compared to verteporfin is due to the increased size of the polymersomes. Once present in the tumor, the BPD-MA concentration remained fairly equal between the two formulations. In the abdominal organs, the intestines (and to insignificant levels, the liver) were noted to have high BPD-

MA uptake at 15 min after administration of polymersomes, but this cleared to levels equivalent to liposome-delivered BPD at 3 h post-injection. At the longer time points of 16 and 24 h, the intestines, liver, and spleen had a small but significantly increased concentration of BPD-MA after administration of polymersomes compared to that resulting from liposome delivery of BPD. This is consistent with the longer retention of polymersomes in the upper and lower abdomen by in vivo imaging. Enhanced retention in abdominal organs could be related to polymersome interaction with immune cells such as macrophages due to their larger size.
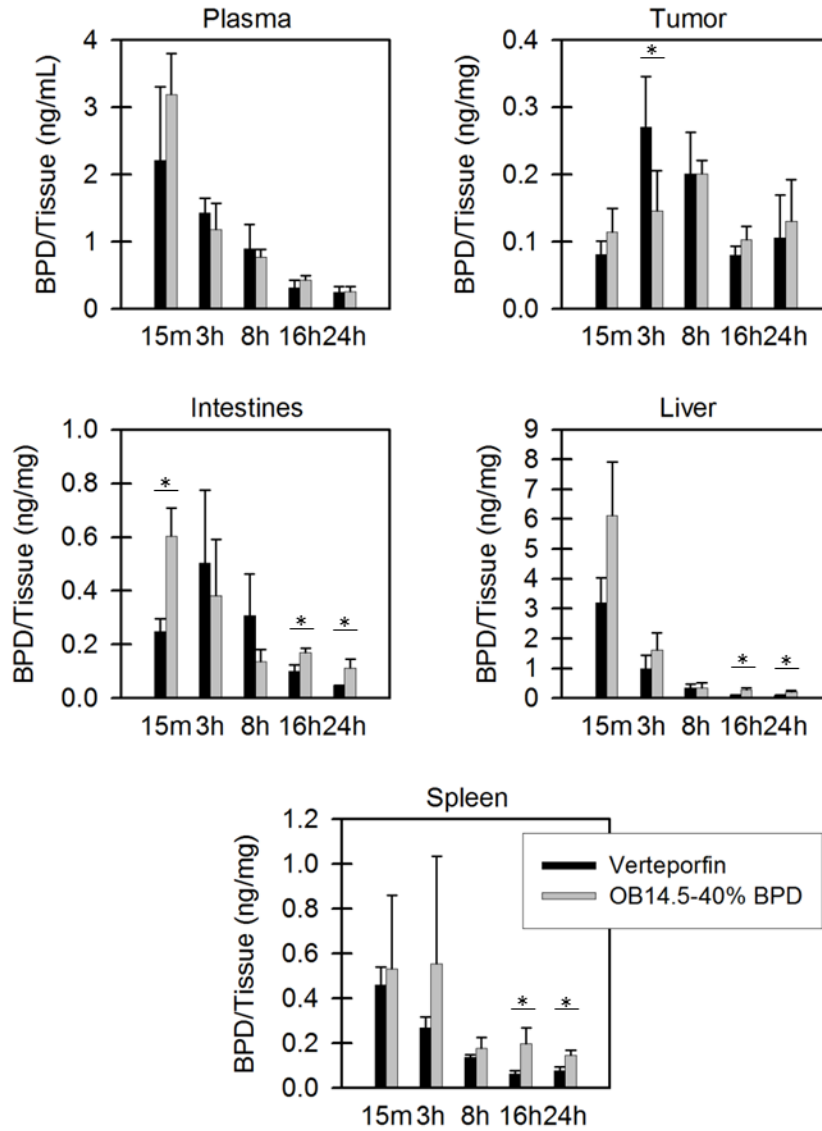
Figure 4-7: Biodistribution of BPD-MA as delivered by verteporfin and OB14.5-40% BPD. At the indicated time points after injection, BPD-MA content was measured in the respective organs spectrophotometrically and calibrated to yield a concentration. Mice were injected with an equivalent dose of 1 mg/kg BPD-MA as verteporfin or OB14.5-40% BPD. * $p < 0.05$ as determined from single factor ANOVA with the level of significance, α = 0.05. Error bars represent standard deviation.

4.4.6 *In Vivo* Response of OVCAR-5 Tumors

Lastly, the effectiveness of PDT mediated by OB14.5-40% BPD polymersomes was tested in OVCAR-5 tumor xenografts. Once tumors reached approximately 50 mm^3, mice were injected with an equivalent dose of 1 mg/kg BPD-MA as either verteporfin or polymersome via tail vein. In oncology studies, BPD-PDT is employed with a 3 h drug incubation to cause tumor cell damage, so we chose a 3 h interval before illuminating the tumors with 690 nm light [41, 42]. Tumors were treated with a fluence rate of 75 mW/cm^2 light for a total light dose of 75 J/cm^2. We monitored tumor growth for 20 days after PDT. Tumor volumes were determined as follows:

$$V = \frac{\pi LW^2}{6} \qquad\qquad \textbf{Equation 1}$$

where L and W are the length and width of the tumor, respectively, and $L > W$. Mice were sacrificed if the tumor volume exceeded 400 mm^3.

The tumors of mice that received either verteporfin or OB14.5-40% BPD, but no light, grew at a similar rate as those that received no light and no drug treatment (Figure 4-8a). Moreover, animals that received light, but no drug (Figure 4-8b plot of "no treatment") also grew at a similar rate to the other controls. In contrast, mice that received PDT (75 J/cm^2 of 690 nm light) of their tumors (Figure 4-8b) showed a reduced tumor growth rate compared to all of the control groups.
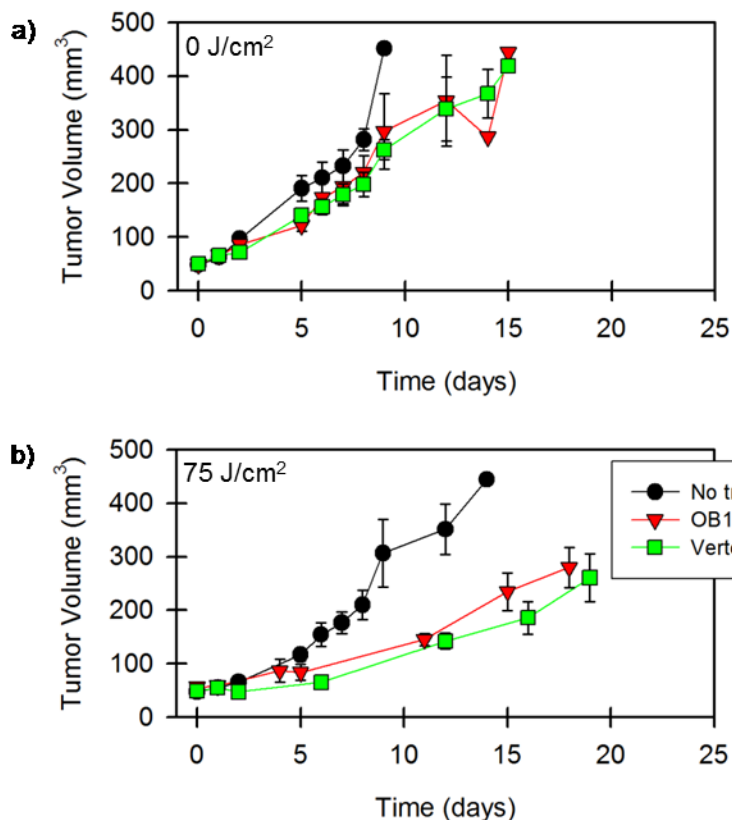
Figure 4-8: PDT response of OVCAR-5 tumors. Nude athymic female mice were treated with saline (no treatment), OB14.5-40% BPD, or verteporfin at a dose of 1 mg/kg BPD. (a) The control groups received no light treatment. Each condition had three mice. (b) The light-treated group received 75 J/cm^2 of light at a fluence rate of 75 mW/cm^2. The no treatment group had three mice, whereas the OB14.5-40% BPD and verteporfin group each had five mice. Error bars are standard error of the mean.

While the tumor response was similar for OB14.5-40% BPD and verteporfin, it should be noted that the concentration of BPD-MA in the tumor is a factor of 2 lower for the polymersomes (see 3 h time point on Figure 4-7). Thus, the OB14.5-40% BPD polymersomes provided equal phototoxicity with a lower dose of BPD than that delivered by verteporfin.

4.5 Conclusion

In summary, the second generation photosensitizer benzoporphyrin derivative monoacid A (BPD-MA) was encapsulated in the hydrophobic membrane of

polymersomes synthesized from the diblock copolymer, OB14.5 (PEO_{14}-PBD_{22}). The efficacy of this photosensitizer formulation was compared to an existing liposomal formulation, verteporfin. OB14.5-40% BPD was more potent at killing OVCAR-5 cells than verteporfin *in vitro* as determined from clonogenic assays. The polymersomes served as a protection against serum binding, thereby increasing the concentration of free BPD that was able to produce phototoxicity. I*n vivo*, OB14.5-40% BPD polymersomes and verteporfin had similar biodistribution profiles. There was a lag in BPD-MA accumulation in the tumor at short times (3 h). Despite having a lower concentration in the tumor at 3 h, the polymersome formulation performed on par with verteporfin in studies of tumor response to PDT.

4.6 Acknowledgements

The results and conclusions presented in this chapter have been adapted from a manuscript submitted to ACS Nano titled, "Nano-polymersomes for Photodynamic Therapy of Ovarian Cancer." The complete author list is as follows: *Nimil Sood,[1] Joann Miller,[2] Shannon M. Gallagher-Colombo,[2] Kevin B. Vargo,[1] Jeff Rawson,[3] Michael J. Therein,[3] Daniel A. Hammer,[1] and Theresa M. Busch[2,*]*

[1] Department of Chemical and Biomolecular Engineering, University of Pennsylvania, 220 S. 33rd St., Philadelphia, PA 19104

[2] Department of Radiation Oncology, Smilow Center for Translational Research, Room 8-126, University of Pennsylvania, 3400 Civic Blvd., Bldg 421, Philadelphia, PA 19104

[3] Department of Chemistry, Duke University, 124 Science Drive, Durham, NC 27708

4.7 References

1.   Gao, F., et al., *Systematic review: photodynamic therapy for unresectable cholangiocarcinoma.* Journal of Hepato-Biliary-Pancreatic Sciences, 2010. **17**(2): p. 125-131.

2.   Hahn, S.M., et al., *Photofrin uptake in the tumor and normal tissues of patients receiving intraperitoneal photodynamic therapy.* Clinical Cancer Research, 2006. **12**(18): p. 5464-5470.

3.   Biel, M.A., *Photodynamic Therapy of Head and Neck Cancers.* Methods in Molecular Biology, 2010. **635**: p. 281-293.

4.   Bozzini, G., et al., *Photodynamic therapy in urology: What can we do now and where are we heading?* Photodiagnosis and Photodynamic Therapy, 2012. **9**(3): p. 261-273.

5.   Friedberg, J.S., et al., *Radical Pleurectomy and Intraoperative Photodynamic Therapy for Malignant Pleural Mesothelioma.* Annals of Thoracic Surgery, 2012. **93**(5): p. 1658-1667.

6.   Shishkova, N., O. Kuznetsova, and T. Berezov, *Photodynamic Therapy for Gynecological Diseases and Breast Cancer.* Cancer Biology & Medicine, 2012. **9**(1): p. 9-17.

7.   Friedberg, J.S., et al., *Photodynamic Therapy and the Evolution of a Lung-Sparing Surgical Treatment for Mesothelioma.* Annals of Thoracic Surgery, 2011. **91**(6): p. 1738-1746.

8.   Gomer, C.J., et al., *Photodynamic therapy: Combined modality approaches targeting the tumor microenvironment.* Lasers in Surgery and Medicine, 2006. **38**(5): p. 516-521.

9.	Verma, S., et al., *Strategies for enhanced photodynamic therapy effects.* Photochemistry and Photobiology, 2007. **83**(5): p. 996-1005.

10.	Quon, H., et al., *Photodynamic therapy in the management of pre-malignant head and neck mucosal dysplasia and microinvasive carcinoma.* Photodiagnosis and Photodynamic Therapy, 2011. **8**(2): p. 75-85.

11.	Dolmans, D.E.J.G.J., D. Fukumura, and R.K. Jain, *Photodynamic therapy for cancer.* Nature Reviews Cancer, 2003. **3**(5): p. 380-387.

12.	Dougherty, T.J., et al., *Photodynamic therapy.* Journal of the National Cancer Institute, 1998. **90**: p. 889-905.

13.	Peng, Q., J. Moan, and J.M. Nesland, *Correlation of subcellular and intratumoral photosensitizer localization with ultrastructural features after photodynamic therapy.* Ultrastructural Pathology, 1996. **20**(2): p. 109-129.

14.	Busch, T.M., *Local physiological changes during photodynamic therapy.* Lasers in Surgery and Medicine, 2006. **38**(5): p. 494-499.

15.	Maas, A.L., et al., *Tumor Vascular Microenvironment Determines Responsiveness to Photodynamic Therapy.* Cancer Research, 2012. **72**(8): p. 2079-2088.

16.	Castano, A.P., P. Mroz, and M.R. Hamblin, *Photodynamic therapy and anti-tumour immunity.* Nature reviews. Cancer, 2006. **6**: p. 535-45.

17.	Sadasivam, M., et al., *Self-assembled liposomal nanoparticles in photodynamic therapy.* Eur J Nanomed, 2013. **5**(3).

18.	Bechet, D., et al., *Photodynamic therapy of malignant brain tumours: A complementary approach to conventional therapies.* Cancer Treatment Reviews, 2014. **40**(2): p. 229-241.

19. Mir, Y., S.A. Elrington, and T. Hasan, *A new nanoconstruct for epidermal growth factor receptor-targeted photo-immunotherapy of ovarian cancer.* Nanomedicine-Nanotechnology Biology and Medicine, 2013. **9**(7): p. 1114-1122.

20. Khdair, A., et al., *Nanoparticle-mediated combination chemotherapy and photodynamic therapy overcomes tumor drug resistance in vitro.* European Journal of Pharmaceutics and Biopharmaceutics, 2009. **71**(2): p. 214-222.

21. Master, A., M. Livingston, and A. Sen Gupta, *Photodynamic nanomedicine in the treatment of solid tumors: Perspectives and challenges.* Journal of Controlled Release, 2013. **168**(1): p. 88-102.

22. Ding, H.Y., et al., *Nanoscopic micelle delivery improves the photophysical properties and efficacy of photodynamic therapy of protoporphyrin IX.* Journal of Controlled Release, 2011. **151**(3): p. 271-277.

23. de Paula, C.S., et al., *Chloroaluminium phthalocyanine polymeric nanoparticles as photosensitisers: Photophysical and physicochemical characterisation, release and phototoxicity in vitro.* European Journal of Pharmaceutical Sciences, 2013. **49**(3): p. 371-381.

24. Aveline, B., T. Hasan, and R.W. Redmond, *Photophysical and photosensitizing properties of benzoporphyrin derivative monoacid ring A (BPD-MA).* Photochemistry and photobiology, 1994. **59**: p. 328-35.

25. Aveline, B.M., T. Hasan, and R.W. Redmond, *The effects of aggregation, protein binding and cellular incorporation on the photophysical properties of benzoporphyrin derivative monoacid ring A (BPDMA).* Journal of photochemistry and photobiology. B, Biology, 1995. **30**: p. 161-9.

26. FDA. *NME Drug and New Biologic Approvals in 2000*. 2011; Available from: http://www.fda.gov/drugs/developmentapprovalprocess/howdrugsaredevelopedandapproved/drugandbiologicapprovalreports/ucm081685.htm.

27. Blumenkranz, M.S., et al., *Photodynamic therapy of subfoveal choroidal neovascularization in age-related macular degeneration with verteporfin - Two-year results of 2 randomized clinical trials - TAP report 2.* Archives of Ophthalmology, 2001. **119**(2): p. 198-207.

28. Bressler, N.M. and D. Treatment Age Related Macular, *Photodynamic therapy of subfoveal choroidal neovascularization in age-related macular degeneration with verteporfin - One-year results of 2 randomized clinical trials - TAP report 1.* Archives of Ophthalmology, 1999. **117**(10): p. 1329-1345.

29. Rizvi, I., et al., *PDT Dose Parameters Impact Tumoricidal Durability and Cell Death Pathways in a 3D Ovarian Cancer Model.* Photochemistry and Photobiology, 2013. **89**(4): p. 942-952.

30. Discher, B.M., *Polymersomes: Tough Vesicles Made from Diblock Copolymers.* Science, 1999. **284**(5417): p. 1143-1146.

31. Discher, D.E. and A. Eisenberg, *Polymer vesicles.* Science, 2002. **297**: p. 967-973.

32. Ghoroghchian, P.P., et al., *Near-infrared-emissive polymersomes: Self-assembled soft matter for in vivo optical imaging.* Proceedings of the National Academy of Sciences of the United States of America, 2005. **102**(8): p. 2922-2927.

33. Ghoroghchian, P.P., et al., *Bioresorbable Vesicles Formed through Spontaneous Self-Assembly of Amphiphilic Poly(ethylene oxide)-block-polycaprolactone.* Macromolecules, 2006. **39**: p. 1673-1675.

34. Levine, D.H., et al., *Polymersomes: a new multi-functional tool for cancer diagnosis and therapy.* Methods (San Diego, Calif.), 2008. **46**: p. 25-32.

35. Christian, N.a., et al., *In vivo dendritic cell tracking using fluorescence lifetime imaging and near-infrared-emissive polymersomes.* Molecular imaging and

biology : MIB : the official publication of the Academy of Molecular Imaging, 2009. **11**: p. 167-77.

36.   Duncan, T.V., et al., *Exceptional near-infrared fluorescence quantum yields and excited-state absorptivity of highly conjugated porphyrin arrays.* Journal of the American Chemical Society, 2006. **128**: p. 9000-1.

37.   Anraku, Y., et al., *Size-controlled long-circulating PICsome as a ruler to measure critical cut-off disposition size into normal and tumor tissues.* Chemical Communications, 2011. **47**(21): p. 6054-6056.

38.   Hasan, T., A.C.E. Moore, and B. Ortel, *Photodynamic Therapy of Cancer*, in *Holland-Frei Cancer Medicine*, R.J. Bast, D. Kufe, and R. Pollack, Editors. 2000.

39.   Sood, N., et al., *Biodegradable Polymersomes for the Delivery of Gemcitabine to Panc-1 Cells.* Journal of Pharmaceutics, 2013. **2013**: p. 10.

40.   Christian, N.a., et al., *Tat-functionalized near-infrared emissive polymersomes for dendritic cell labeling.* Bioconjugate chemistry, 2007. **18**: p. 31-40.

41.   Chen, B., et al., *Combining vascular and cellular targeting regimens enhances the efficacy of photodynamic therapy.* International Journal of Radiation Oncology Biology Physics, 2005. **61**(4): p. 1216-1226.

42.   Richter, A.M., et al., *Liposomal Delivery of a Photosensitizer, Benzoporphryin Derivative Monoacid Ring A (BPD), to Tumor Tissue in a Mouse Tumor Model.* Photochemistry and Photobiology, 1993. **57**(6): p. 1000-1006.

5 A Hydrodynamic Model of the Sized-Based Separation of Polymersomes Using a Deterministic Lateral Displacement Microfluidic Device

5.1 Summary

We developed a hydrodynamic, forced-based computational model to understand the fractionation of polymersomes in a DLD microfluidic device. We found that the key parameter in determining the separation between two particles is the strength of the attraction between the cylindrical post and spherical polymersome. We developed a microfluidic DLD device synthesized from photolithographic techniques to experimentally separate polymersomes of known sizes. Using this model, we can correctly predict the fractionation of two polymersomes of different sizes (46 and 58 µm) in a DLD device.

5.2 Introduction

Particle suspensions have traditionally been fractionated by size using chromatographic techniques. In this separation technology [1], porous beads are packed in a column and the particle suspension is driven through the stationary phase via a pressure gradient. Particles that are smaller than the pore size can travel through the beads via the tortuous pores, whereas larger particles travel through the void space created from the bead packing. The resulting fractionation occurs because of the size-dependent path length taken by particles. A disadvantage to this method of fractionation is the "zone broadening" effect which stems from the fact that two particles of the same size may take two different paths: one longer and one shorter.

The development of microfluidic devices for particle separation and fractionation is an interesting approach that combines hydrodynamics with chromatography. Deterministic lateral displacement (DLD) devices have been used to separate a wide range of particle sizes particles with submicron resolution [2, 3]. DLD devices utilize laminar flow through a periodic array of micron-sized obstacles that are rotated by a small angle with respect to the direction of flow. Particles that are larger than a critical size are "bumped" by the obstacles and are unable to cross-over into different lanes, whereas particles smaller than the critical size "zig-zag" through the device separating themselves from the larger particles.

Theoretical approaches have been developed to understand the relationship between device geometry and particle separation [4-6]. In these approaches, particles follow streamlines until they interact with a post. Larger particles are unable to access streamlines that are close to the post due to steric hindrance effects and as such are

bumped by the posts. Smaller particles can travel along streamlines closer to the posts and can "zig-zag" between posts and migrate down the device at a different trajectory from larger particles. These approaches, however, do not take into account the vast majority of forces exerted on the particle by the fluid and posts and as such are unable to capture the physical motion of particle trajectories.

Frechette and Drazer used a Stokesian Dynamics approach to understand particle trajectories in DLD devices [7]. Their model looked at the dynamics of a non-Brownian sphere suspended in a stationary fluid subject to a constant external force and a short range repulsive interaction. Simulations showed that particles subjected to varying forcing angles separated themselves based on size. The key difference between the simulations performed by Frechette and Drazer and the work done here is the inclusion of non-constant forces that are position dependent. Here we include non-constant hydrodynamic forces, torques, and van der Waals and steric repulsive forces that are coupled together via the grand mobility matrix.

5.3 Materials and Methods

5.3.1 Materials

Poly(ethylene oxide)-poly(butadiene), PEO_{30}-b-PBD_{46} (OB29, MW = 3800 g/mol) was purchased from Polymer Source (Montreal, Canada). Bovine serum albumin (BSA) and Pluronic F-127 were purchased from Sigma. Sylgard 184 silicone elastomer base and curing agent were purchased from Dow-Corning. PBS was purchased from Fisher.

5.3.2 Microfluidic Vesicle Preparation

Micron-sized vesicles were prepared via a double emulsion technique using a glass capillary system as described previously [8-11]. The inner aqueous phase consisted of a solution of 290 mOsm sucrose. The middle organic phase consisted of a solution of 1 mg/mL OB29 in a mixture of chloroform and toluene (28:72 v/v). The outer phase consisted of 290 mOsm phosphate buffered saline (PBS) containing 1wt% BSA. The three solutions were cofocused into a single immiscible stream to generate double emulsions. These emulsions were collected in 2 mL of PBS in a 20 mL scintillation vial. The vials were loosely capped and placed on a gentle rocker for 1-2 weeks to allow for the organic layer to evaporate. The inner flow rate was maintained at 1.5 mL/hr, the middle flow rate at 7 mL/hr, and the outer flow rate was varied from 20-50 mL/hr to generate vesicles of various sizes.

5.3.3 Microfluidic Mask Design

The photomask was designed using AutoSketch®. The cylindrical posts are 100 μm in diameter with an edge-to-edge spacing of 60 μm and grid rotation of 8º.

5.3.4 Microfluidic Chamber Preparation

The deterministic lateral displacement device was fabricated by replica molding on a patterned silicon wafer as the master and polydimethylsiloxane (PDMS) as the polymer. The master was fabricated by spinning a layer of negative photoresist (KMPR 1050,MicroChem Corp., Brookline, MA) with a thickness of 88 μm onto a smooth silicon wafer, followed by a ramped soft bake period (65ºC to 115ºC at a rate of 15ºC every two minutes), and a continuous soft bake period at 115ºC for 15 minutes. The KMPR-coated wafers were exposed to UV light at a dose of 1520 mJ/cm^2 using a contact mask aligner,

and post baked for seven minutes at 105ºC. The exposed wafer was developed with SU-8 developer solution for 10 minutes, followed by an isopropanol rinse and drying. The device was fabricated by pouring PDMS (PDMS:curing agent 10:1 by weight) over the master and curing the elastomer for 12 hours at 65ºC. The device was cut out and separated from the master. Holes were punched out for the inlets and outlets with a flat-tip stainless steel 20G needle. The PDMS device was plasma bonded to a glass cover slip.

5.3.5 Microfluidic Chamber Operation

Polymersome and PBS were loaded into one 3 cc and two 10 cc syringes, respectively. Polymersomes were introduced into the device via a syringe pump operating at a flow rate of 100 μL/hr. PBS was introduced into the left and right inlet channels using a second syringe pump operating at a flow rate of 1.5 mL/hr. These flow rates ensured laminarity in the microfluidic device.

5.3.6 Determination of Forces

We calculated the external forces exerted on the polymersomes by the fluid and cylindrical posts. Here we specifically considered the shear force exerted on the polymersome by the fluid, the torque exerted on the polymersome by the fluid due to the cylindrical posts, the van der Waals force between the polymersome and the posts, and the steric stabilization between the polymersome and posts. Our computational model assumed a two dimensional Stoke's flow in the microfluidic device with negligible diffusion effects ($Pe \gg 1$). Additionally, we ignored top and bottom edge effects in the calculations of particle trajectories. With these assumptions, we applied a streamline solution to determine the fluid velocity everywhere in the device.

Table 5-1: Definition of parameters in the computational model

Parameter	Definition
a	Polymersome radius, μm
μ	Water viscosity, $N \cdot s \cdot \mu m^{-2}$
F_i	Shear force on polymersome ($i = x, y$), N
v_i^{fluid}	Fluid velocity ($i = x, y$), $\mu \cdot s^{-1}$
U	Uniform fluid velocity, $\mu \cdot s^{-1}$
R	Post radius, μm
dG	Differential torque from post, $N \cdot \mu m$
$\tau_{r\theta}$	Viscous stress, $N \cdot \mu m^{-2}$
H	Hamaker constant, J
$2h$	Polymersome to post center to center distance, μm
γ	Compressibility of PEG brush, N
s	Polymersome to post edge to edge distance, μm
τ	Thickness of PEG brush, μm

Given the fluid velocity, the shear force on the polymersome was determined by invoking Stoke's Law,

$$F_{x,y} = 6\pi\mu a v_{x,y}^{fluid} \qquad\qquad \text{Equation 5.1}$$

The expressions for the fluid velocities are given in the Appendix. In addition to the shear exerted on the polymersome by the fluid, the fluid flow also introduced a torque on the particles because the fluid is traveling at a slower velocity near the posts. We can once again take advantage of the streamline solution to the fluid flow field and determine the viscous stress on the polymersome. The expression for the differential torque on a polymersome due to one post is,

$$dG = \tau_{r\theta} \cdot a \sin \phi \, dS$$ **Equation 5.2**

We can then integrate all of the differential torque components from the posts and add them together to obtain the final expression for the torque on the polymersome. The detailed calculations are presented in the Appendix.

The two nonspecific interactions considered in this model were van der Waals and steric stabilization interactions. We approximated the interaction between the spherical polymersome and cylindrical post as a sphere-sphere interaction, where the expression for the van der Waals force has been determined by Parsegian [12],

$$F_{vdW} = -\frac{32H}{3} \frac{a^3 R^3 2h}{(4h^2 - (a+R)^2)^2 (4h^2 - (a-R)^2)^2}$$ **Equation 5.3**

The steric stabilization force is a well-known force in colloidal science [13]. It can be used to describe interactions between polymer-coated particles, such as cell-cell interactions in biology, or in our case, polymersome-post interactions. When two polymer-coated objects come close together, the polymer brushes on the surface compress and exclude the solvent. The resulting repulsive potential as described by Bell, Dembo, and Bongrand [14] can be represented as,

$$\Gamma(s) = \frac{\gamma}{s} e^{-s/\tau}$$ **Equation 5.4**

The repulsive force per unit area is simply the negative gradient of the potential with respect to separation distance. Invoking the Langbein approximation to estimate the interaction area between the polymersome and the post, the total repulsive force due to one post is,

$$F_r = 2\pi R\gamma s \left(\frac{1}{s\tau} + \frac{1}{s^2}\right) e^{-s/\tau} \qquad \text{Equation 5.5}$$

5.3.7 Particle Tracking

The external forces (shear, torque, van der Waals, repulsion) as described in the previous section are functions of the position of the polymersome within the deterministic lateral displacement grid. Once these external forces are calculated for the interaction between the polymersome and each post, we sum over all of the posts to calculate the net external forces. The polymersome trajectory can be calculated using the hydrodynamic mobility function. A linear relationship describes the velocity of the particle to the external forces,

$$(\mathcal{F}) = -\mu(\bar{\bar{\mathcal{R}}})(\mathcal{U}) \qquad \text{Equation 5.6}$$

$$(\mathcal{U}) = -\frac{1}{\mu}(\bar{\bar{\mathcal{R}}})^{-1}(\mathcal{F}) \qquad \text{Equation 5.7}$$

The mobility matrix, $(\bar{\bar{\mathcal{M}}})$, is the inverse of the resistance matrix, $(\bar{\bar{\mathcal{R}}})$, and relates the applied external forces to the polymersome linear and angular velocity. The coefficients of $(\bar{\bar{\mathcal{R}}})$ are given in the Appendix and are described in detail by Brenner [15]. Brenner suggested that in the absence of a center of hydrodynamic stress, the

hydrodynamic resistance of a particle could be expressed in terms of three second-rank tensors, termed the Translation Tensor, the Rotational Tensor, and the Coupling Tensor [15]. These three tensors comprise the resistance matrix. Equation 5.7 implies that the inertial forces have been neglected, which is true in our case since the polymersomes have negligible mass, and that the fluid responds instantly to the changes in particle motion.

Polymersome trajectories are calculated as follows. At every time step, the position of the polymersome is known within the grid. Based on the position we can calculate all of the forces exerted on the polymersome. As detailed in the Appendix, the Coupling Tensor is proportional to $1/h^4$, and for this reason we calculate the resistance matrix for the polymersome-post pair that has the shortest center-to-center distance. Once $\left(\bar{\bar{\mathcal{R}}}\right)$ and $\left(\bar{\mathcal{F}}\right)$ are known, Equation 5.7 can be solved for the particle linear and angular velocity. The polymersome position is updated based on the linear velocity, and the trajectory calculation is repeated at the next time step. The schematic of the geometry in the computational model is shown in Figure 5-1.
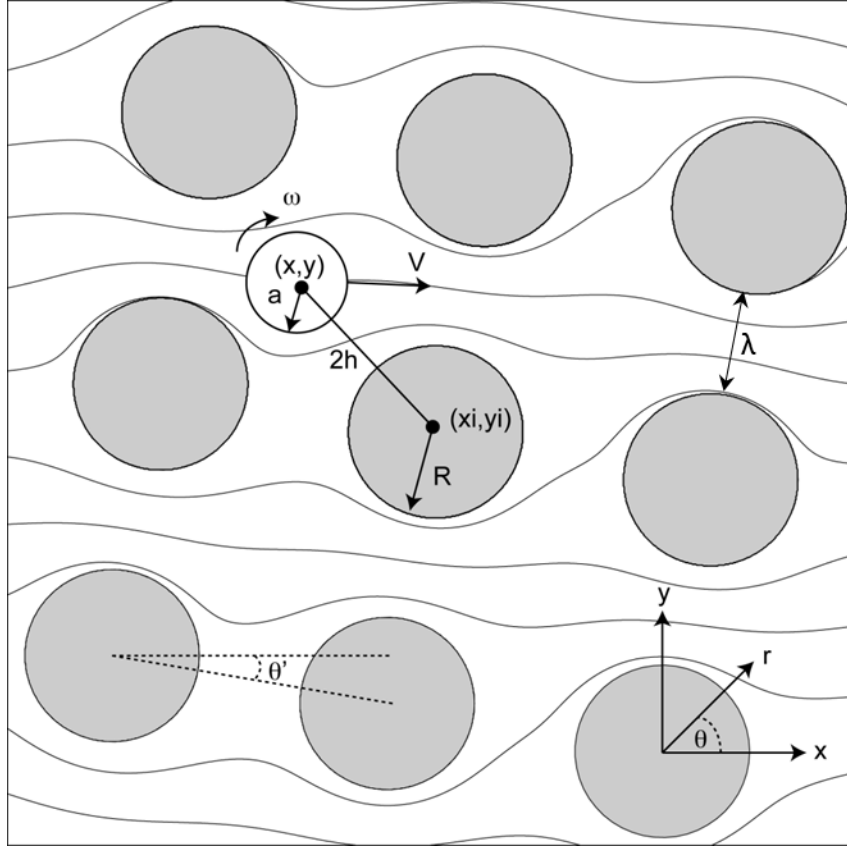
Figure 5-1: Top-view geometry of computational model. A polymersome of radius a interacts with a periodic array of cylindrical posts of radius R. The array is rotated by angle θ' with post edge-to-edge distance λ. The polymersome moves with linear velocity $\bar{V}$ and angular velocity $\bar{\omega}$.

5.4 Results

5.4.1 Two-Body Simulation: Polymersome and Post

We first studied the simplest case of a polymersome interacting with a single post. We use this example to illustrate the importance of the Hamaker constant (H) and polymer chain compressibility (γ) in the model. The interplay between attraction and repulsion is important as it will dictate the particle trajectory and ultimately the separation of the polymersome within the DLD grid. We began by placing the particle far away from the post and introducing a fluid flow in the positive x-direction. Depending on the y-position of the polymersome relative to the post, the polymersome will either clear the post completely following its unperturbed hydrodynamic trajectory, or the will come into

88

close proximity with the post and experience a combination of attraction and repulsion perturbing its hydrodynamic trajectory. We can derive an expression for the critical y-position where the initial incident y-position is equal to the final y-position after encountering the post,

$$y_{Hyd} = a + R_p - \frac{R_p^2}{a + R_p} \qquad \textbf{Equation 5.8}$$

In the case where the particle's trajectory is unperturbed by the post, $y_{in} \geq y_{Hyd}$ and the final y-position is equal to the initial position, $y_{out} = y_{in}$. In the case where the polymersome can feel the post's presence, $y_{in} < y_{Hyd}$ and $y_{out} = y_{Hyd}$. Values of the Hamaker constant and polymer chain compressibility affect y_{out} in the latter case when the polymersome can "feel" the post.
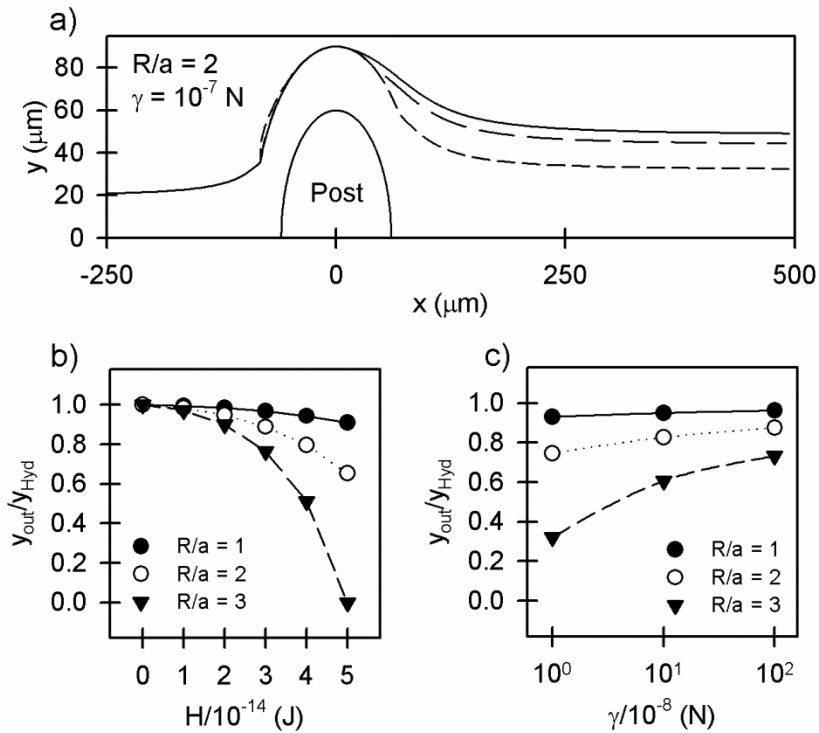
Figure 5-2: Single Polymersome-Post Interaction. a) Representative polymersome trajectory (motion of centers) with $R/a = 2$ for fixed $\gamma = 10^{-7}N$. Values of the Hamaker constant are $1 \times 10^{-14} J$ (solid line), $3 \times 10^{-14} J$ (long dash), and $5 \times 10^{-14} J$ (short dash). b) Deviation from hydrodynamic trajectories as a function of varying Hamaker constant. $\gamma = 10^{-7}N$. c) Deviation from hydrodynamic trajectories as a function of varying and polymer chain compressibility. $H = 3.7 \times 10^{-14}J$.

Figure 5-2 illustrates the effects of varying the Hamaker constant and polymer chain compressibility on polymersome trajectory of different post to polymersome size (R/a) ratios. Figure 5-2a shows a representative trajectory of a polymersome at $R/a = 2$. We see that increasing the Hamaker constant causes the polymersome to have a greater contact time with the post and have a lower y_{out}. We can represent deviations from the unperturbed hydrodynamic trajectory by normalizing y_{out} with y_{Hyd}, where a ratio of one implies a completely hydrodynamic interaction and values less than one indicate the relative strength of non-hydrodynamic interactions (*i.e.* attraction and repulsion). Figure 5-2b and Figure 5-2c show the deviations from the unperturbed hydrodynamic trajectory as a function of varying the Hamaker constant and polymer chain compressibility. For all

size ratios, increasing the attraction increased the contact time between the polymersome and post, whereas increasing the repulsion decreased the contact time. The polymersome trajectory is more sensitive to variations in the Hamaker constant than variations in the polymer chain compressibility, and smaller polymersomes are even more sensitive to this change. For the case of $R/a = 2$, increasing H by a factor of five increased the perturbation from the hydrodynamic trajectory by 30%, whereas increasing γ by a factor of 100 reduced the perturbation by 14%. We also found that a Hamaker constant of $5 \times 10^{-14} J$ imposed a very strong attraction between the polymersome and the post for $R/a = 3$ such that the polymersome trajectory wrapped around the post. This result is physically unattainable in the experimental system and helped establish upper limits for values of the Hamaker constant.

Since the trajectories are not very sensitive to changes in the polymer chain compressibility, we calculated the attractive and repulsive forces felt by the polymersome due to a single post for varying Hamaker constants at a constant γ (Figure 5-3). Figure 5-3a and Figure 5-3b show the attractive and repulsive force, respectively, during the polymersome-post contact. Both forces are zero before and after the contact period. Figure 5-3c and Figure 5-3d show the maximum force felt by the polymersomes, which occurred at initial point of contact between the polymersome and post. Interestingly, we found that the repulsive force depends exponentially on H. By monotonically increasing the Hamaker constant, we are exponentially increasing the repulsion experienced by the polymersome.
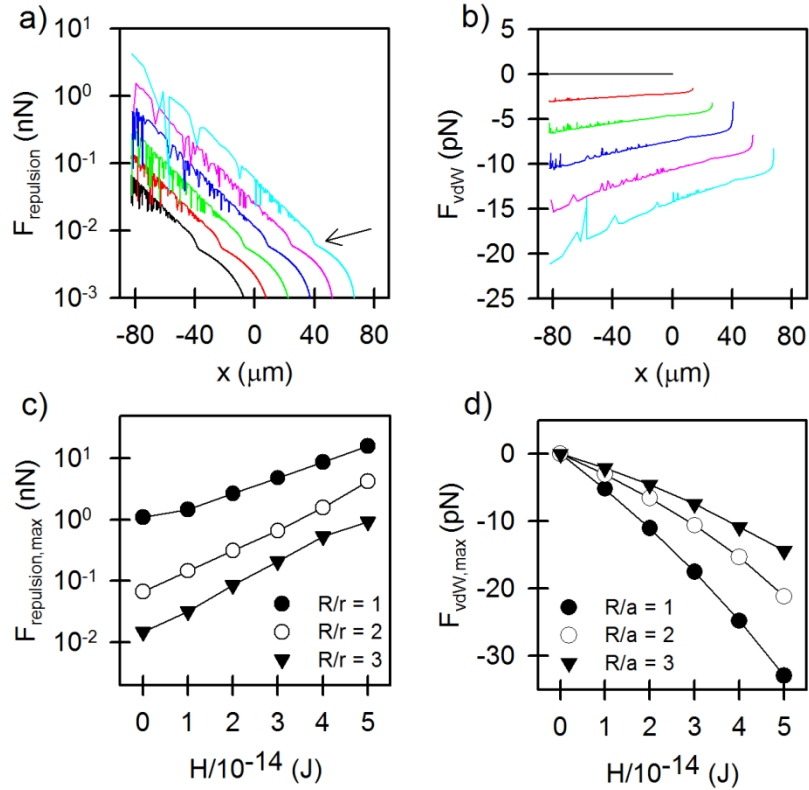
Figure 5-3: Attractive and repulsive forces during interaction. a) Repulsive force and b) attractive force felt by the polymersome for $R/a = 2$, $\gamma = 10^{-7} N$, and $H = 0\,J$ (black), $1 \times 10^{-14}\,J$ (red), $2 \times 10^{-14}\,J$ (green), $3 \times 10^{-14}\,J$ (blue), $4 \times 10^{-14}\,J$ (pink), $5 \times 10^{-14}\,J$ (cyan). The arrow in (a) shows a dip in the forces and is indicative of the point where the polymersome breaks contact with the post. (c) Maximum repulsive force. (d) Maximum attractive force. The force vectors point radially outward, starting at the post center and ending at the polymersome center.

5.4.2 Determination of Computational Grid Size

The forces exerted on the polymersomes are a numerical sum of individual post contributions. While we can generate a post array of an arbitrary size and rotation, it is unnecessary to include force contributions from all posts. The hydrodynamic, repulsive, and attractive forces and the hydrodynamic torque are inverse power law functions of h. As a result, posts that are far away from the polymersome will have negligible contributions to the net calculated force. Figure 5-4 shows the cumulative sum of the non-dimensional forces and torque as a function of the number of nearest posts that are included in the summation.
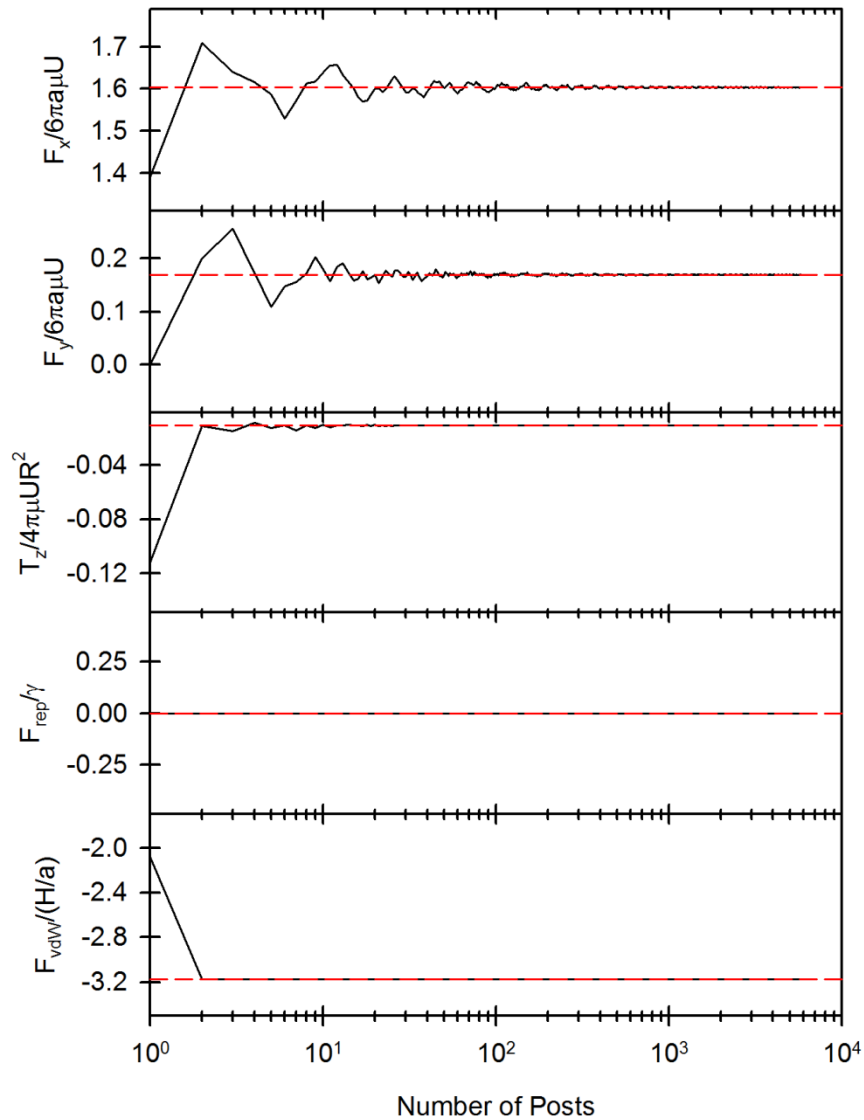
Figure 5-4: Cumulative sum of non-dimensional forces and torque on polymersome. A polymersome (a = 25 μm) was placed in the center of an array of posts with R = 50 μm, λ = 60 μm, θ = 8°. The calculated forces and torque are cumulative sums from post contributions, starting with the nearest post and working radially outward. The red dash represents the "equilibrium" value, which is the cumulative sum from all posts.

As can be seen from Figure 5-4, the equilibrium force or torque value is reached after summation of a finite number of posts. The grid used to calculate the forces and torque contained a total of 7177 posts. The oscillatory behavior in the hydrodynamic forces (F_x and F_y) are severely damped after summing over 100 nearest posts, indicating that (to a good approximation) the equilibrium value has been reached. The hydrodynamic torque

requires even fewer nearest posts (10) to reach equilibrium. The repulsive force is shown to be zero for all post numbers because the polymersome is not in physical contact with the post. This behavior suggests that the repulsive force contribution is a very short range interaction, and only comes from the single nearest post when the polymersome is on the order of τ μm away from the post. Similarly, the attractive force is also a short range interaction, with the polymersome feeling the presence of the nearest two posts. We can conclude from this study that it is unnecessary to include force and torque contributions from all posts within a microfluidic device. The power of this technique implies that one can study the separation of polymersomes within an extremely large grid size simply by calculating the force contributions from the nearest n neighbors.

5.4.3 Experimental Results

The microfluidic device contained three sections: inlet section, fractionation section, and collection section (Figure 5-5). The inlet section consisted of three inlets. The left and right inlets maintained the laminar flow throughout the device, while the center inlet introduced the polymersomes into the device. The fractionation section contained an array of cylindrical posts 100 μm in diameter with an edge-to-edge post spacing of 60 μm and grid rotation of 8°. The size-based separation of polymersomes occurred in this section. The collection section consisted of five outlets. The separated polymersomes exited the device via the outlets.
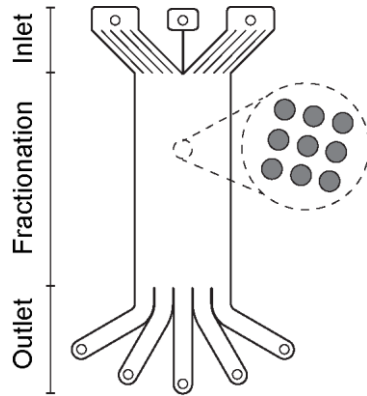
94

Figure 5-5: Microfluidic device schematic. The device contains three distinct regions: inlet, fractionation, and outlet. The polymersomes were introduced into the device through the center inlet channel. The left and right inlet channels helped maintain the fluid laminarity throughout the rest of the device. The fractionation channel contained an array of cylindrical posts with an edge-to-edge distance of 60 μm and post diameter of 100 μm. The overall grid rotation was 8º. The outlet channels were used to collect fractionated polymersomes. It should be noted that the separation occurred in the left half of the device due to the grid rotation.

Based on the grid rotation, the separation occurred in the left half of the device. Two

sizes of polymersomes (46 and 58 μm) were separately introduced into the microfluidic

device and the vesicle trajectories are shown in Figure 5-6. The 58 μm polymersomes

followed the 8º path mapped out by the grid rotation and did not deviate from this path

(Figure 5-6B). The 46 μm polymersomes were seen to deviate from the 8º path and

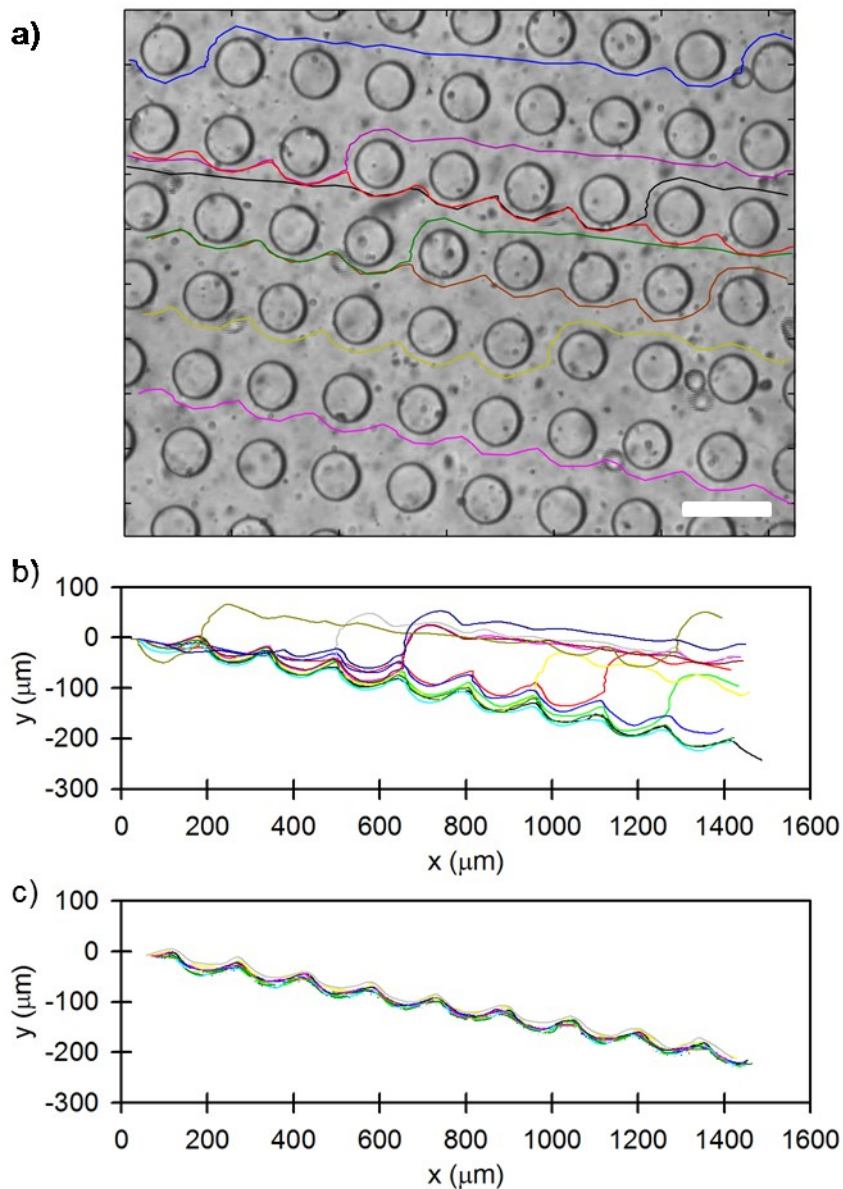cross over into different lanes (Figure 5-6A).

Figure 5-6: Polymersome trajectories in a 400 µm x 1600 µm region in the fractionation zone of the microfluidic device. a) Trajectories of 46 µm polymersomes. Scale bar = 200 µm. b) Corrected trajectories of 46 µm polymersomes, adjusted to start at the same point. c) Corrected trajectories of 58 µm polymersomes, adjusted to start at the same point.

We calculated the average migration angle of the polymersomes within this region and found that there is a 4° separation between the 46 and 58 µm polymersomes (Figure 5-7). This translated to the polymersomes being separated and collected in different collection lanes.
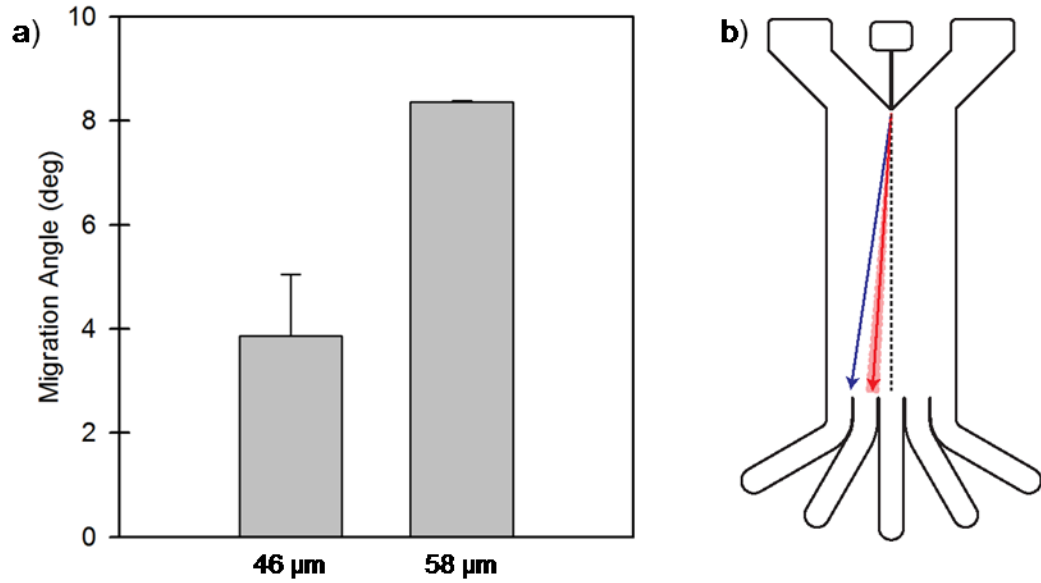
96

Figure 5-7: Polymersome trajectories within microfluidic device. a) Average migration angle of the two polymersomes as determined from experiment. Error bars indicate standard error or the mean. N = 12 for 46 µm polymersomes and N = 11 for 58 µm polymersomes. b) Visualization of the endpoint of migration within the device based on the average migration angle. The shaded region indicates the range of migration as determined from the standard error.

Using the Hamaker constant and polymer brush compressibility parameters established previously, we can use the model to predict the separation of 46 and 58 µm polymersomes (Figure 5-8).
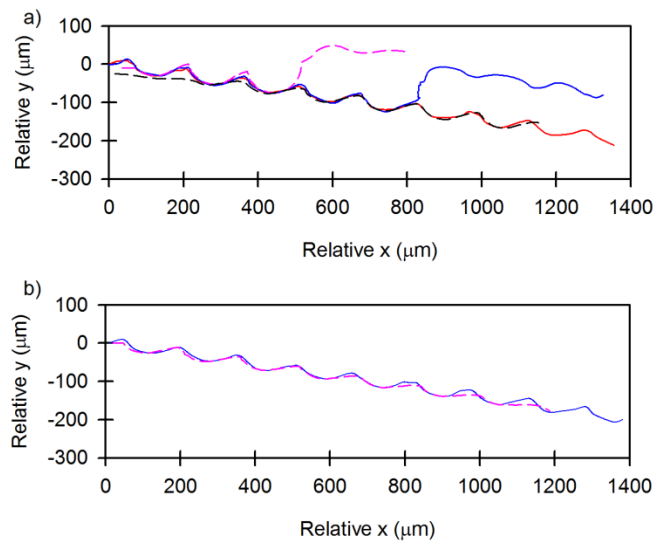

Figure 5-8: Predicting polymersome fractionation. a) 46 µm polymersomes and b) 58 µm polymersomes fractionated in a DLD device. Dashed lines represent computational simulations and solid lines represent actual experiments.

5.5 Conclusion

We developed a hydrodynamic, forced-based computational model to understand the fractionation of polymersomes in a DLD microfluidic device. We found that the key parameter in determining the separation between two particles is primarily determined by the strength of the attraction between the cylindrical post and spherical polymersome. Interestingly, we found that the repulsive force experienced by the polymersome depends exponentially on H. Using this model, we can correctly predict the fractionation of two polymersomes of different sizes (46 and 58 µm) in a DLD device.

5.6 Acknowledgements

5.7 Appendix

5.7.1 Fluid Velocity within the Microfluidic Device

The Reynolds number for the steady motion of a sphere with velocity V and diameter D_p moving through a fluid with density ρ and viscosity μ is

$$\mathrm{Re_D} = \frac{\rho V D_p}{\mu} \qquad\qquad \textbf{Equation 5.9}$$

For our present system, $\mathrm{Re_D} \ll 1$ and we can reduce the full Navier-Stokes equation to the Stokes equation,

$$\nabla P = \mu \nabla^2 v \qquad\qquad \textbf{Equation 5.10}$$

and determine the velocity throughout the microfluidic device. Consider first the simple case of fluid flow past one cylinder. We can analytically determine the fluid velocity past this cylinder by invoking streamline solutions of known problems and the principle of superposition. The fluid velocity past a cylinder is a superposition of a uniform fluid velocity and a doublet flow as shown in Figure 5-9.
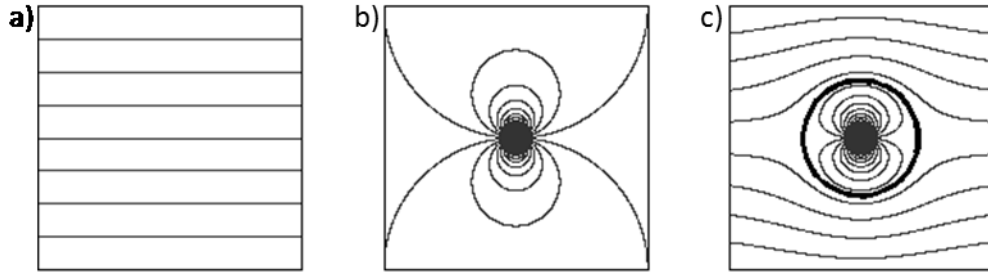
Figure 5-9: Streamlines solutions for velocity fields. a) Uniform 1D flow. b) Doublet flow. c) Superposition of (a) and (b) resulting in the solution for the non-lifting flow past a cylinder.

The streamlines for the velocity fields presented in Figure 5-9 are given by

$$\psi_{uniform} = Uy$$

<div align="right">Equation 5.11</div>

$$\psi_{doublet} = -\frac{\kappa}{2\pi}\frac{\sin\theta}{r}$$

<div align="right">Equation 5.12</div>

Transforming Equation 5.11 into polar coordinates (or conversely Equation 5.12 into rectangular coordinates) and invoking superposition, the streamlines for Figure 5-9c are given by

$$\Psi = Ur\sin\theta\left(1-\frac{R^2}{r^2}\right)$$

<div align="right">Equation 5.13</div>

$$\Psi = Uy\left(1-\frac{R^2}{x^2+y^2}\right)$$

where the substitution $\kappa/2\pi U = R^2$ has been made. The velocity components can be calculated from the streamlines by taking the appropriate partial derivatives

100

$$v_x = \frac{\partial \Psi}{\partial y} = U - UR^2 \frac{x^2 - y^2}{(x^2 + y^2)^2}$$

Equation 5.14

$$v_y = -\frac{\partial \Psi}{\partial x} = -2UR^2 \frac{xy}{(x^2 + y^2)^2}$$

Equation 5.15

Translating this solution to the problem of n cylindrical posts in our microfluidic device, we can once again invoke superposition and sum over the n posts

$$v_x = U - UR^2 \sum_{i=1}^{n} \frac{(x - x_i)^2 - (y - y_i)^2}{[(x - x_i)^2 + (y - y_i)^2]^2}$$

Equation 5.16

$$v_y = -2UR^2 \sum_{i=1}^{n} \frac{(x - x_i)(y - y_i)}{[(x - x_i)^2 + (y - y_i)^2]^2}$$

Equation 5.17

where (x_i, y_i) refer to the coordinates of the cylindrical posts. We can see from Equation 5.16 and Equation 5.17 that the x- and y-velocity components depend on all of the posts. The $1/r^4$ dependence, however, implies that far away posts have less of a contribution to the velocity at a given point than posts that are closer.

5.7.2 Torque on the Polymersome

Consider once again the solution to the problem of fluid flow past one cylinder. The rectangular velocities presented in Equation 5.14 and Equation 5.15 can be converted to cylindrical velocities and are given by:

$$v_r = U \cos \theta \left(1 - \frac{R^2}{r^2} \right)$$

Equation 5.18

$$v_\theta = -U \sin \theta \left(1 + \frac{R^2}{r^2} \right)$$

Equation 5.19

In order to calculate the torque on the polymersome due to the fluid, we must first determine the fluid viscous stress, which can be determined by taking the appropriate partial derivative of the fluid velocity:

$$\tau_{r\theta} = \mu \left[r \frac{\partial}{\partial r} \left(\frac{V_\theta}{r} \right) + \frac{1}{r} \frac{\partial V_r}{\partial \theta} \right] = \frac{4\mu U R^2 \sin \theta}{r^3}$$

Equation 5.20

The torque on the polymersome can be calculated by integrating the viscous stress over the surface of the particle. Every point on the surface of the polymersome can be parameterized with a position vector $\vec{r}$ as show in Figure 5-10.

$$\vec{r} = (a \sin \phi \cos \theta + p)\hat{\imath} + (a \sin \phi \sin \theta + q)\hat{\jmath} + a \cos \phi \, \hat{k}$$
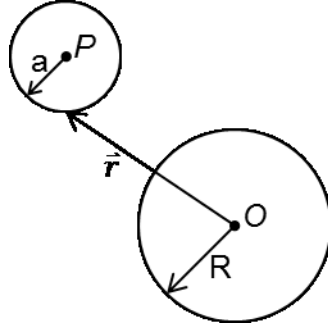
Equation 5.21

Figure 5-10: Post and polymersome geometry. Top view of cylindrical post located at the origin O with coordinates (0,0,0) and spherical polymersome located at P with coordinates (p,q,0).

For the purposes of the torque calculation, we will assume that the top and bottom edges of the post do not affect the polymersome and as such the z-direction in the parameterization is neglected. The viscous stress can be restated in terms of the parameterization as follows:

$$\tau_{r\theta} = 4\mu U R^2 \frac{\left|\vec{r}_{xy} \cdot \hat{j}\right|}{\left|\vec{r}_{xy}\right|} \cdot \frac{1}{\left|\vec{r}_{xy}\right|^3}$$

Equation 5.22

The expression for the differential torque on the polymersome is given by:

$$dG = \tau_{r\theta} \cdot a \sin\phi \, dS$$

Equation 5.23

and the differential surface element on the polymersomes is:

$$dS = a^2 \sin\phi \, d\phi d\theta$$

Equation 5.24

103

The final expression for the torque on the polymersome can be determined by combining Equation 5.22 – Equation 5.24:

G

$$= 4\mu U R^2 a^3 \int_0^{2\pi} \int_0^{\pi} \frac{a \sin\phi \sin\theta + q}{[(a \sin\phi \cos\theta + p)^2 + (a \sin\phi \sin\theta + q)^2]^2} \sin^2\phi \, d\phi d\theta$$

Equation 5.25

This integral was evaluated numerically using MATLAB.

5.7.3 The Grand Mobility Matrix

The resistance matrix (Equation 5.6) can be re-written to show all of the individual components as follows:

$$\begin{bmatrix} F_x \\ F_y \\ F_z \\ T_x \\ T_y \\ T_z \end{bmatrix} = -\mu \begin{bmatrix} K & D \\ C & \Omega \end{bmatrix} \begin{bmatrix} V_x \\ V_y \\ V_z \\ \omega_x \\ \omega_y \\ \omega_z \end{bmatrix}$$

Equation 5.26

where F_i is the external force acting on the polymersome, T_i is the external torque acting on the polymersome, V_i is the polymersome linear velocity, and ω_i is the polymersome angular velocity in the x, y, and z directions. The four components of the resistance matrix consist of the translational dyadic (K), the rotational dyadic (Ω), and the coupling dyadic (C), and the transpose of the coupling dyadic (D). The resistance matrix for a sphere-cylinder system can be approximated by considering a sphere-sphere system. Detailed analysis of this system is presented by Brenner [15]. Let spheres 1 and 2 have

radii a_1 and a_2, respectively. Let the instantaneous center-to-center distance be $2h$ and let $\hat{e}_{21} = -\hat{e}_{12}$ be a unit vector drawn from the center of sphere 2 to sphere 1. The sphere-sphere system can be described by the following system of equations:

$$\vec{F}_1 = -\mu(\mathbf{K}_{11} \cdot \vec{U}_1 + \mathbf{K}_{12} \cdot \vec{U}_2 + \mathbf{D}_{11} \cdot \vec{\omega}_1 + \mathbf{D}_{12} \cdot \vec{\omega}_2)$$

$$\vec{F}_2 = -\mu(\mathbf{K}_{21} \cdot \vec{U}_1 + \mathbf{K}_{22} \cdot \vec{U}_2 + \mathbf{D}_{21} \cdot \vec{\omega}_1 + \mathbf{D}_{22} \cdot \vec{\omega}_2)$$

Equation 5.27

$$\vec{T}_1 = -\mu(\mathbf{C}_{11} \cdot \vec{U}_1 + \mathbf{C}_{12} \cdot \vec{U}_2 + \mathbf{\Omega}_{11} \cdot \vec{\omega}_1 + \mathbf{\Omega}_{12} \cdot \vec{\omega}_2)$$

$$\vec{T}_2 = -\mu(\mathbf{C}_{21} \cdot \vec{U}_1 + \mathbf{C}_{22} \cdot \vec{U}_2 + \mathbf{\Omega}_{21} \cdot \vec{\omega}_1 + \mathbf{\Omega}_{22} \cdot \vec{\omega}_2)$$

In our simulation, sphere 2 will be held motionless and $\vec{U}_2 = \vec{\omega}_2 = 0$. For sphere 1, Equation 5.27 reduces to:

$$\vec{F}_1 = -\mu(\mathbf{K}_{11} \cdot \vec{U}_1 + \mathbf{D}_{11} \cdot \vec{\omega}_1)$$

Equation 5.28

$$\vec{T}_1 = -\mu(\mathbf{C}_{11} \cdot \vec{U}_1 + \mathbf{\Omega}_{11} \cdot \vec{\omega}_1)$$

Due to the interaction between the spheres, the four dyadic take the form of

$$\mathbf{K}_{11} = 6\pi a_1 \left[\mathbf{I} + \frac{9}{64} \left(\frac{a_1}{h}\right) \left(\frac{a_2}{h}\right) (\mathbf{I} + 3\hat{e}_{12}\hat{e}_{12}) \right]$$

$$\mathbf{\Omega}_{11} = 8\pi a_1^3 \left[\mathbf{I} + \frac{3}{64} \left(\frac{a_1}{h}\right)^3 \left(\frac{a_2}{h}\right) (\mathbf{I} - \hat{e}_{12}\hat{e}_{12}) \right]$$

Equation 5.29

$$\mathbf{C}_{11} = \frac{9}{16} \pi a_1 a_2 \left(\frac{a_1}{h}\right)^3 [\hat{e}_{12} \times \mathbf{I}]$$

$$\mathbf{D}_{11} = -\frac{9}{16} \pi a_1 a_2 \left(\frac{a_1}{h}\right)^3 [\mathbf{I} \times \hat{e}_{12}]$$

where I is the identity dyadic. If we define the center of the polymersome at (p,q) and the center of the post at (0,0), we can express the entire cross and dyadic products with the unit vector $\hat{e}_{12}$ in Equation 5.29 as follows:

$$\hat{e}_{12} = -\frac{p}{2h}\hat{\imath} - \frac{q}{2h}\hat{\jmath}$$

$$\hat{e}_{12}\hat{e}_{12} = \frac{1}{4h^2}\begin{bmatrix} p^2 & pq & 0 \\ pq & q^2 & 0 \\ 0 & 0 & 0 \end{bmatrix}$$

$$\hat{e}_{12} \times I = I \times \hat{e}_{12} = \frac{1}{2h}\begin{bmatrix} 0 & 0 & -q \\ 0 & 0 & p \\ q & -p & 0 \end{bmatrix}$$

Equation 5.30

Finally, substituting Equation 5.30 into Equation 5.29 we obtain the final expression for the components of the resistance matrix:

$$K_{11} = 6\pi a_1 \begin{bmatrix} 1 & 0 & 0 \\ 0 & 1 & 0 \\ 0 & 0 & 1 \end{bmatrix} + \frac{9}{64}\left(\frac{a_1}{h}\right)\left(\frac{a_2}{h}\right)\begin{bmatrix} 1+3p^2 & 3pq & 0 \\ 3pq & 1+3q^2 & 0 \\ 0 & 0 & 1 \end{bmatrix}$$

$$\Omega_{11} = 8\pi a_1^3 \begin{bmatrix} 1 & 0 & 0 \\ 0 & 1 & 0 \\ 0 & 0 & 1 \end{bmatrix} + \frac{3}{64}\left(\frac{a_1}{h}\right)^3\left(\frac{a_2}{h}\right)\begin{bmatrix} 1-p^2 & -pq & 0 \\ -pq & 1-q^2 & 0 \\ 0 & 0 & 1 \end{bmatrix}$$

Equation 5.31

$$C_{11} = \frac{9}{16}\pi a_1 a_2 \left(\frac{a_1}{h}\right)^3 \frac{1}{2h}\begin{bmatrix} 0 & 0 & -q \\ 0 & 0 & p \\ q & -p & 0 \end{bmatrix}$$

$$D_{11} = \frac{9}{16}\pi a_1 a_2 \left(\frac{a_1}{h}\right)^3 \frac{1}{2h}\begin{bmatrix} 0 & 0 & q \\ 0 & 0 & -p \\ -q & p & 0 \end{bmatrix}$$

The grand mobility matrix can now be determined by inverting the resistance matrix:

$$\bar{\bar{\mathcal{M}}} = \begin{bmatrix} K_{11} & D_{11} \\ C_{11} & \Omega_{11} \end{bmatrix}^{-1}$$

Equation 5.32

5.8 References

1. Heftmann, E., *Chromatography: Fundamentals and Applications of Chromatographic and Electrophoretic Methods.* 4 ed. 1983, New York: Elsevier Science.

2. Huang, L.R., et al., *Continuous particle separation through deterministic lateral displacement.* Science (New York, N.Y.), 2004. **304**: p. 987-90.

3. Morton, K.J., et al., *Hydrodynamic metamaterials: Microfabricated arrays to steer, refract, and focus streams of biomaterials.* Proceedings of the National Academy of Sciences of the United States of America, 2008. **105**(21): p. 7434-7438.

4. Cerbelli, S., M. Giona, and F. Garofalo, *Quantifying dispersion of finite-sized particles in deterministic lateral displacement microflow separators through Brenner's macrotransport paradigm.* Microfluidics and Nanofluidics, 2013. **15**(4): p. 431-449.

5. Inglis, D.W., et al., *Critical particle size for fractionation by deterministic lateral displacement.* Lab on a Chip, 2006. **6**(5): p. 655-658.

6. Long, B.R., et al., *Multidirectional sorting modes in deterministic lateral displacement devices.* Physical Review E, 2008. **78**(4): p. 9.

7. Frechette, J. and G. Drazer, *Directional locking and deterministic separation in periodic arrays.* Journal of Fluid Mechanics, 2009. **627**: p. 379-401.

8. Hayward, R.C., et al., *Dewetting instability during the formation of polymersomes from block-copolymer-stabilized double emulsions.* Langmuir, 2006. **22**(10): p. 4457-4461.

9. Lorenceau, E., et al., *Generation of polymerosomes from double-emulsions.* Langmuir, 2005. **21**(20): p. 9183-9186.

10. Shum, H.C., et al., *Double emulsion templated monodisperse phospholipid vesicles.* Langmuir, 2008. **24**(15): p. 7651-7653.

11. Utada, A.S., et al., *Monodisperse double emulsions generated from a microcapillary device.* Science, 2005. **308**(5721): p. 537-541.

12. Parsegian, V.A., *Van der Waals forces: a handbook for biologists, chemists, engineers, and physicists*. 1939.

13. Napper, D.H., *Steric Stabilization.* Journal of Colloid and Interface Science, 1977. **58**(2): p. 390-407.

14. Bell, G.I., M. Dembo, and P. Bongrand, *Cell Adhesion - Competition Between Nonspecific Repulsion and Specific Bonding.* Biophysical Journal, 1984. **45**(6): p. 1051-1064.

15. Brenner, H., *The Stokes resistance of an arbitrary particle - II, An Extension.* Chemical Engineering Science, 1964. **19**(9): p. 599-629.

6 Summary of Major Results and Suggested Future Research

6.1 Major Results with Respect to the Specific Aims

Aim 1:   Develop controlled release nano-polymersome platform for the encapsulation and release of chemotherapeutic drug and determine toxicity in cancer cells.

Results: A nano-polymersome system using a biodegradable and biocompatible block copolymer, PEO-PCL, was developed to encapsulate the chemotherapeutic drug gemcitabine, and released this cargo based on an external pH stimulus (acidic environment). We determined the efficacy of the PolyGems compared to the unencapsulated drug, FreeGem, and found that the PolyGems performed at par with the free drug with a total cell killing of 1 log at 1 µM gemcitabine dose.

Aim 2:   Quantify the release of an encapsulated fluorescent dye from giant polymersomes due to photo-initiated rupture.

Result: The rupture of giant polymersomes made from OB14.5 and OB29 polymers was quantified by detecting the released fraction of a fluorescent dye, sulforhodamine B, from the aqueous core of the vesicles. Polymersomes were irradiated using a 690 nm diode laser with a fluence rate of 200 mW/cm^2 and a maximal light dose of 100 J/cm^2. OB14.5 polymersomes released more sulforhodamine B than OB29 polymersomes because OB14.5 polymersomes have a softer membrane.

Aim 3:   Encapsulate a photosensitizer in nano-polymersomes for photodynamic therapy and assess the *in vitro* and *in vivo* toxicity of the polymersomes.

Result: A second generation photosensitizer, benzoporphyrin derivative monoacid A (BPD-MA), was encapsulated in the hydrophobic membrane of OB14.5 nano-polymersomes at a high molar loading ratio (40%). We compared the *in vitro* and *in vivo* toxicity of OB14.5-40% BPD to a liposomal formulation of BPD-MA, verteporfin. OB14.5-40% BPD polymersomes outperformed verteporfin both in *in vitro* toxicity assays and *in vivo* tumor response. The polymersomes serve to protect BPD-MA from being leached by serum proteins, and as such the concentration of BPD-MA that is unbound and able to generate singlet oxygen is greater than when verteporfin is used as the carrier vehicle.

Aim 4:   Develop a force-based model for understanding and predicting polymersome

fractionation in a deterministic lateral displacement microfluidic device.

Results: A hydrodynamic model was developed that incorporated shear, hydrodynamic

torque, van der Waals attraction, steric repulsion as the forces and torques felt

by the polymersome as it navigates a deterministic lateral displacement device.

We found that the most sensitive parameter in fractionating the polymersomes

is the Hamaker constant, which dictated the length of the "contact time"

between the polymersome and the cylindrical post. We conducted experiments

that fractionated polymersomes of two different sizes, and recapitulated this

experimental result via a numerical simulation using the model that was

developed.

6.2 Further Investigations Towards the Development of Dual Drug Delivery Polymersomes for Combined Chemotherapy and Photodynamic Therapy

The systemic toxicities associated with chemotherapy suggest that there is a strong need to provide local delivery of drugs to tumors. The work presented in Chapters 2 and 4 of this dissertation outline two strategies for encapsulating chemotherapeutics and photosensitizers for PDT, respectively. Combining these modalities can have a synergistic effect on treatment outcomes.

Several challenges must be considered for a dual-delivery system to be successful. An important question to answer consider is which therapy to do first – chemotherapy with polymersomes requires diffusion of the drug out of the aqueous lumen and into the tumor and PDT requires photosensitizer accumulation followed by

irradiation of the diseased tissue. One can allow for the drug to escape the polymersomes and cause cell damage, and then irradiate with light to generate singlet oxygen. However, the time scale for release of the chemotherapeutic drug might not match the time scale for accumulation of the photosensitizer, i.e. the drug is being released into the tumor while the photosensitizer is being cleared from the tumor.

An alternate strategy would be to do PDT first with a short drug-light interval and cause vascular damage surrounding the tumor [1]. The tumor will lose its nutrient supply and undergo cell death. While this vascular shutdown is taking place, the chemotherapeutic can diffuse out of the polymersomes and cause direct cell death.

The polymersome drug delivery system can be improved by adding targeting ligands onto the surface of the polymersome. The overexpression of EGFR on OVCAR-5 cells can be exploited to preferentially accumulate polymersomes at the tumor site as opposed to other tissues. Work has been previously done conjugating cetuximab to BPD-MA, but this photoimmunoconjugate was not effective at killing OVCAR-5 cells [2]. It is possible that cetuximab hindered the ability of BPD-MA to effectively generate singlet oxygen. A polymersome system could be an improvement over the direct conjugation of an antibody to BPD-MA. The surface of polymersomes can be conjugated via peptide coupling reactions to include EGF binding domains (RGD domain). A newer approach would be to blend short surfactant-like peptides containing the binding domain with the polymer. Our lab developed has a family of oleosin mutants that resemble block copolymers [3]. Using molecular biology, one could include the RGD binding domain on the terminal end of the peptide and blend this targeting peptide with the polymer.

6.3   References

1.   Castano, A.P., P. Mroz, and M.R. Hamblin, *Photodynamic therapy and anti-tumour immunity.* Nature reviews. Cancer, 2006. **6**: p. 535-45.

2.   Abu-Yousif, A.O., et al., *Epidermal growth factor receptor-targeted photosensitizer selectively inhibits EGFR signaling and induces targeted phototoxicity in ovarian cancer cells.* Cancer letters, 2012. **321**: p. 120-7.

3.   Vargo, K.B., R. Parthasarathy, and D.A. Hammer, *Self-assembly of tunable protein suprastructures from recombinant oleosin.* Proceedings of the National Academy of Sciences of the United States of America, 2012. **109**(29): p. 11657-11662.